Non-Conventional Plasma Machining and Nano-polishing of Optics

A thesis submitted
in partial fulfillment of the requirements
for the degree of

Doctor of Philosophy

By

ENNI KRISHNA
Roll No. 186103016

Department of Mechanical Engineering
Indian Institute of Technology Guwahati
Guwahati, India

November, 2023

Department of Mechanical Engineering
Indian Institute of Technology Guwahati
Guwahati-781039
INDIA

CERTIFICATE

It is certified that the work contained in the thesis entitled "***Non-Conventional Plasma Machining and Nano-polishing of Optics***," submitted by **Enni Krishna**, Roll No. 186103016 to the Indian Institute of Technology Guwahati for the degree of Doctor of Philosophy, has been carried out under my supervision in the Department of Mechanical Engineering, Indian Institute of Technology Guwahati. This work has not been submitted elsewhere for any other degree or diploma award.

The thesis has reached the standard fulfilling the requirements for the degree of Doctor of Philosophy award by the institute's regulations.

Manas Das

Dr. Manas Das

Date: 23/11/23

Department of Mechanical Engineering

Indian Institute of Technology Guwahati

Guwahati-781039, Assam, India

Declaration

I declare that this written submission represents my ideas in my own words, and where others' ideas or words have been included, I have adequately cited and referenced the sources. I also declare that I have adhered to all academic honesty and integrity principles and have not misrepresented, fabricated, or falsified any idea/data/fact/source in my submission. I understand that any violation of the above will cause disciplinary action by the Institute and can also evoke penal action from the sources which have thus not been adequately cited or from whom proper permission has not been taken when needed.

Date: 23/11/23

Enni Krishna
Roll No. 186103016

Dedicated to

My Father
Late E Ramalingam

ACKNOWLEDGMENT

I want to express my deepest gratitude and respect to my Supervisor, Dr. Manas Das, Department of Mechanical Engineering of Indian Institute of Technology Guwahati, for his valuable support and active supervision throughout this period. With his guidance and persistent help, this dissertation is possible.

I also want to thank members of my dissertation committee, Prof. S Kangara, Prof. S. Senthilvelan, and Prof. Tamal Banerjee, for their constant support, guidance, and constructive criticism and direction during the dissertation.

I want to express my extreme and sincere gratitude to Dr. Sam Dayala Dev, Director of the ISRO Inertial Systems Unit, who has been a constant source of inspiration and encouragement for this academic research.

I extend my deep sense of reverence to my senior colleagues Shri R Raman, Smt. Santha Kumari and Smt. Usha K (Group Director, ISG/AIS) for their encouragement and belief in me for pursuing my higher studies Ph.D.

I place on record my sincere thankfulness to my friends and colleagues at ISRO Inertial Systems Unit, Shri P B Narayana Kutty, Shri Jagroop, Smt. Sreelakshmy K, Shri Arun George, and Shri Sukumaran K D for their constant support during experimentations and characterizations.

Above all, I thank my wife, Smt Meghana, for her constant support and patience. My family members, mother, sister, and brother, have given me unconditional support for completing this thesis, and for that, I am expressing my gratitude.

I greatly and emotionally thank my beloved father (Late Enni Ramalingam) for his recurring inspiration throughout my carrier. He provided the foundation for my studies and the backbone of my carrier, which helped to gain an attitude toward higher studies.

Above everything, I thank my GOD for blessing me with wisdom and good health throughout this endeavor.

Enni Krishna

ABSTRACT

Glass has become essential in everyday life. Our modern society uses glass as a key material in thousands of products, ranging from simple glass bottles to sophisticated information technology (IT) systems. The pace of innovation in glass is accelerating due to progress in understanding glass physics and chemistry, combined with modern analytic and control technologies. Due to its unique properties, fused silica finds many applications among glass materials as a passive and active optical system. It is widely used as high-power lenses and windows for astronomy, microlithography, laser material processing, and high-power laser applications. But fused silica optics plays an active role in the inertial sensors category for aerospace applications. The ultrasmooth total internal reflecting corner optics for refractive-based ring laser gyroscope and freeform hemispherical resonator shell for vibratory gyroscope are significant and critical applications of the fused silica substrate. These applications demand damage-free fused silica optics. But the brittle nature of the fused silica material poses a challenge for manufacturing.

Conventional contact type of machining induces damage at the fused silica surface and significant damage incurred at the subsurface. Hence, a quantum of research is carried out to eliminate subsurface damage of fused silica optics by various non-conventional methods. Among the non-conventional methods, atmospheric plasma processing emerged as a deterministic process for polishing fused silica optics. The atmospheric plasma processing method requires a high-precision mechanism for processing a free-form optical application; moreover, achieving uniform machining is challenging. Similarly, low-pressure plasma processing can process the entire optics simultaneously without precision mechanization. The physical action of the ions at low pressure damages the surface topography of the optical surface. Medium-pressure plasma processing carries the energy advantage of the low-pressure plasma system and chemical reactivity as atmospheric plasma processing.

The existing confined medium-pressure plasma system suffers numerous disadvantages like low material removal rate (0.008 mm3/min), formation of redeposition layers, achieving sustained material removal rate for long operating cycles, etc. The present study designed and developed a plasma flow system to overcome these limitations. The plasma flow system consists of fine mass flow controllers for precise control of Helium (processing gas), sulfur hexafluoride (reactive gas), and oxygen (catalytic gas). The flow

system also consists of a gas dosing valve for controlling the total pressure of the plasma chamber. The pumping system can remove the chamber pressure rise during machining. Hence, there are new reactive radicals available for the entire machining cycle. The comparative study between the confined and plasma flow systems reveals that the plasma flow system results in a 300% increase in Material Removal Rate (MRR), absence of redeposition layer, and sustained MRR for the entire one-hour cycle operation. Moreover, even at a higher MRR, the plasma flow system effectively improves the surface finish and removes the surface and subsurface defects.

The material removal rate and total material removal determine the end product's performance. This is essential to predict the MRR during plasma polishing, or it will hinder the yield of the process. This study developed a non-invasive in-situ MRR methodology using optical emission spectroscopy to predict the MRR during plasma polishing. The method utilizes the relative intensity ratio of silicone oxidation states (Si II at 518 nm and Si III at 481 nm) for predicting the MRR. Hence, this method is very accurate and validated experimentally.

The uniform plasma processing for dielectric barrier capacitive coupled discharge system depends primarily on the chamber configuration. Consistent plasma processing is essential for freeform optics like hemispherical resonator shells. Unsymmetric material removal can detrimentally affect the device quality factor. Hence, establishing the uniform radial distribution inside the plasma chamber is essential. The uniform radical distribution depends on the free volume of the system. Comsol® simulation study carried out for optimization of the chamber configuration. The V-shaped groove provides a uniform radical distribution with optimum electron density. The analytical simulation was validated experimentally using an emission spectrometer.

Machining induces stress and subsurface damage to the fused silica substrate. The presence of subsurface damage dramatically influences the performance and life of the optical device. The unique properties, like being 100% transparent to ultra-violet and visible light, low damping for the vibratory resonator, high laser damage threshold, etc., cannot be maintained due to machine-induced damage. Partial removal of damaged layers also significantly affects performance. Hence, it is essential to quantify the depth of the damaged layers after machining. Various methods are being developed, such as X-ray micro-diffraction, electron-induced Kossel diffraction with a scanning electron microscope

(SEM), and convergent beam electron diffraction with a transmission electron microscope (TEM) for analyzing the stress by knowing the elastic strain in a crystalline material. These diffraction methods provide direct information about the lattice parameters of crystalline materials. Hence, these methods need crystal periodicity, like metals. But no reliable way exists for quantifying the depth of damage of fused silica optics. Therefore, this study utilizes the confocal capability of Raman microscopy to quantify the damage depth of the machined and ground optics in a non-destructive way. A frequency shift of ideal six-membered transitions at the surface to bulk provides information about the machine-induced damage depth. Grinding induces plastic deformation or densification on the optics. The densification causes short-range local crystallinity in the optics. Hence, the Full Width at Half Maximum of the transition at the surface to bulk indicates the extension of plastic deformation in the optics. The ultra-sonic machining parameters were optimized by analyzing the damaged depth using confocal Raman microscopy. The quality factor (Q) of the hemispherical resonator shell, which is the function of damaged layers for a given design and material, is measured using Laser Doppler Vibrometer (LDV). The Q of the shell at various stages was measured, and simultaneously, damage depth was analyzed using Raman microscopy. The Q factor was highest where stress analyzed by the Raman microscopy study was less. It shows that the developed non-destructive Raman microscopy methodology for quantification of damage depth was validated.

The life and performance of the Ring Laser Gyroscope (RLG) device depend on the quality of the Total Internal Reflecting (TIR) optics. TIR optics are fabricated to super smooth surfaces by the standard chemo-mechanical polishing method. Due to the contact nature of the fabrication, it induces specific hydrated layers and chemical and physical defects at the surface of the optics. The index-matched hydrated layer is called the Beilby layer. The presence of these layers produces absorbing precursors under continuous radiation. These absorbing precursors are termed color centers and reduce the transmission of the optics and ultimately hamper the RLG device performance. Identifying and quantifying the depth of damage to the ultrasmooth surfaces is challenging. The Secondary Ion Mass Spectrometer (SIMS) was adopted to quantify the depth of the Beilby layer based on the presence of metallic impurities. The SIMS revealed the presence of non-homogenous layers, which extend about 250 nm.

The methodology was developed using a medium-pressure plasma flow system to remove the damaged layers without affecting the surface topography of the supersmooth

optics. After each experimental trial, an optical screening jig was adopted to screen the plasma-processed TIR optics. Composition of 5% SF6, 2.5% O2, and 92.5% He at 20 W power results in optimum performance, but Scanning Electron Microscopy (SEM) revealed the presence of cerium contamination at the surface after plasma processing. The chemical leaching processes are optimized to remove these contaminations from the surface. However, the fluorescence spectroscopy method reveals the presence of an Oxygen Deficiency Center (ODC) still at a depth of 350 nm of damaged layers. Hence, the plan was established to remove the 350 nm depth of damaged layers. In this study, a complete process was developed to mitigate the damaged layers of super smooth optics. Moreover, the post-processed optics shows an improvement in surface finish and one order reduction in the amplitude of power spectrum density.

The newly developed plasma flow system with higher MRR can etch the optics after matching and grinding operations. The experimental study was carried out at the coupon level to evaluate the plasma process concerning the wet etching process. The buffered hydrofluoric acid composition is optimized to achieve a similar MRR as a plasma flow system. At least three test coupons for different initial surface roughness were subjected to wet chemical etching and plasma processing. The results suggested that the wet chemical process significantly damages the surface roughness, decreasing surface energy after processing. On the other hand, there is an improvement in surface energy, and surface roughness deteriorates marginally. Hence, plasma processing replacing the hazardous chemical process can reduce the optics' labor-intensive polishing time and cost.

This study explored the new methodology for polishing the optics under a medium-pressure plasma flow system to improve the surface integrity of supersmooth optics. It developed a non-destructive and reliable method for quantifying the damaged layers of machined and ground optics using confocal Raman microscopy. It helped in the optimization of fused silica glass machining parameters. It identified and quantified the depth of the index-matched hydrated layer using Secondary Ion Mass Spectroscopy. The concentration of the oxygen deficiency center was quantified with the help of fluorescence spectroscopy. The plasma flow system can be a worthy replacement for the hazardous wet chemical etching process.

TABLE OF CONTENTS

List of Figures

LIST OF TABLES

NOMENCLATURES

A	Einstein coefficient
n_e	Electron Density
g	Degeneracy factor
T_e	Electron temperature
T_i	Ion temperature
K_B	Boltzmann's constant
ev	Electron volt
h	Plank's constant
λ	Wavelength
c	Speed of light
I	Intensity of light
Sa	Average surface roughness entire area
Ra	Center-line Average surface roughness
E_1'	Color center
PL	Photo luminescence

ACRONYM

AFM	Abrasive flow machining
MAF	Magnetic abrasive finishing
MRAFF	Magnetorheological abrasive flow finishing
MFP	Magnetic float polishing
MRF	Magnetorheological finishing
MRR	Material removal rate
SSD	Sub-surface damage
RAP	Reactive atom plasma machining
APPP	Atmospheric pressure plasma polishing
APPJ	Atmospheric pressure plasma jet
MWP	Microwave plasma
OES	Optical emission spectrometer
NIST	National institute of standards and technology
LIDT	Laser-induced damage threshold
CRM	Collision radiative mode

MPPP	Medium Pressure Plasma Processing
HCl	Hydrochloric acid
H_2O_2	Hydrogen peroxide
HNO_3	Nitric acid
He	Helium
O2	Oxygen
SF6	Sulfur hexafluoride
CMP	Chemo-mechanical polishing
Ce	Cerium
Fe	Iron
K	Potassium
Al	Aluminum
Si	Silicone
SiO_2	Silica
ODC	Oxygen deficiency centers
NBOH	Non-bridging oxygen hole center
SCCM	Standard cubic centimeter per minute
SEM	Scanning electron microscopy
EDX	Energy dispersive X-ray spectroscopy
SIMS	Secondary ion mass spectroscopy
XPS	X-ray photoelectron spectroscopy
PSD	Power spectral density
HER	High etching rate
LER	Low etching rate
RF	Radiofrequency
MFC	Mass flow controller
BOE	Buffer oxide etching
HF	Hydrofluoric acid
DI	De-ionized
LDV	Laser Doppler Vibrometry
TRP	Total Internal Reflecting prism

Chapter 1
Introduction

The history of glass-making starts way back more than 5000 years, and glass materials have become an essential part of human civilization. Due to the growing population and quality of life, the glass industry faces challenges related to sustainable production and meeting the demanded performance (Mauro and Zanotto, 2014). Glass has become essential in everyday life. Our modern society uses glass as a key material in thousands of products, ranging from simple glass bottles to sophisticated information technology (IT) systems. The pace of innovation in glass is accelerating due to progress in understanding glass

physics and chemistry, combined with modern analytic and control technologies (Morse and Evenson, 2016). Key and well-established glass-related markets include consumer glass and electronics, containers, insulation, composites, windows, automotive glass, lighting, communications, optics, etc.

1.1 Classification of glass

- **Fused Silica** is the purest form of Silicon Dioxide (SiO_2). This glass has superior UV and IR spectra transmission, a very low dielectric coefficient, and excellent properties where fluorescence or solarization is an issue. Unlike sapphire (a crystalline structure, not amorphous), fused silica can be shaped into different forms and produce extremely high-grade (pure) fused silica glasses that exhibit excellent ultraviolet and infrared performance. Where purity, a non-reactive, durable substrate, and homogeneity between melts (uniform optical properties) are needed, this high-quality material is the likely choice.
- **Bk 7** is a barium borosilicate glass known for its high transmission and clear appearance. It is the most common material for many optical glass applications because it offers good optical properties and a reasonable price. It is often used as a standard of comparison for other glass materials.
- **Borofloat** is a special Schott borosilicate glass. It is characterized by excellent flatness and better heat resistance. These characteristics make boro-float more costly than float glass. However, borosilicates retain shape and handle thermal shock better than other less expensive glasses.
- **B270 or Crown Glass** has a sound optical transmission and appears crystal clear due to fewer impurities. It can be polished and readily accepts all types of coating**.**
- **GE 124 & NSG OZ** are fused Quartz glasses. Fused quartz is used in applications where sound ultraviolet light transmission, excellent thermal stability, and chemical inertness (resistance to stains) are required. Fused quartz is more challenging to polish than borosilicate. Hence the cost is high. Hence. For applications where prolonged or periodic temperatures are more extremely prevailing or there is a need for higher purity, fused quartz is an appropriate choice.
- **Soda lime**, or '**Float Glass,'** is a common, inexpensive substrate. Float glass is a sheet of glass made by floating molten glass on a bed of molten tin. This method gives the sheet uniform thickness and very flat surfaces. The oldest glass float can

appear with a slight greenish or blue tint, depending upon the amount of iron and other elements. It is quickly tempered to increase strength.

- **Zerodur** is a glass ceramic made by Schott AG. It has both an amorphous (vitreous) component and a crystalline component. It is mainly used in many optical devices such as telescopes and laser gyro cavities, requiring a substrate material with a near-zero coefficient of thermal expansion ($\sim 0.02 \times 10^{-6}$ / K at 0-50^{0}C) and excellent thermal shock resistance.

1.2 Applications of fused silica

Among the various glass materials, fused quartz glass enjoys a premium class for manufacturing high-tech products. Its fundamental unique properties are given as follows:

- High chemical purity and resistance,
- High softening temperature and thermal resistance,
- Low thermal expansion with high resistance to thermal shocks,
- High transparency from the ultraviolet to the infrared spectral range,
- High radiation resistance.

Because of the above properties, fused silica finds application in various fields, as discussed below.

1.2.1 Aerospace and astronomy

It has endurance in a hostile environment, shock resistance, low weight, and, most importantly, reliability with a long lifetime. Astronomy telescopes use fused silica lenses due to their excellent chemical homogeneity, physical inclusion, and bubble free.

1.2.2 High energy and high power lasers

It has low absorption at Ultra Violet (U V) to visible, an excellent optical index of homogeneity from surface to bulk.

1.2.3 Laser material processing

It involves transporting light from the laser source to the desired working point. An optical path needs to be created. This path comprises fiber optics, lenses, prisms, mirrors, windows, and optical components. Hence, these optical components should have lower absorption,

higher temperature stability, and high damage resistance; fused silica is the material of choice for this purpose.

1.2.4 Microlithography

It is necessary to realize electronic circuits; here, excimer ArF 193 nm laser light is used for imaging. Synthetic fused silica is the only material having a very high deep ultraviolet transmissivity and low absorption so that no image defects due to lens heating occur. It can be produced with excellent optical 3D homogeneity (common refractive index variations) and little stress birefringence.

1.2.5 Spectroscopy

Fused silica is used as a window or lens due to its excellent transmission from ultraviolet-visible near-infrared (U V-Vis-NIR) (180 nm to 3500 nm).

1.3 Aerospace sensors

For aerospace space applications, the material should tolerate a hostile environment, have shock resistance, and be reliable for a long lifetime. Aerospace sensors generally use various sensors for detection and tracking applications. Most of the applications need radiation-hard fused silica glass. Another prominent application of fused silica is inertial sensor applications, where critical elements such as sensing and corner optics need fused silica material.

1.3.1 Ultra-smooth and high surface integrity of ring laser gyro

Inertial sensors like Ring Laser Gyroscopes need corner refractive optics for the Laser to sustain. Fused silica serves the purpose very efficiently as a total internal reflecting optics due to its excellent 3D homogeneity laser can travel through the optics without loss. Because of U V and visible light transference of fused silica, no reduction in Laser intensity occurs during the performance. Due to its high Laser damage threshold, fused silica is also responsible for long sustained life. A low thermal expansion coefficient also added an advantage for the performance of the gyroscope under thermal conditions.

1.3.2 3D freeform surfaces for hemispherical resonators

Freeform surfaces can be defined as surfaces with no areas of rotational variance (within or beyond the part). The freeform surface may appear to have an arbitrary shape and regular or irregular surface structures. Freeform optics or microstructures offer designers of precision sensors opportunities and challenges for manufacturing and surface finishing. Freeform optical surfaces simplify system structure with lower mass, lower cost, smaller package size, and enhanced performance. Hemispherical shells can be considered a particular case of freeform optics with an area of rotational invariants. Advanced gyroscope like Hemi spherical resonator gyro (HRG) also utilizes fused silica as a sensing structure due to its high mechanical quality factor (Q), chemical homogeneity, and absence of any physical inclusions.

1.4 Challenges in the optical machining and fabrication process

Machining of optics poses various challenges due to its brittle nature. Machining tool induces surface and subsurface damage during machining, as shown in Fig. 1.1. The figure signifies the schematic representation of machining of fused silica optics with abrasive particles. The sharp abrasives cause indentation; it leads to semi-circular radial / lateral cracks perpendicular to the optics surface. Fractures in brittle materials propagate when the stress intensity at the crack tip is greater than the fracture toughness of the material.

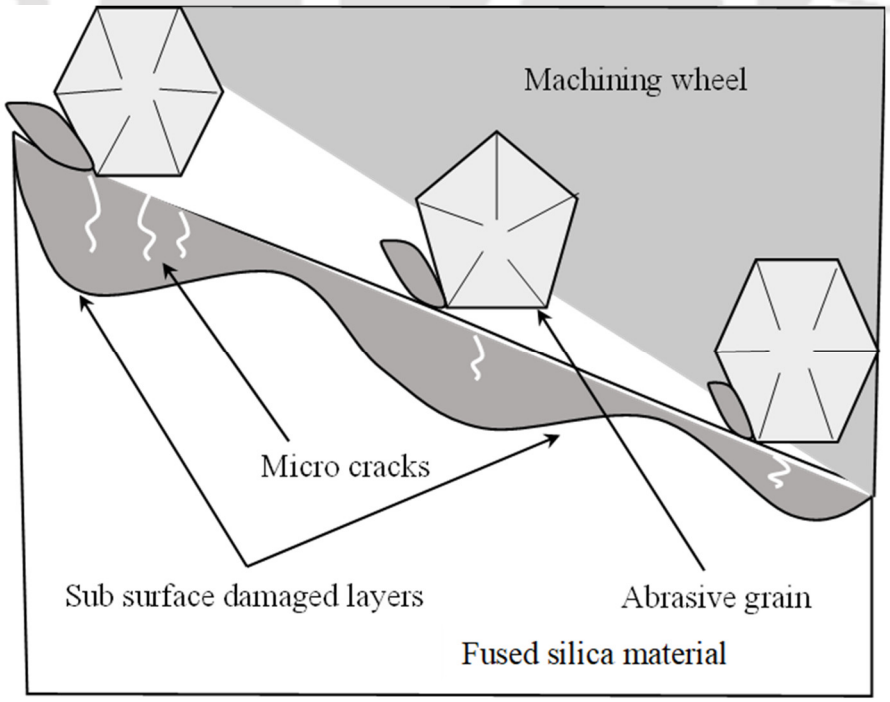

Fig. 1.1: Schematic representation of glass machining

Hence, the fused silica optics are often cut by ultra-precision grinding and finished by polishing (Li et al., 2008; Suratwala et al., 2008). As fused silica is very hard and brittle, abrasive grinding induces cracks, as shown in Fig. 1.1 (Wang et al., 2011). Hence, it takes much longer to remove the machine-induced cracks during polishing. Still, sometimes, if the damage cannot be eradicated, it will affect the optics' quality, end life, and performance.

1.4.1 Optics fabrication

A typical fabrication process starts after shaping and machining. The fabrication process produces optical components suitable for various end applications. The standard fabrication process includes numerous grinding and polishing steps to achieve desired optics. The ultimate objective of the fabrication process is to remove the material from the optics in a controlled manner. Also, the subsequent steps can clear the damage induced by one step to achieve the anticipated surface finish and surface figure.

Optical fabrication depends on the following parameters and their interactions;

- Kind of slurry and their particle distribution
- Type of lap or tool for mechanical loading
- Type of glass used

1.4.2 Effect of fabrication on optics performance

Optical fabrication influences the following properties of the optics, which affects the specific optics' performance.

Surface figure

Non-uniform load affects the surface figure, which is the long-range surface shape of the optics. It modifies the light wavefront required for optics.

Surface quality

Higher mechanical load during fabrication affects the characteristics of the optics, such as structural modification, surface, sub-surface damage, etc. It is a critical parameter that influences the laser damage threshold and scattering losses of the resultant optics.

Surface roughness

The presence of a rouge particle in the slurry can affect the optics' short-range surface topography and induce laser-beam contrast and scatter sites for high-power laser

application.

Material removal rate

The rate at which material is removed from the optics affects the processing time and cost. So, the ideal optical fabrication process optimizes the above-said parameters without compromising the time and manufacturing cost of the optics.

The many optical components' performance and life depend on surface integrity, which combines surface quality and surface metallurgy. The surface integrity depends on how optics are finished after grinding and machining, such as polishing.

1.5 Review of polishing methods used for the fabrication of optics

Advanced optical designers require shapes and materials that are challenging to finish. As designers become more intricate, new fabrication tools and techniques are needed. A general overview of some precision polishing methods and advanced surface finishing methods that enable precision fabrication of flats and spheres and increasingly complex optics, such as aspheric and freeform shapes, are highlighted. To understand and appreciate the challenges in optical polishing, the primary classification of the most commonly used optical glass with precision and advanced applications must be studied.

The following classification chart provides an idea of essential processes for the precision polishing of glass. There are three popular theories of glass polishing. Hooke, Newton, and Rayleigh proposed the ‘wear theory,’ which says that polishing occurs by the mechanical wear of the abrasives with the glass surface. In short, it is an extension of grinding. This is also called the ‘hypothesis of abrasion.’ The other theory is the ‘flow theory’ or ‘flow hypothesis,’ proposed by Beilby. It says that the polishing compounds can be used to form an amorphous layer of glass that can be smeared to fill the void of the glass surface. Finally, Preston and Grebenshchikov advanced the ‘chemical theory’ or ‘chemical hypothesis.’ The actual material removal rate in the glass depends on the chemical durability of the glass rather than the micro-hardness or softening point of the glass. As stated by Izumitani, there is no bulk material removal; only a soft, hydrated layer is removed. There is a chemical reactivity between glasses, sometimes with lap and always with polishing slurry, a mixture of water, polishing powder, and additives. However, as the wear on the polishing pads takes place, the energy put in is reduced. Hence, MRR is also

reduced. The SiO_2 film surface first reacts with cerium oxide (CeO_2) particles, forming a bonding of Si-O-Ce. Further, mechanical tearing of those bonds leads to removing SiO_2 instead of lump Silicon hydroxide ($Si(OH)_4$). Broadly glass polishing is classified into two major categories conventional complete lap polishing and sub-aperture non-conventional polishing as shown in Fig. 1.2. The full aperture polishing also known as conventional polishing. The sub-aperture polishing emerged to finish complex structures without inducing the surface defects. It has classified based on the mechanism of material removal and processing tool such as ion beam, laser, plsma ions and radicals etc.

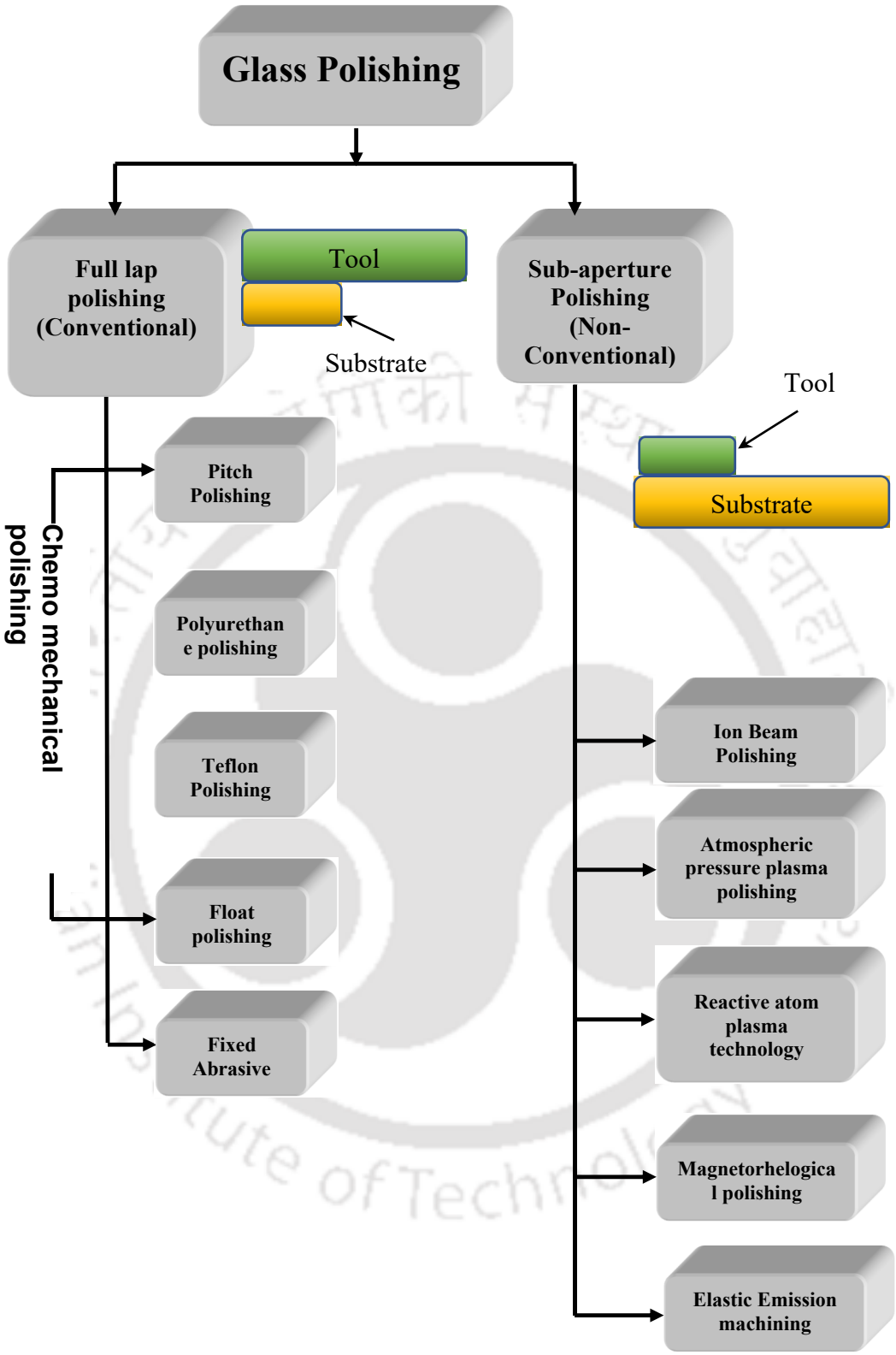

Fig. 1.2: Classifications of glass polishing methods

1.5.1 Lap polishing processes (i.e., conventional methods)

Lapping and polishing are inherent conventional processes where the tool is larger than the substrate to fabricate optics of the desired shape, size, surface figures, and quality.

These processes involve the interaction of the workpiece with the lap through solid granular particles (slurry) mixed with a fluid in a four-component-mutually-interacting system, as shown in Fig. 1.3.

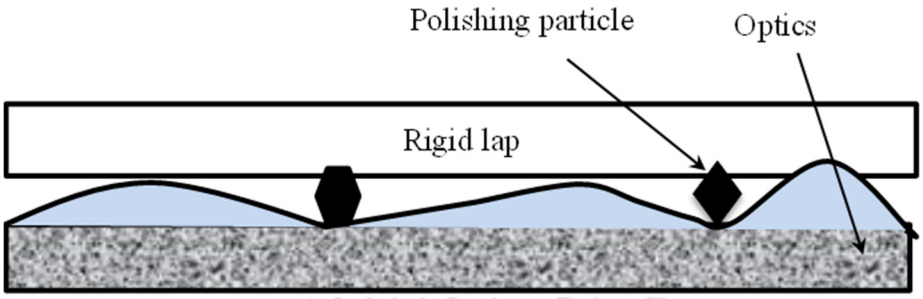

Fig. 1.3: Mutually interacting four components polishing system

1.5.1.1 Chemo-mechanical polishing (CMP)

The chemo-mechanical polishing process is widely used and matures among non/less-damaging polishing technologies. Super-smooth polished surfaces can be successfully obtained through mechanical and chemical reactions among abrasive, work-piece, and environment (Desai et al., 1994; Xie and Bhushan, 1996). These interactions can be on a macroscopic scale.

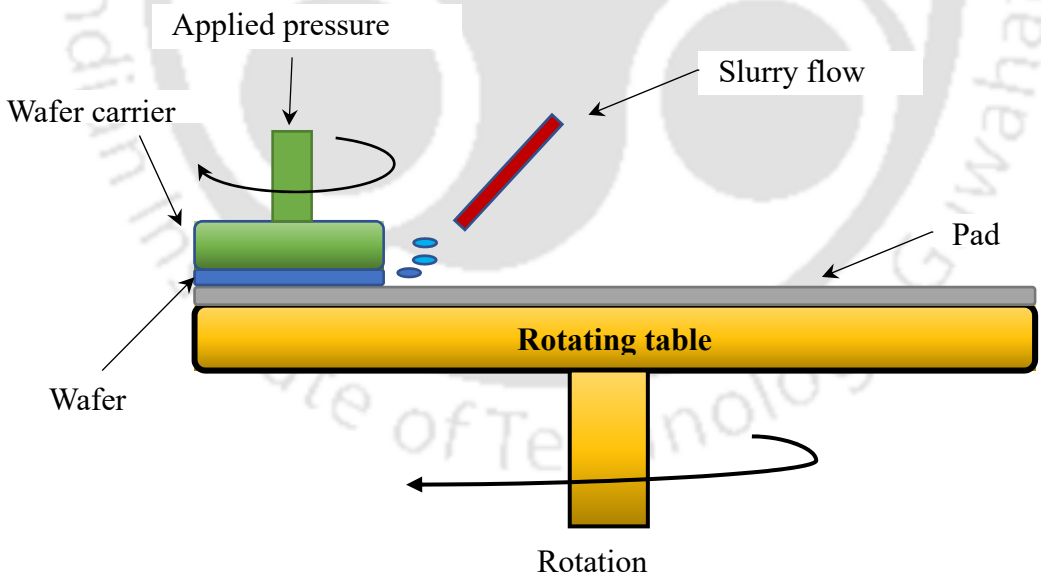

Fig. 1.4: Typical chemo-mechanical polishing setup

Also, in microscopic scales like dissolution, the workpiece is involved at the nanometer level laterally and vertically. The outcome of these interactions is given in terms of MRR, surface figures (flatness and roughness), and the workpiece's sub-surface damage

(SSD). The Fig. 1.4 shows the typical chemo-mechanical polishing set up used for polishing of optics with CeO2 as polishing slurry.

1.5.1.2 Pitch polishing

It is one of the most historical processes used for ages. Pitch is a very complex material. Limited information is available in the literature regarding the composition and properties of optical polishing pitch (Gillman and Tinker, 1999). Designs are primarily proprietary. It is generally understood that the material consists of various amounts of the following: residues distilled from tar, oil, or wood; rosin, a derivate of turpentine which comes from the sap of pine trees or stumps to increase melting point and tackiness; beeswax or linseed oil to the lower melting point: asphalt; flake shellac; paraffin wax; wood flour; or walnut shell flour. Essential properties are viscosity (started to be in the range of 10^7 to 10^9 Pa.s), the softening temperature in the field of 55-70^{0}C, penetration hardness (shore D by 60-80), coefficient of friction (tackiness), and groove pattern. After the glass is ground, it is integrated into a spherical viscoplastic pitch lap. Any tangential force applied to the workpiece will cause it to slide on the lap surface, which is wetted with a slurry containing abrasives. Here, the high spots are under more pressure and are removed preferentially. Therefore, the spherical surface is obtained almost automatically. The abrasives could be silicon carbide (SiC) used for rough grinding, aluminum oxide (Al_2O_3) used for fine grinding, and other compounds like cerium oxide (CeO_2) and zirconium oxide. The surface roughness that is achieved is 5.7 Å RMS for BK 7 with Al_2O_3 abrasives and 2.6 Å with CeO_2, 8 Å for flint glass with Al_2O_3 abrasives, and 0.8 Å with CeO_2 abrasives.

High metal removal rate (MRR) and easy lap preparation are the advantages of pitch polishing. The lap has to be frequently checked and corrected. Also, the pitch is volatile and sometimes acts as a fluid. Also, the abrasive media can sometimes be reactive to the surface. These are some of the disadvantages of the pitch polishing method.

1.5.1.3 Polyurethane polishing

Introduced in the ‘80s by Carl Zeiss Optics, it was developed due to the need for high-speed and finer accuracy in advanced engineering. Highly wear-resistant polyurethane polishing pads replaced pitch and cloth. The polyurethane lap is tuned to the desired shape on the workpiece surface (Li and Wang, 2009). During polishing, this master shape is copied on the workpiece at high speed. The rigid lap does not flow, so a relatively high number of workpieces can be polished by one lap before regrinding. The same slurry as the one used in pitch polishing is used here. Polyurethane is expected to perform better than pitch in

comparison to MRR. The MRR for BK 7 and fused silica are 10 and 4 µm/h. Better MRR and surface finish than pitch polishing are observed; however, occasionally, small pits and depression are also introduced during the process.

1.5.1.4 Teflon polishing

It is one of the fine-finishing processes where a low MRR is achieved. Before polishing a workpiece surface on Teflon, it must be polished using a pitch to remove all imperfections and grinding marks (Leistner et al., 1992).

1.5.1.5 Float polishing

Float polishing is done by rotating a tin lap with an aqueous polishing slurry of colloidal silicon oxide at high speed (Namba, Y., Tsuwa, H., Wada, 1987). Non-porous tin lap is one of the essential elements for the success of float polishing. The size of these abrasive polishing particles is 4-7 nm, in contrast to the conventional polishing particles of the order of 1 µm. The elastic bombardment by the polishing grain on the workpiece leads to the contact bonding and removal of weakly bonded atoms from the surface. The average surface roughness that can be experimentally obtained for some glass is Zerodur 8.5Å, fused quartz 11Å, and Cer-Vit 3.2Å.

1.5.1.6 Fixed abrasive polishing

This process can be adopted when lower-quality lenses are to be finished in large numbers. Plastic laps with pure water as a lubricant and sub-micron-sized CeO_2 as abrasives are used (Li et al., 2010). No unpredicted chemical slurry is required; it has a distinct advantage over polyurethane polishing. Besides higher MRR, CeO_2 is selected as an abrasive due to its high polishing efficiency for soft and moderately complex glasses. The average RMS that can be achieved is 2 nm. The advantages of this process are high polishing efficiency (high MRR per stroke of polisher), temperature stability, low cost of consumables, and compatibility, which reduces overall production time when employed in mass production. The main disadvantages of this process are that tool life is in hours, and the tool has to be checked for shape accuracy frequently.

1.5.2 Non-conventional polishing

The Conventional methods of fabricating optics are based on the delicate abrasive process. The material removal happens from the substrate due to abrasives, where a definite load is

applied between the abrasives and the machining surface. These processes use average load or shearing forces against the optic's character, which will induce stress on the surface and subsurface damage due to the brittle nature of the substrate. Some non-contact abrasive-based machining methods have been developed to overcome these problems where a tool is smaller than the substrate, such as float polishing, Elastic Emission Machining, ion beam polishing, etc.

1.5.2.1 Elastic emission machining

Elastic emission machining (EEM) (Mori et al., 1987) is one of the atomic-size machining methods. EEM is a machining method that utilizes particle surfaces' chemical activities instead of an etchant, as in chemical etching. EEM, machining properties mainly depend on the relationship between workpiece material and powder particles. EEM is performed by flowing a uniform mixture of ultra-fine powder particles having diameters much more minor than 1.0 micrometers and water on the machined surface. Powder particles are accelerated and transported to the work surface with a small average load to the surface through the flow. When they contact the workpiece surface, surface atoms are removed through the abovementioned process.

1.5.2.2 Ion beam polishing

The impact of energetic ions and atoms removes the surface atoms (Wilson and McNeil, 1987). It needs a vacuum pumping facility, gas medium lines, loading of workpieces, cooling of the system, and an ion beam source. During the sputtering process, ions collide with the substrate resulting in a cascade collision of atoms. The distance between the ion source and the workpiece holder is smaller than the mean free path length of ions, so the extracted ions will reach the workpiece without collision. A typical system may have a vacuum of 2×10^{-6} Torr or lower. The workpiece holder can be made with all the possible advances in mechanisms and with all the possible degrees of freedom. The best performance (cascade collision) happens when the ion beam incidence angle is between 45^0 and 60^0. This process can achieve an average surface roughness of 0.2 nm. The beam diameters can be 5 to 0.5 µm. The MRR can reach up to 1.050 $\mu m^3/s$. It is suitable for special-purpose applications, although it is expensive with limited availability and long polishing cycles.

1.5.2.3 Magnetorheological finishing (MRF)

Magnetorheological finishing (MRF) has been developed by the Center for optics manufacturing (COM) and QED Technologies in Rochester, N.Y., to automate high-precision optics polishing (Kordonski and Jacobs, 1996). MRF has demonstrated the ability to produce optical surfaces with surface roughness better than 30 nm peak-to-valley and less than 0.5 nm RMS on various optical glasses, single crystals, and glass ceramics (Golini et al., 1999). The MR fluid forms a polishing tool that is perfectly conformal and, therefore, can polish a variety of shapes, including flats, spheres, aspheres, prisms, and cylinders, with either round or rectangular apertures (i.e., finishing spot) without tool wear. Figure errors are corrected to a fraction of the wavelength of light, and subsurface damage is removed. Other applications in precision finishing are the polishing of integrated circuits and advanced ceramics. The MRF process relies on a unique "smart fluid" known as Magnetorheological (MR) fluid. MR-fluids exhibit dynamic field strength of 50-100 kPa for applied magnetic fields of 150-250 kA/m (~2-3 kOe) (Carlson et al., 1996).

Material removal occurs due to the shear stress created as the magnetorheological polishing ribbon is dragged into the converging gap between the part (lens) and carrier surface (moving wall). The zone of contact is restricted to a spot that conforms perfectly to the local topography of the part. Deterministic finishing of flats, spheres, and spheres can be accomplished by mounting the region on a rotating spindle and sweeping it through the spot under computer control, such that dwell time determines the amount of material removal. The MR-polishing fluid lap has the following merits over traditional lap: (a) Its compliance is adjustable through the magnetic field, (b) it carries heat and debris away from the polishing zone, and (c) it does not load like a grinding wheel and does not lose its shape as it is self deformable.

1.5.2.4 Reactive atom plasma (RAP) machining

The chemically reactive plasma jet is used to precisely shape optical and semiconductor surfaces by the reactive atom plasma (RAP) method. It is a dry chemical etching process. As material removal is done chemically, there is no subsurface damage. Computer numerical control RAP process can polish or correct precisely complex shapes. Energy associated with this process is considerably large, approximately 1 KeV, compared to the plasma process, which is typically less than 100 eV.

1.6 Plasma-assisted machining

As discussed above, the conventional polishing methods induce surface and subsurface damage to the optical substrate due to physical loading (Hed and Edwards, 1987; Lv et al., 2016; Wang et al., 2011). There are various non-conventional methods evolved to overcome the shortcomings of conventional methods. But these methods are not deterministic to obliterate subsurface damage and finish the optics with desired surface quality. The material removal rate (MRR) of EEM processes is meager, and the material removal mechanism is also abrasive-based; hence this method needs to be validated. Magnetic rheological finishing produces smoother surfaces at a lesser time but often contaminates the substrate, lowering the device's Laser damage threshold. Other prominent methods like ion beam polishing and reactive atom plasma processing utilize the chemical activity of the ions and radicals to remove material without subsurface damage from the fused silica substrate. However, these methods induce high thermal stress and affect the device's performance (Zhang et al., 2022).

Plasma-based polishing is an emerging technology. It utilizes the physical or chemical properties of ions/radicals for polishing fused silica without inducing any damage to the fused silica material. Plasma polishing is classified into two types depending on the operating pressure.

1.6.1 Low-pressure vacuum plasma polishing

Low-pressure plasma is known for its high MRR, and anisotropic plasma machining has been effectively used for such applications. As the pressure of the plasma increases, the isotropic property is gained, and the energy level keeps coming down the atmospheric pressure plasma in a low-energy isotropic plasma polisher.

1.6.2 Atmospheric pressure plasma polishing (APPP)

It utilizes chemical reactions between reactive plasma and surface atoms to remove atom-scale material. Since the process is chemical, APPP avoids various surface/subsurface defects that usually appear in conventional machining processes. Uniform low-temperature plasma can be generated over a large surface at a low cost and more extensive application range. Also, it quickly reacts with materials due to more active and multifarious species than those generated from chemical reactions. The reaction and plasma gas with the optimum ratio are sufficiently mixed and then input into the plasma torch. Then, ionized by the radiofrequency (RF) power, the reaction gas is excited in the plasma to generate high-density and high-energy reactive radicals. Then the generated reactive radicals cause

a chemical reaction with the surface atoms of the workpiece, which performs effective atom-scale material removal. For different materials, different combinations of plasma and reactive gas are used. Helium is used as plasma for silicon material, and carbon tetrafluoride (CF_4) is used as reactive gas. This gives a radical F* and SiF_4; volatile and machined surfaces are left with no contaminant. The principle of APPP is shown in Fig.1.5 shows how the reactive radicals combine with the surface atoms and volatile products are formed. The APPP method uses low-temperature plasma to avoid local high temperatures on the part surface. The temperature is just 90^0C as compared to 800-900^0C in ion beam polishing.

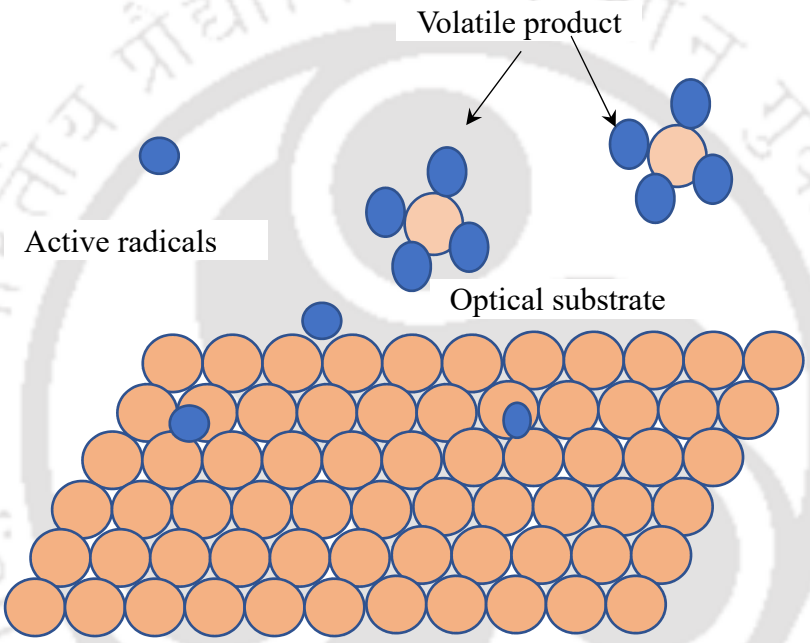

Fig. 1.5: Principle of atomic pressure plasma processing

The system's main components are a gas supply system, Radio Frequency (RF) power supply and impedance matching system, multi-axes worktable and relevant motion control system, hermetic chamber, and residual gas recovery system. But the main component is a plasma torch. The plasma torch is where the plasma and reactive radicals are generated. The plasma torch used is a capacitance-coupled RF plasma torch. The experimental value achieved till now is Ra of 0.631 nm or 6.31Å. This process is capable of attaining sub-nanometer average surface roughness. Also, the MRR is 32 mm^3/min, which is better than ion beam polishing. There are always certain defects on the final surfaces of the components formed in conventional contacting machining processes, such as micro-cracks, lattice disturbances, etc. Because of their unique characteristics, it is

severe for hard, brittle functional materials such as crystals, glass, and ceramics. The atmospheric pressure plasma polishing (APPP) method is developed to solve these problems.

Gerhard et al. (Gerhard et al., 2013) investigated the polishing of optical media by dielectric barrier discharge gas plasma at atmospheric pressure. Precision polishing of the sub-nanometer scale is achieved using dielectric barrier discharge at atmospheric pressure. The process gas used is Argon, with traces of oxygen. They have reported on significant topographic surface modifications on the optical media achieved. Approximately 20% reduction in surface roughness is completed, with an 80% improvement in waviness and increased surface energy on visual materials, including fused silica. The material removal is explained by ion bombardment and de-excitation of argon species. It is demonstrated that the plasma discharge causes high electric field strength at roughness peaks, initiating corrosion effects.

Li et al. (Li et al., 2019) have studied the surface changes in terms of surface modulus and hardness after atmospheric pressure plasma polishing and demonstrated improved surface mechanical properties. Nanoindentation tests were carried out to evaluate the residual stress on the surface before and after polishing. They showed decreased surface residual stresses as the deformed layer is removed atom by atom from the surface.

Jin et al. (Jin et al., 2010) investigated the impacting factors on the zerodur material surface roughness during APPJ processing. Also, the modification of the surface chemistry of Zerodur is studied as this material is based on multiphase-multi-chemical component nature. The relationship between substrate roughness and process parameters is reported based on experimental results. The processing gas used is He, O_2, and SF6, and the gas mixture ratio implication on the surface finish is also reported.

Yao et al. (Yao et al., 2010) reported on the chemical machining of Zerodur material with an atmospheric pressure plasma jet (APPJ). The paper discusses the consistency and spatial distribution of the chemically reactive part of the plasma jet. Atomic emission spectroscopy extensively studies the distribution of activated Fluorine atoms (radicals) and the material removal mechanism. Also, the material removal function is checked w.r.to work material, RF Power flow rate of SF_6, the ratio of SF_6/O_2, and working distance.

Zhang et al. (Jufan Zhang et al., 2008) have analyzed the mechanism of ultrasmooth surface formation due to APPP. Quantum chemistry simulation is done to explain the selectivity of APPP on surface topography and surface finish improvement mechanism.

Atomic Emission spectroscopy is used to study the plasma and to identify the control parameters in material removal. The low temperature encountered on the specimen and Ra surface finish of 0.63 nm is also reported. Li et al. (Li et al., 2003) discuss the effects of Ar and O_2 additives on SiO_2 etching in C_4F_8. Infrared laser absorption spectroscopy is used to study the etching functions under different operating parameters.

Coburn and Winters (Coburn and Winters, 1979) have studied ion and electron-assisted gas surface chemistry and its effect on plasma etching. An attempt has been made to evaluate the Ion enhanced gas-surface chemistry independently. Electron-enhanced gas-surface chemistry and a portion of their contribution to the chemical plasma material removal mechanism.

Zhang et al. (J Zhang et al., 2008) discuss a novel non-thermal Atmospheric Pressure Plasma for polishing SiC optics. Reactive gas such as CF_4 was introduced into the plasma area to react with the molecules at the surface of the SiC optics. As the interaction is a pure chemical process, the material removal is at the atomic, and no surface damage is caused. The theoretical analysis of the necessary conditions to generate the radicals also is presented.

Liu et al. (Liu et al., 2009) reported the novel plasma polishing process of fused silica developed in the laboratory of thin film techniques and optical tests at Xi'an University. Highly stable SF_6 and Ar plasmas are generated by the capacitive coupled hollow cathode radio frequency (RF) discharge method. Factors that affect plasma stability, such as gas flow rate, pressure, and discharge power, are investigated. The reported surface finish improvement is marginal from 1.2 nm to 1.0 nm, but surface integrity is enhanced. This is the only literature where effective plasma machining/polishing is done on bulk fused silica under low pressure (0.05 mbar). Also, the plasma source is operated in High Etching Rate (HER) mode and Low Etching Rate mode. HER method removes a surface and subsurface damaged layer, and LER mode is used to improve the surface finish.

A lot of research articles are available on non-conventional plasma processing for low-pressure and atmospheric-pressure plasma processing. However, medium-pressure plasma processing provides uniform radical distribution for the entire substrate and reacts chemically with the optical substrates. Hence, the classification of non-conventional processing is updated, as shown in Fig. 1.6.

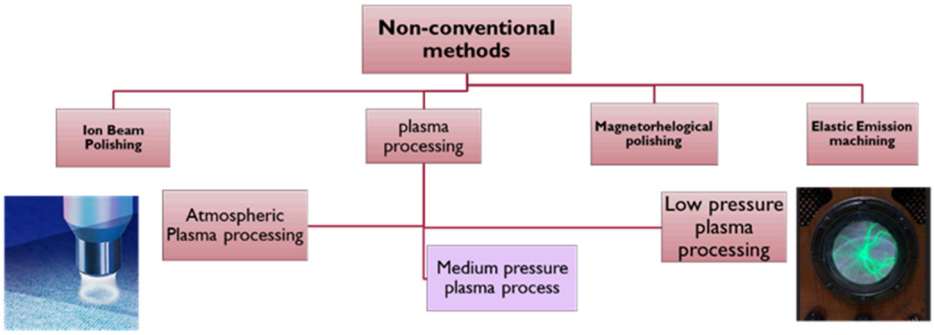

Fig. 1.6: Classification of non-conventional polishing methods

1.7 Gaps in literature

There is enough literature available regarding low-pressure plasma etching/polishing with custom-built industrial equipment and the machine also being available. Also, very active research is being carried out in atmospheric pressure plasma polishing for broader applications. However, low-pressure plasma processing is anisotropic, so surface topography cannot be improved. Also, radiation affects reduces the device's life. At the same time, atmospheric pressure plasma processing utilizes the chemical nature of the plasma to enhance the surface quality. But, low MRR makes this process time intensive and requires precise numerical control for uniform plasma processing. Hence, this method cannot be industrial-friendly due to higher polishing costs.

There needs to be literature available on the medium-pressure plasma polishing process. The medium pressure plasma processing carries the energy advantages of low pressure and chemical reactivity of the atmospheric plasma process. This region has the most interesting and exciting research possibilities for polishing fused silica optics. The medium pressure plasma processing is the competitive technology for polishing 3D freeform substrates much more cost-effectively. Fig. 1.6 shows the modified glass polishing non-conventional methods, which include plasma processing. This study explores the medium-pressure plasma processes and their advantages.

The plasma processes depends on the various parameters such as electron temperature, electron density, ion density, radical concentration, input power, total pressure of operation, chamber configuration, electode profile etc. Hence, it is esstential to simulate the plasma processes for optimizing the plasma parameters. Uchida and Hamaguchi, 2008 utilized the numerical simulation for single electron motion in RF field for evaluating the kinetic energy of the electron with electric field. Present study utilizes Comsol® multiphysics software module to predict electron number density for various configurations. Further, the

simulation results are experimentally validated using optical emission spectrometer (OES) results at different chamber positions.This study also adopted various characterization tools for accessing the surface and sub-surface chemistry and topography of the fused silica optics.

1.8 Objectives

This study aims to provide a solution for the machining and fabricating fused silica optics for high-end applications like aerospace inertial sensors like Hemispherical resonator gyroscopes and ring laser gyroscopes. There are various conventional fabrication methods exist for manufacturing fused silica optics. But these methods are not deterministic to achieve the quality of the optics. Hence, non-conventional methods emerged for fabrication. Specifically, optics polishing. Among the non-conventional techniques, much research was carried out on plasma processing last decade. The objectives of the present thesis are as follows:

- Development of a non-destructive method for quantifying the depth of damage of the ground optics and optimization of the machining parameters.
- Design and development of a medium-pressure plasma flow system to mitigate the damage during standard chemo-mechanical polishing.
- Investigation of characterization methods for quantifying depth of thin hydrated Bielby layer.
- Experimental investigation using medium-pressure plasma processing to replace the hazardous wet chemical etching without deteriorating surface topography.

1.9 Organization of thesis

Chapter 1 describes the brief literature survey of available glass and glass-ceramic materials fabrication methodologies. The need for non-contact machining to achieve the current complex requirement was generated. Among the various non-contact methods, plasma processing shows distinct advantages over the other methods. The basic information on plasma and the mechanism involved in material removal on multiple materials by a broad spectrum of plasma with varying characteristics were also studied.

Chapter 2 studied the advantages of medium-pressure plasma and the disadvantages of the confined system. A medium-pressure plasma flow system was designed and realized in-house. The sensitivity of flow meters concerning various gases was also studied. A

comparative study was made between the confined and plasma flow systems. The fluorine density remained constant for an hour of continuous operation, and a threefold increase in material removal rate was noticed for the plasma flow system. Moreover, there is a reduction in surface roughness and an increase in surface integrity of the fused silica substrate after plasma processing. Hence, the advantages of the plasma flow system were utilized for the subsequent studies.

Chapter 3 describes the optimization of chamber configuration using COMSOL® simulation for uniform plasma processing of free-form Hemispherical resonator shell.

Chapter 4 describes the in-situ and accurate monitoring method for the plasma polishing process using an optical emission spectrometer. In this process, the material removal rate has been monitored using different ionizing species silicon oxidation states generated in the plasma during plasma polishing. These silicon oxidation states are treated as in situ probe gases for monitoring the plasma interaction with the substrate during processing time. Silicon oxidation states accurately predict plasma and substrate interaction independent of processing and reactive gases.

Chapter 5 describes the quantification of the mechanically stressed layer depth of fused silica substrate, especially for brittle substrates like fused silica materials; the knowledge of machine-induced mechanical stress is essential for the performance and yield of the devices. In Hemispherical Resonator Gyro (HRG), which works with the principle of Coriolis force, the quality factor Q (defined as the ratio of the amount of energy stored divided by energy lost at every cycle) is a very critical parameter for the performance of gyro. Q factor depends on various factors, but for specific designs and materials, it is primarily proportional to the depth of damage to the optical substrate. Raman spectroscopy is the only reliable method to analyze the local mechanical stress in the micrometer depth scale for fused silica material. Hence, this method optimizes fused silica's rotary ultrasonic machining parameters and quantifies damage depth after the jig grinding process. This study optimized the cutting speed of 25 m/min, the feed rate of 100 mm/min, and the depth of cut 5 µm to shape fused silica substrate using Rotary Ultrasonic machining.

Chapter 6 covers the characterization methodology for quantifying the depth of damage of ultra-precision fused silica optics. The Secondary Ion Mass Spectrometer (SIMS) method was adopted for quantifying the depth of the Beilby layer based on metallic composition. Chemical defects like color centers' presence were analyzed using a fluorescence spectrometer. This chapter also includes experimental methods for removing

the defects layers formed during fine abrasive polishing without altering the surface finish and improving the surface chemistry; it is validated using a fluorescence spectrometer.

Chapter 7 includes the experimental study of wet etching compared to plasma polishing for fused silica optics. This chapter shows the advantages of medium-pressure plasma processing over hazardous wet chemical etching. **Chapter 8** delts the work's overall summary and future scope, followed by references.

Chapter 2
Medium-pressure plasma finishing

2.1 Introduction

The word plasma describes microscopically neutral substances containing many interacting free electrons and ionized atoms or molecules. In other words, plasma, called the fourth state of matter, is a partially ionized gas with an equal number of positive and negative particles; overall, the plasma remains electrically neutral. The plasma mainly contains free radicals, which are chemically reactive and responsible for material removal. The plasma processing depends on various parameters such as processing time, total operating pressure, processing gas, partial pressure of each gas, applied electrical field, etc. But the plasma process is broadly classified into low-pressure, medium-pressure, and atmospheric-pressure plasma processing depending on the total operating pressure. With the increase in force, the plasma characteristics also vary hence, the applications. At low pressure (< 0.00001 bar), the plasma acts as a conventional glass polishing tool where the entire substrate is treated simultaneously. At low-pressure plasma, the mean free path is higher. Hence, the physical action of the ion is dominating factor compared to a chemical reaction. Hence at low-pressure, plasma processing is anisotropic. On the other hand, at atmospheric pressure (~1 bar), the mean free path of the partially ionized electrons is less, so the plasma

act as a non-conventional polishing sub-aperture tool. At this pressure, the chemical action is the more dominating factor; hence, primarily, the reaction is isotropic. At medium pressure (0.02 to 0.1 bar), the plasma carries the advantages of both low and atmospheric pressures. At medium pressure, the plasma can be controlled such that it reacts with the substrate chemically, unlike low-pressure plasma, and simultaneously the entire substrate, unlike the atmospheric plasma process. Hence, it is the most cost-effective and reliable processing method compared to other functions. The complex 3D freeform surfaces can be polished simultaneously by optimizing the plasma parameters of medium-pressure plasma processing. Table 2.1 shows different plasma processing systems' advantages, disadvantages, and applications. The table shows that the medium-pressure plasma processing can be controlled to achieve desired properties of the optics without inducing surface or subsurface defects. Hence, medium-pressure plasma processing is preferred in this study.

Table 2.1: Plasma pressure Vs. polishing application

Types of plasma processes	**Low pressure**	**Medium pressure**	**Atmospheric pressure**
Plasma distribution	Plasma is evenly distributed inside the plasma chamber.	**Plasma can be made evenly distributed inside the chamber**	Plasma confined to a small area
Processing of 3 D free form objects	All items in the plasma chamber are treated simultaneously. Also, cavities can be treated from the inside.	**All surfaces can be treated uniformly and simultaneously. Also, cavities can be treated from the inside wide aperture.**	Local surface treatment is possible for 3D free-form surface treatment complex, and control maneuver is essential.
Surface integrity and surface finish of Optics	Surface topography remains the same or deteriorates	**There is no change or improvement in surface topography based on parameters but improving surface integrity**	There is improvement in surface integrity and surface finish
Mechanism of material removal	Ion physical action	**Chemical reaction**	Chemical reaction
Disadvantages	Requires complex vacuum technology	**Requires Control flow system**	Can apply to local area treatment only

Dev et al. (Dev et al., 2018, 2016) established a method for plasma polishing complex free-form surfaces using medium-pressure dielectric glass barrier capacitive coupled

discharge. It combines high-pressure plasma's chemical phenomena and low-pressure plasma's energy to replace etching and contact polishing without generating subsurface defects. This plasma process successfully eliminates sub-surface damage, reduces surface waviness, and improves surface quality (Dev et al., 2016). However, the above process has a few limitations, like the material removal rate (MRR) being insignificant, only about 8×10^{-3} mm^3/min. Hence, this method cannot be considered a wet chemical etching replacement. Multiple experiments were conducted with an accumulative plasma machining time of about 300 minutes to accomplish a uniform reduction in substrate thickness of about 1 µm from the substrate surface with 8×10^{-3} mm^3/min MRR. The total material removal expected during the process at 8×10^{-3} mm^3/min MRR for 300 minutes is 35% lesser. It suggests that throughout the experiment, the MRR is not uniform. Hence, a new plasma flow system has been developed in this study to achieve higher MRR and uniform material removal throughout the fused silica substrate surface during plasma processing.

2.2 Observations in closed medium-pressure plasma

The closed medium pressure plasma system is simple, operation friendly, and easy to characterize and control the plasma parameters. But this system faces the following drawbacks.

- **Need for expensive vacuum systems:** The above procedure needs vacuum leak tightness better than 10^{-10} mbar lit./sec during plasma processing, or else plasma chemistry will change during processing.
- **Requirement of chamber cleaning:** As plasma reactions happen in a closed system, the reactive gases contaminate the chamber by reacting with the components. Hence it is very tedious and time-consuming to clean the chamber post-plasma process.
- **Meager material removal rate:** The closed system allows the machining with a substrate for significantly less than the actual processing time. The plasma chemistry, pressure, and gas composition of the chamber change with time during plasma processing. Hence material removal rate decreases significantly with time. This leads to low (0.016 mm^3/min maximum) MRR, so time-consuming and not cost-effective. The material removal rate is negligible compared to conventional polishing.

- **Reduction in material removal rate with time:** The material removal rate depends on the reaction of free radicals with the substrate. In a confined system, the new free radicals cannot approach the substrate surface due to the presence of volatile byproducts. Hence, there is a reduction in the material removal rate with time.

2.3 Design of medium-pressure plasma flow system

The plasma flow system is designed and developed in-house to overcome the drawbacks of the closed system. In this chapter, details of the plasma flow system and the comparison of this system with the previous plan are briefed. The plasma machining flow system schematic layout is shown in Fig. 2.2. It has provisions to handle four gases simultaneously during plasma machining with the following features.

- The flow rate of the gases can be controlled simultaneously with the digital flowmeter.
- The chamber can provide machine samples of 5 mm to 40 mm in diameter with a height of up to 40 mm.
- Chamber is made up of dielectric material; hence, electrodes can be placed outside the chamber, allowing the section's purity during machining.
- The transparent chamber allows the monitoring of plasma chemistry by emission spectrometer.
- The system can operate at any constant pressure ranging from 0.1 to 100 mbar without increasing pressure during machining.

The system consists of the following essential elements for having the above features:

- **Mass flow meter:** The system contains four Teledyne Hastings make mass flow meters (MFC) to simultaneously enable the flow of four gases as shown in Fig. 2.1. These flow meters are calibrated concerning indented gases. The gas regulators connect the high-pressure cylinders (150 bar) to the mass flow meters. This gas regulator ensures constant pressure at the mass flow meters input and protects the MFCs against the high pressure (ensures < 2 bar at MFC input end). The mass flow meters are connected to the chamber through hermetic-sealed Swagelok connectors.

(a) (b)

Fig. 2.1: (a) Teledyne Hastings mass flow meters and (b) VAT make gas dosing valve

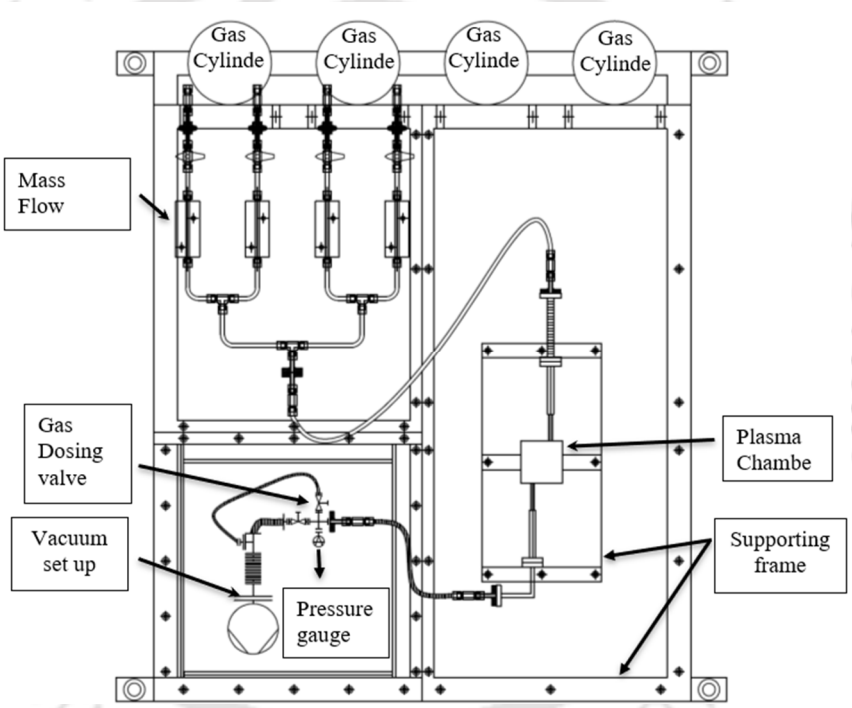

(a)

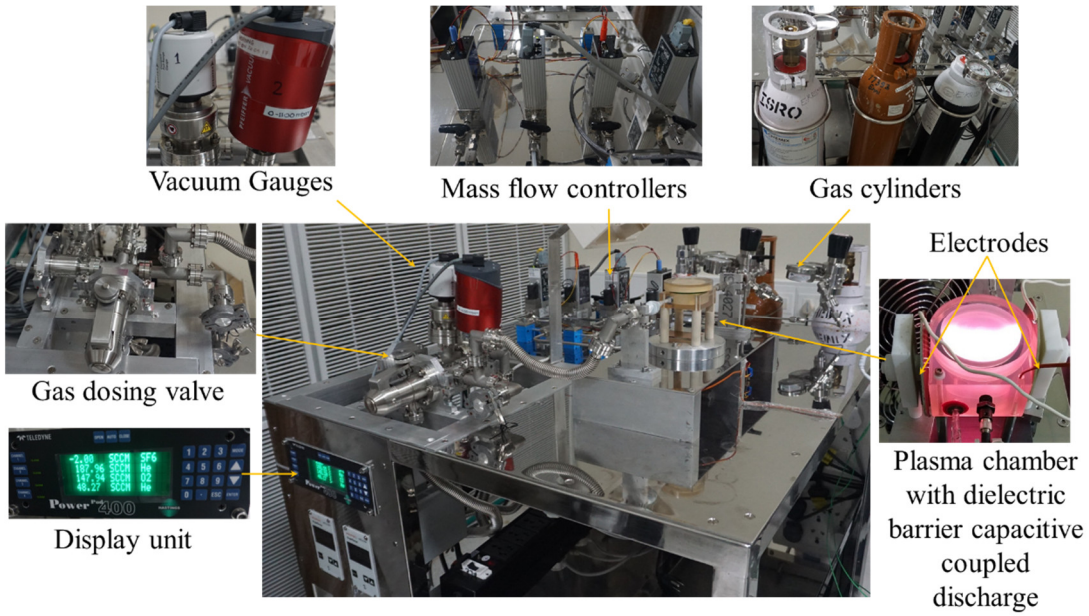

(b)

Fig. 2.2: Plasma flow system (a) schematic layout and (b) actual photograph

- **Digital mass flow controller:** A mass flow controller digitally controls the four mass flow meters simultaneously. The flow rate also can be set independently for individual flow meters.
- **Plasma chamber:** The plasma chamber comprises glass-ceramic material for enabling dielectric barrier discharge and ensuring plasma purity during machining. The four MFC gas flow tubes merged into a single flow line using Swagelok T-joint as shown in Fig. 2.2. The chamber was also hermetically sealed through Viton make O-ring but designed such that the O-ring physically separated from direct plasma contact.
- **Gas dosing valve:** The fine control gas dosing valve is inducted to ensure constant pressure during plasma machining. This connects to the chamber at one end, and the other end interfaces with a vacuum gauge for identifying pressure inside the room. The chamber pressure can be achieved through the rotary pump.

2.4 Optimization of system parameters

As explained above, the main feature of the flow system is flow meters and controllers. Hence, it is essential to characterize and optimize the parameters before the plasma machining. The mass flow meters' functionality depends on various parameters such as

input pressure, type of gas, set flow rate, etc. In this section, the optimization of these parameters is discussed.

2.4.1 Input pressure

Table 2.2 shows the total chamber pressure variation at a given flow rate. No change in full pressure was observed, with a significant difference in input pressure. It suggests that chamber pressure depends on the flow rate and is independent of input pressure. It provides more tolerance to work continuously.

Table 2.2: Variation of chamber pressure with input pressure for a given flow rate

Measured SCCM	Total chamber Pr. @0.1 kg/cm^2 input Pr.	Complete chamber Pr. @ 10000 kg/cm^2 input Pr.
10	7.8	7.7
15	10.8	10.7
20	13.7	13.6
30	18.8	18.7
40	23.4	23.4
50	27.5	27.4
60	31.5	31.5

2.4.2 Characterization of response of each gas with flow rate

Figure 2.3 shows the response of each gas with MFC with a different flow rate. The change in chamber pressure was analyzed with a sweep in flow rate until 110 SCCM. It shows that chamber pressure increases linearly with an increase in flow rate. But it is interesting to note that individual gases have a different responses concerning the flow rate for an MFC. The figure suggests that oxygen gas is more sensitive to flow rate, where chamber pressure increases more than other gases. It may be due to the chemical affinity of the oxygen gas. Whereas sulfur hexafluoride is the minor response to the flow rate, an increase in chamber pressure is the minimum among the three gases with a sweep in flow rate. It may be due to the large size, leading to flow resistance. While helium is, the inert gas flow rate falls between O_2 and SF_6.

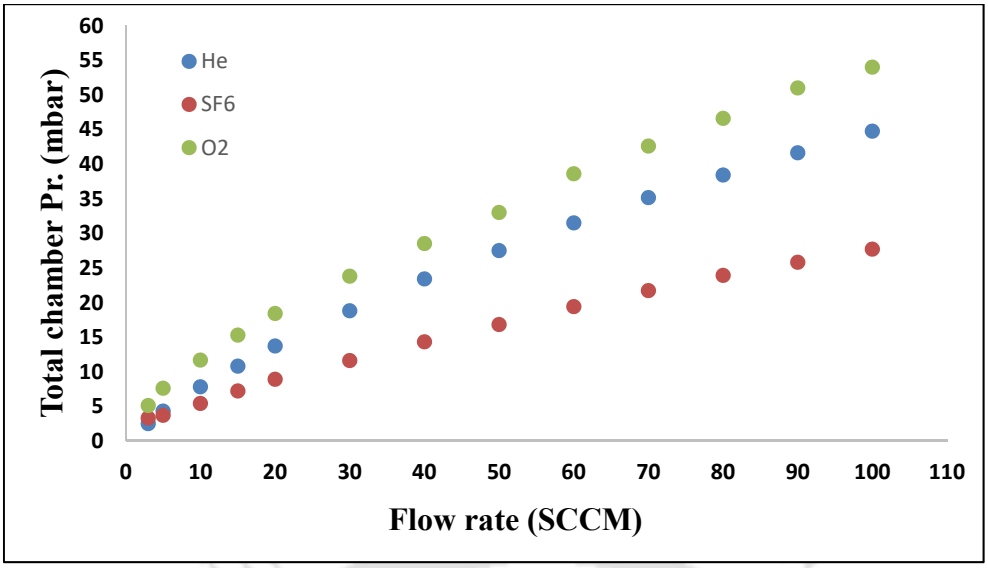

Fig. 2.3: Total chamber pressure at different flow rates for different gases

2.4.3 Feasibility of usage of gas composition as old set up

The gas optimization was done based on the experience of the previous setup. Table 2.3 shows the strategy of gas composition and flow rate optimization. Hence, good control flow meters were incorporated to achieve optimum gas composition as an old configuration. Hence, the need for fine mass flow controllers was established. New fine mass flow controllers were obtained, and the system was upgraded. With this system, it is possible to achieve similar optimum composition as the old configuration.

Table 2.3: Comparison between old and new configurations of polishing chambers

	Old configuration for 20 mbar total pressure		**Required flow rate for new configuration**		
	Composition (%)	Pressure (mbar)	Flow rate (sccm)	Composition (%)	Pressure (mbar)
He	96.25	19.25	30	86.5	60
SF6	1.25	0.5	<0.5	6	3
O2	0.25	0.25	<0.25	7	6
			Total Pressure 35 mbar hence, Not possible with this flow meter		

2.5 MRR comparative study

Plasma processing with a closed system shows less material removal rate; moreover, the material removal rate is not uniform throughout the experiment. Hence in the present study, a new plasma flow system is developed to improve the material removal rate to achieve sustainable uniform material removal over the entire component surface during plasma processing.

2.5.1 Experimental setup

The present experimental setup consists of a plasma chamber to polish components having a size between 5 to 40 mm. Also, the uniform generation of reactive gases is considered while designing the chamber (Dev et al., 2018). The photograph of the plasma polishing system with a vacuum system and different gas units required for plasma processing is shown in Fig. 2.2. The magnified view of the plasma chamber is also shown in Fig. 2.4. Zerodur is used to fabricate the plasma chamber. The chamber is sealed with an optically transparent lid plate for 300 to 1200 nm wavelength. Figure 2.4 shows the photographs of both old and new configurations. There is a lot of technical and dimensional difference between both configurations.

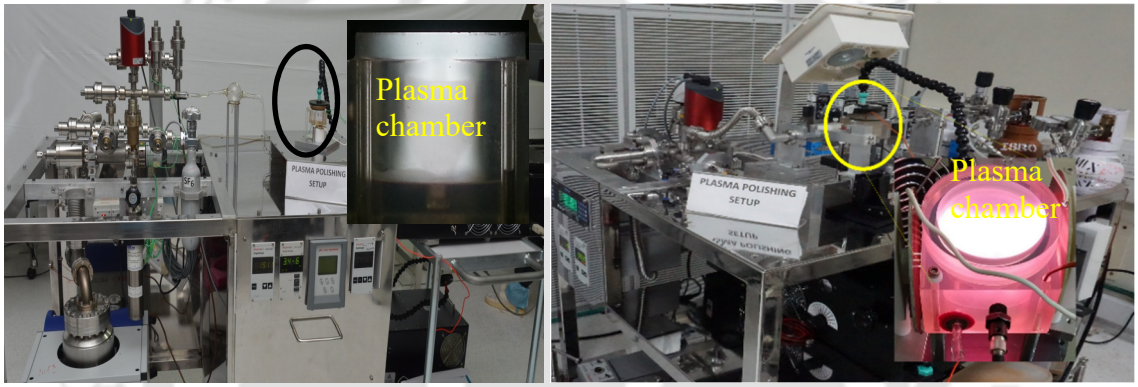

(a) (b)

Fig. 2.4: Photograph of (a) old and (b) new configurations of experimental setup

The vacuum pump is connected to the chamber with different tubes for feeding reactive and processing gasses. To avoid ion impingement, medium vacuum pressure is considered. Also, to minimize electron heating, dielectric barrier radio-frequency (RF) excitation is selected to permit chemical interaction by the reactive free radicals with the workpiece's surface atoms. The excitation frequency of RF is determined as 40.68 MHz to minimize the bombardment of the ion. Optical emission spectroscopy is applied to analyze the light-emitting photons during plasma processing. Plasma processing is carried out at 40W excitation power and 20 mbar total pressure with gas composition of 96.25% He, 2.5% SF_6, and 1.25% O_2. The processing parameters are chosen from a confined plasma system studied by Dev et al. (2018). In this paper comparative study is made concerning the continuous gas flow system versus the confined plasma system, whereas other processing parameters are kept constant.

2.5.2 Design of experiments

This study uses experiments on a fused silica sample of 20 mm length, 20 mm width, and 2 mm thickness as a substrate. The pieces are shaped to the required dimension using the abrasive cut machine. Two samples are identified for processing in the new plasma flow system and previously studied closed system. Each set contains four different pieces for processing with different time duration. The plasma processing duration is 5 mins, 10 mins, 15 mins, and 20 mins of continuous operation.

Surface roughness is analyzed before and after plasma processing using Talysurf surface analyzer for all the substrates. The surface stress of the substrate is analyzed using confocal Raman microscopy illuminated with a 532 nm laser. This study uses Optical emission spectroscopy to understand plasma chemistry during processing.

2.5.3 Analysis of MRR

Figure 2.5 shows the MRR of the samples with time. MRR is about 200% higher in the new plasma flow system than in the confined plasma system. MRR decreases linearly with time for the previously studied confined plasma system. There is improvement in MRR observed after post-cleaning. It infers the deposition of specific contamination during plasma processing in a confined system. On the other hand, there is a linear increase in MRR for the new continuous flow system till 15 mins, and MRR remains unaltered for further processing with time.

Calculation of difference in MRR

Maximum MRR for confined system = 0.01 mm3/min

Maximum MRR for flow system = 0.03 mm3/min

Percentage difference in MRR = 200%

Hence, the MRR for flow system is 3 times higher than the confined system, which is 200%.

There is an improvement in MRR for substrates processed in the confined system after ultrasonic cleaning. Substrate surfaces were analyzed using Raman microscopy to understand the depositions after plasma processing. Figure 2.6 shows the overlay of the Raman spectrum after processing for ten minutes in a confined and plasma flow system. Raman spectrum revealed carbon and oxygen-based contamination peaks for confined systems after plasma processing. It suggests that contaminations get adsorbed during plasma processing in a confined system on the fused silica substrates, which hampers the fluorine radical from approaching the fused silica substrate.

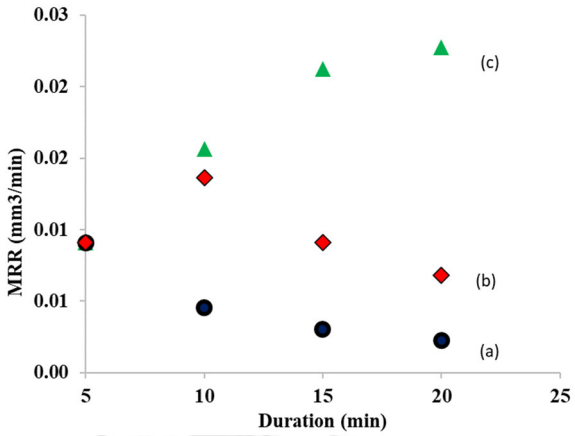

Fig. 2.5: The material removal rate for the samples processed in (a) confined plasma system before post-cleaning, (b) confined plasma system after post-cleaning, and (c) new continuous gas flow system.

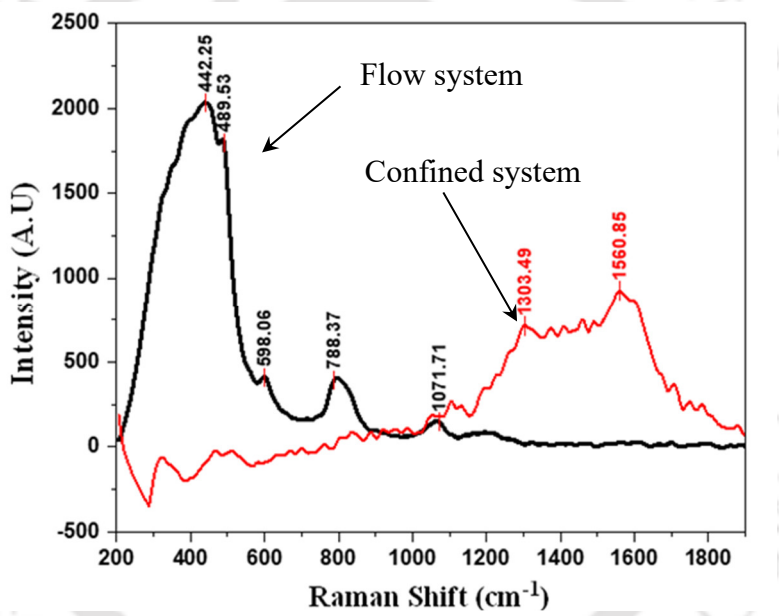

Fig. 2.6: Raman spectrum overlay on substrate surface processed in confined plasma and continuous gas flow systems without cleaning

Figure 2.7 shows the schematic representation of the plasma processing mechanism for confined and newly developed plasma flow systems. In a confined system, the reactive gas is filled in the chamber and processed by the sample by applying an external field. During initial plasma processing, fluorine radicals/ions react with Si-O bonds of fused silica substrate and form volatile silicone tetra-fluoride (SiF_4). But with time, as the reaction proceeds temperature of the chamber also increases, causing the sealing O-ring to emit carbon atoms. These carbon atoms spread and cover the entire fused silica surface, which hinders reactive fluorine ions/radicals from approaching and reacting with Si-O bonds of the fused silica substrate, as shown in Fig. 2.7. Hence, the material removal rate decreases

with time for a confined system. Meanwhile, new radicals/ions constantly react with the substrate for the plasma flow system since the system's pressure is made constant with the help of a controlled leak valve throughout the reaction.

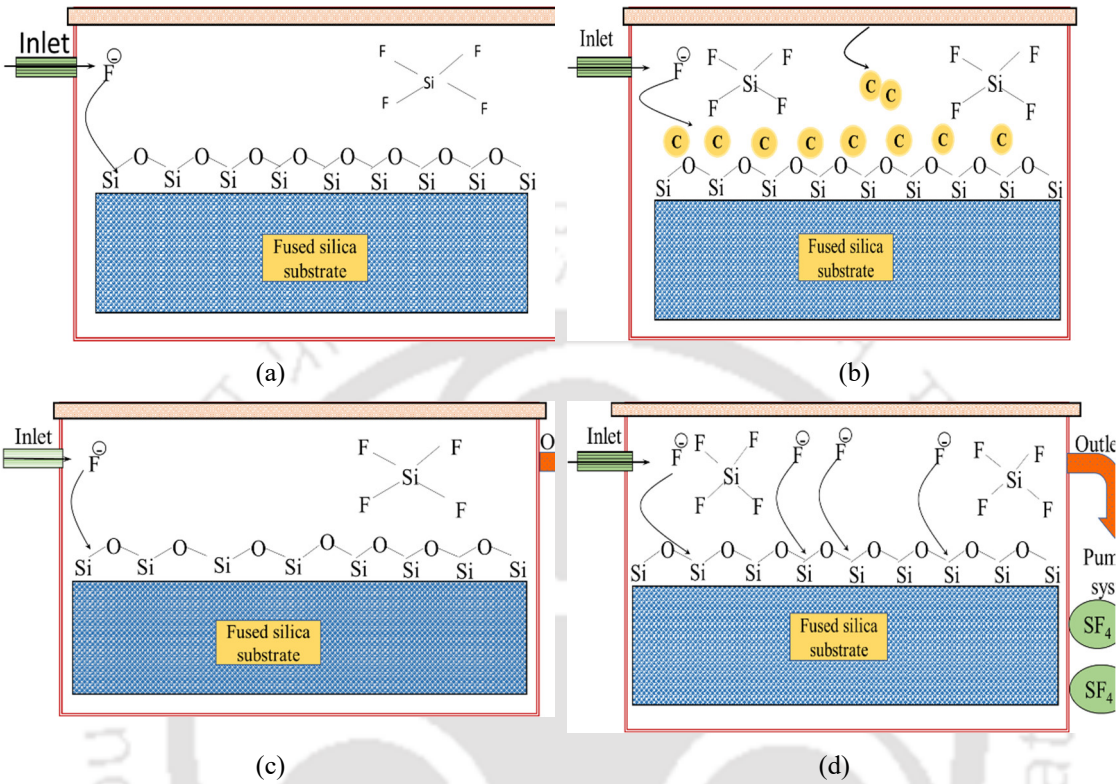

Fig. 2.7: Schematic representation of the mechanism of plasma processing (a) in the confined system at the initial stage (at time t = 0) and, (b) in the confined system after 20 mins of processing time, (c) in plasma flow system at the initial stage (t = 0) and, (d) in plasma flow system after 20 mins of processing time

2.5.4 Analysis of plasma chemistry

Plasma chemistry during plasma processing plays a vital role in MRR. Optical emission spectroscopy (OES) is a crucial non-invasive diagnostic tool for understanding plasma chemistry. Using OES plasma spectrum recorded continuously at the interval of two mins. The intensity of the characteristic peaks of Si, F, and He processed for 5 minutes are plotted in Fig. 2.8. In Fig. 2.8, the typical peak intensities of Si, F, and He for (a) a new continuous flow system and (b) confined plasma system. Characteristic radical/ion peak intensities decrease significantly with time for medium-pressure confined systems, whereas, as mentioned earlier, powers increase with time for identical pressure plasma flow systems.

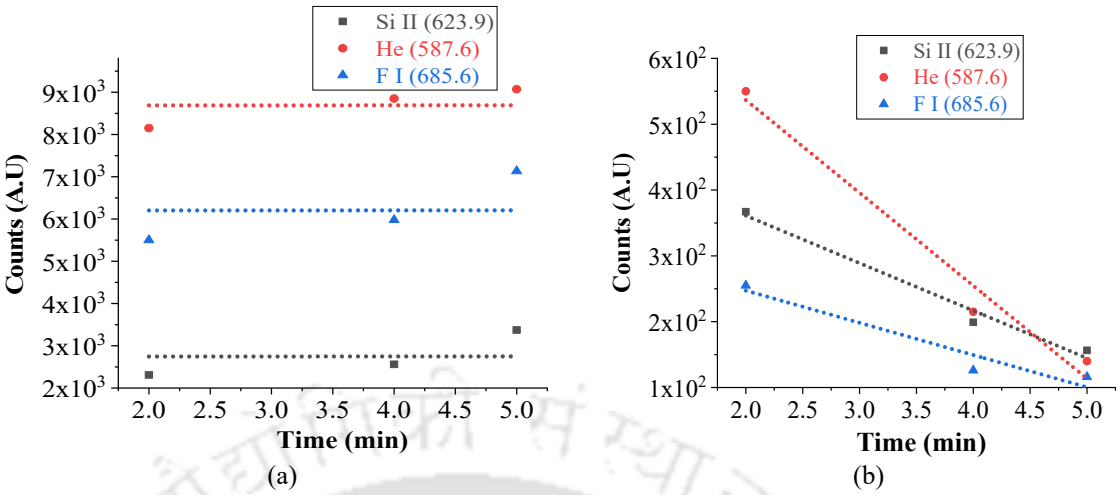

Fig. 2.8: Emission spectrum intensities of plasma processed for 5 mins continuously in (a) continuous gas flow and (b) confined plasma system

Figure 2.9 shows characteristic peak intensities of Si, F, and He for (a) a new continuous flow system and (b) a confined plasma system for 10 minutes of a continuous process. Characteristic peak intensities decrease with time (Fig. 2.9 (b)) for medium-pressure confined plasma systems. For a continuous flow system, distinct peaks of F and Si increase with time during processing; however, peak intensity decreases marginally after 8 minutes. Generating more silicon and fluorine radicals may reduce the gain for Helium radicals.

Similarly, Fig. 2.10 shows characteristic peak intensities of Si, F, and He for (a) a new continuous flow system and (b) a confined plasma system for 15 minutes of continuous operation. Fig. 2.10 (b) shows a similar trend as in Figs. 2.8 (b) and 2.9 (b). It suggests that machining happens only in the initial few minutes for a confined system. Hence, MRR decreases continuously with time, as shown in Fig. 2.5. For the newly developed continuous flow system, the radical intensities of fluorine and silicon increase with time during processing.

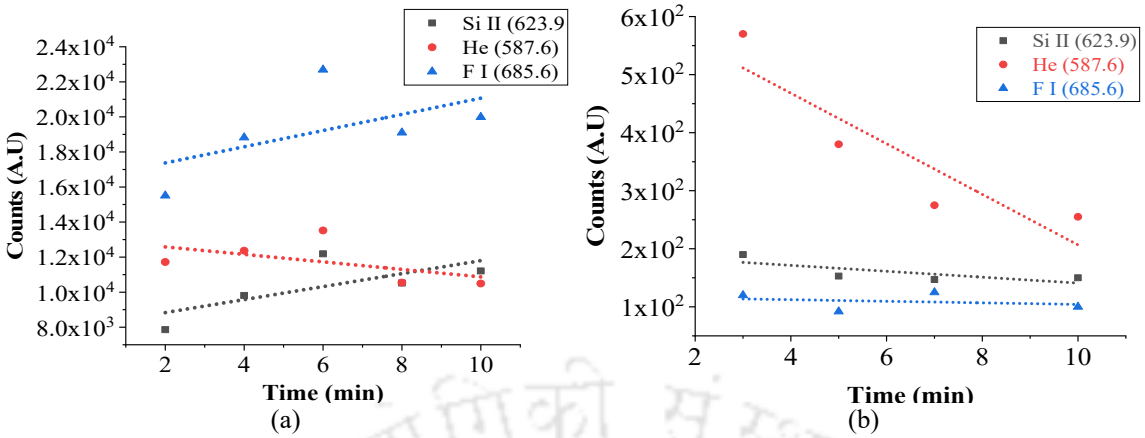

Fig. 2.9: Emission spectrum intensities of plasma processed for 10 mins continuously in (a) continuous gas flow and (b) confined plasma system

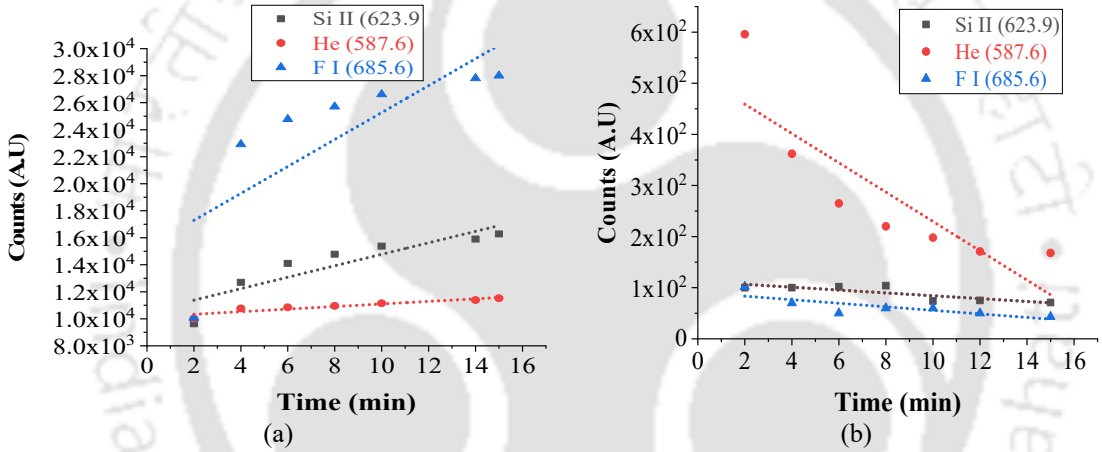

Fig. 2.10: Emission spectrum intensities of plasma processed for 15 mins continuously in (a) continuous gas flow and (b) confined plasma system

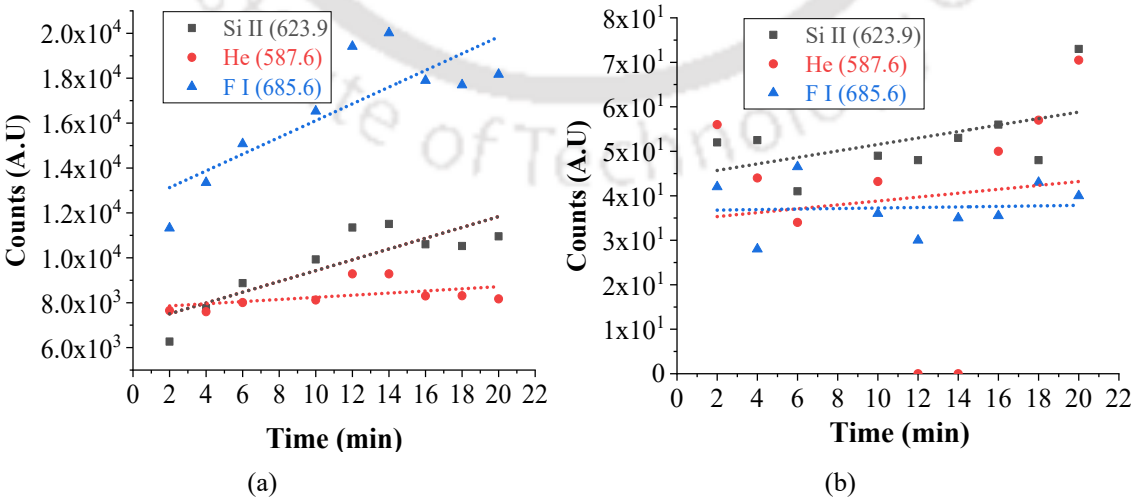

Fig. 2.11: Emission spectrum intensities of plasma processed for 20 mins continuously in (a) continuous gas flow and (b) confined plasma system.

Hence, MRR also increases linearly till 15 minutes. Emission spectroscopy results explain the enhancement of MRR in the case of a continuous flow system compared to a confined system. The Fig. 2.11 shows the characteristic peak intensities of Si, F, and He for (a) a new continuous flow system and (b) a confined plasma system for 20 minutes of continuous operation. The continuos flow system shows the constant MRR as 15 mins of operation. On the otherhand the plasma intensity in confined system reduces significantly, thus, no machining activity.

2.5.5 Surface chemical network analysis

Raman spectroscopy is an ideal tool for the structural modification characterization of fused silica. Fused silica shows a broad Raman band centered at 440 cm^{-1} is related to the perfect six-membered Si-O-Si angle distribution (Galeener and Geissberger, 1983). However, due to the induced mechanical strains during contact polishing or machining brittle fused silica, two characteristic Raman bands centered at 495 cm^{-1} (D1) and 605 cm^{-1} (D2) are found. These defect peaks indicate the formation of five and four-membered rings. Raman spectroscopy can analyze damage to fused silica surfaces by considering the intensity and area under these bands, which reflect the disruption of the tetrahedron Si-O network (Liu et al., 1997). An increase in the number of these rings results in a decrease in overall bond angle, increased density, and surface stress.

Surface and sub-surface stress are critical functional criteria for optics performance. As MRR is higher for the present flow system, surface stress analysis is essential in certifying the process. Confocal Raman microscopy analyzes all the samples processed with time in the new flow system. Table 2.4 shows the substrate's characteristic Raman peak intensities at different durations. It shows that the ideal six-membered 440 cm-1 amplitude is higher for plasma-processed fused silica samples than for the unprocessed reference sample. However, at the defect peak, D1, the peak intensity is higher for the unprocessed reference sample than the processed sample.

Figure 2.12 indicates that the relative intensity of 440 cm^{-1} versus D1 and D2 peaks increases linearly with processing time. It suggests that stress-induced defect peaks decrease, and the ideal six-membered concentration increase with time. Hence, the fused silica sample's surface integrity improves with time during plasma processing.

Table 2.4: The intensity of Raman peaks of fused silica samples processed at different time duration with the present flow system as compared to the unprocessed substrate

Sample description	Intensity 440 cm^{-1} peak	The intensity of 490 cm^{-1} peak (D1)	Intensity 603 cm^{-1} peak (D2)
without processing	31531	34060	1580
5 min processed	64769	21450	1807
10 min processed	102321	27218	2237
15 min processed	181087	27093	2862
20 min processed	104988	11875	1286

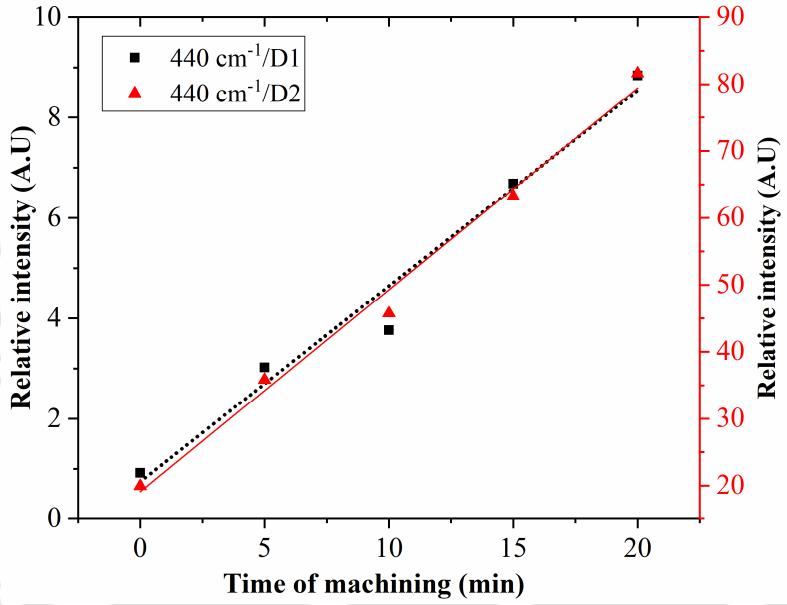

Fig. 2.12: Relative intensities of 440 cm^{-1} peak concerning defect peaks D1 and D2 of fused silica samples processed inflow system with time

2.5.6 Surface finish analysis

The surface roughness of the samples processed with time in the new plasma flow system is analyzed before and after plasma processing. Figure 2.13 shows the surface profile comparison of the substrates processed before and after 5 minutes. A 5% improvement in the surface finish was observed after 5 minutes of continuous plasma processing. Moreover, it shows that before plasma processing, the surface spread's peak to valley (PV) is from 2 to 20 µm, while after processing, the PV surface spread is limited to 4 to 10 µm only. These results suggest that peaks are eliminated by plasma processing. Hence, it confirms that plasma processing improves the surface finish.

Figure 2.14 shows the surface profile of the substrate before and after plasma processing for ten continuous minutes, which offers a similar trend as 5 mins processed

sample. There is an 11% improvement in surface finish observed after plasma processing. Similarly, Fig. 2.15 and 2.16 show the substrate surface profile processed for 15 and 20 mins, respectively. Both the cases' surface roughness values got improved after plasma processing.

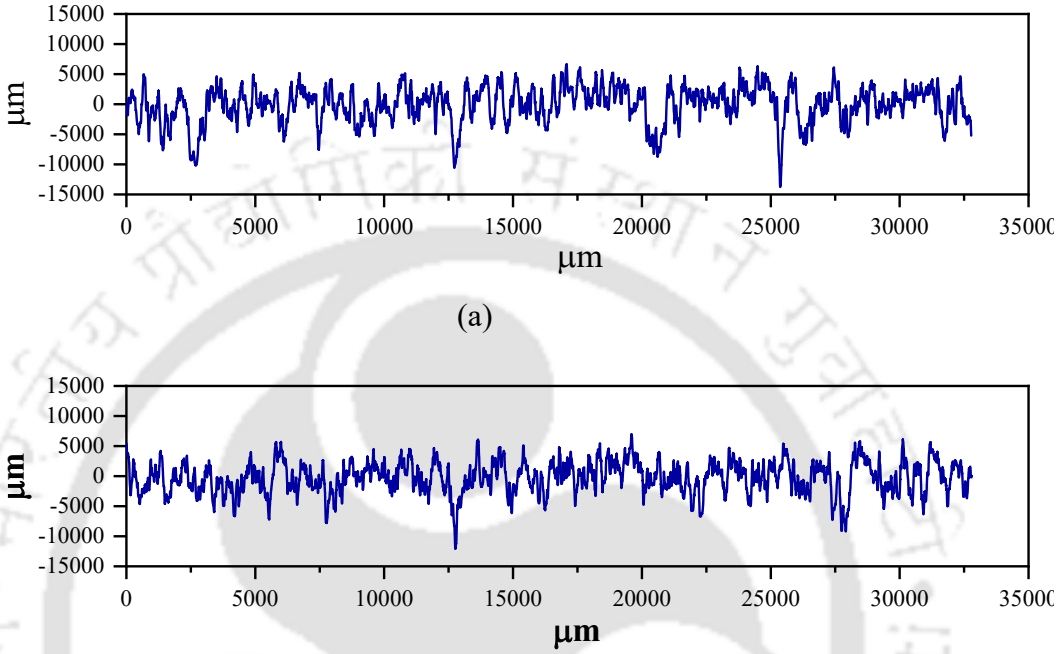

(a)

(b)

Fig. 2.13: The surface profile of the substrate (a) before and (b) after 5 mins of plasma processing

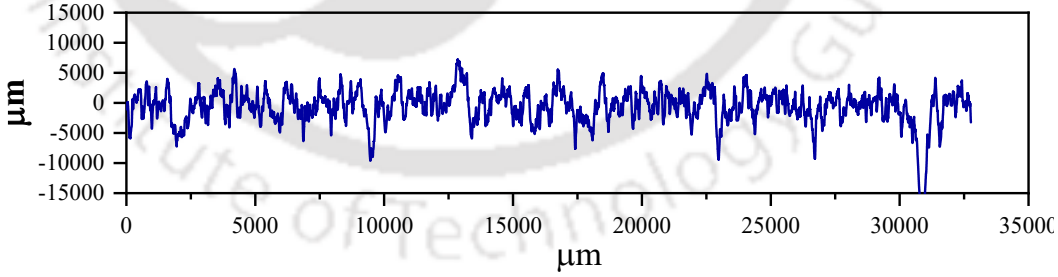

(a)

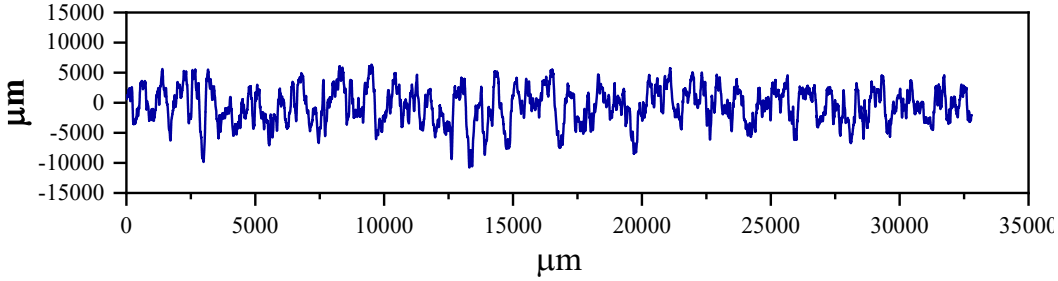

(b)

Fig. 2.14: The surface profile of the substrate (a) before and (b) after 10 mins of plasma processing

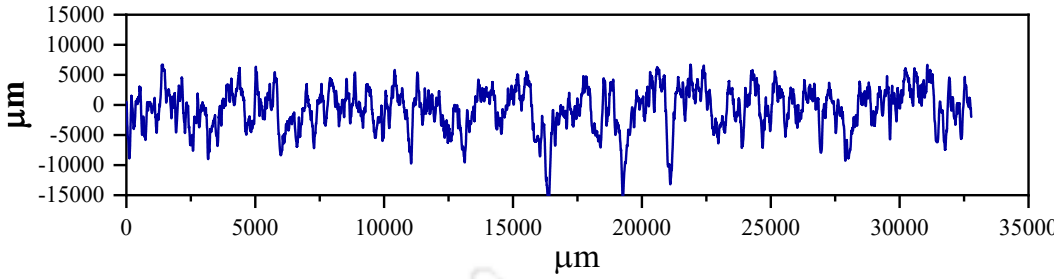

(a)

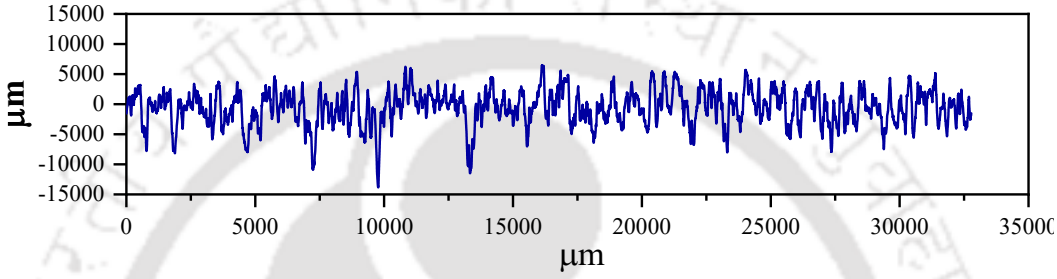

(b)

Fig. 2.15: The surface profile of the substrate (a) before and (b) after 15 mins of plasma processing

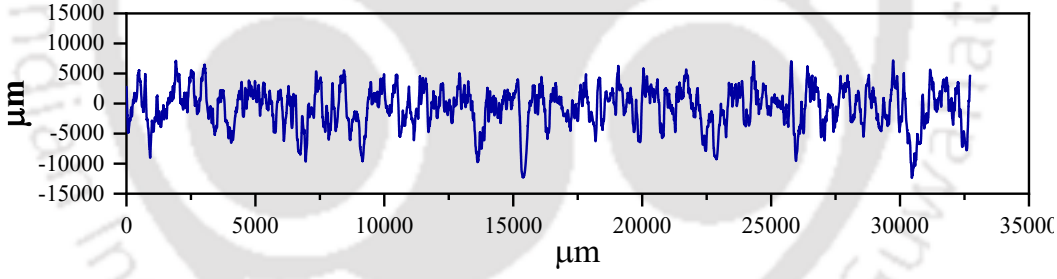

(a)

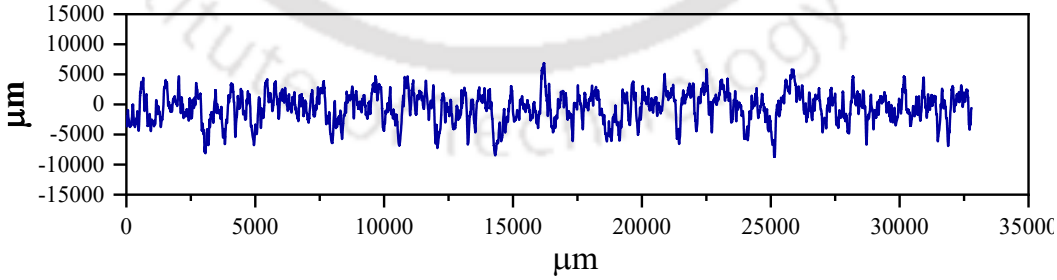

(b)

Fig. 2.16: The surface profile of the substrate (a) before and (b) after 20 mins of plasma processing

Table 2.5 describes the average surface roughness value of fused silica substrates processed with different time durations. Results suggest that surface finish gets improved

with processing time. The results show an improvement in the surface topography of fused silica substrate with plasma processing, unlike atmospheric plasma processing, as demonstrated by Duo et al. (Li et al., 2019) and Qiang et al. (Xin et al., 2015). Surface finish results suggest that medium-pressure plasma processing preferentially removes the surface peaks compared to others. This study is in line with the investigation made by Dev et al. (Dev et al., 2016) using medium-pressure plasma processing. It may be due to the peaks experiencing higher ion/radical concentration at the elevations than valleys. Hence, the peak-to-valley difference has reduced, and the surface finishes improved with plasma processing.

Table 2.5: Surface roughness value of sample before and after processing of the samples processed at different time durations

Sample description	Ra, before processing	Ra, after processing	% change in Ra
5 mins continuous processed	1.7	1.6	5
10 mins continuous processed	1.8	1.6	11
15 mins continuous processed	2.0	1.5	25
20 mins continuous processed	1.9	1.6	16

2.5.7 MRR comparison study for longer machining time

Long-duration plasma processing is mandatory to eliminate subsurface damage layers incurred due to mechanical machining. To meet long-duration matching sustained material removal rate is essential. Hence, a comparative study was made for the fused silica substrate from 5 to 60 minutes.

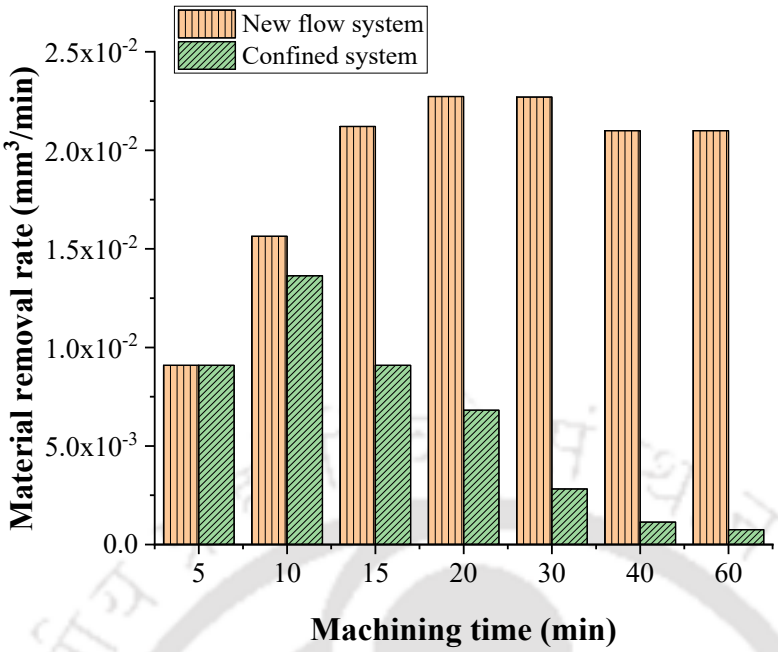

Fig. 2.17: Comparisons of MRR for both systems for 60 mins of operation

Figure 2.17 shows a comparative MRR graph for a longer operation time for both systems. It suggests that The MRR reduces significantly with time after 10 mins of operation. It may be due to the generation of more contaminations and the unavailability of new fluorine radicals for reaction with the fused silica substrate. On the other hand, the MRR increases with time till 10 mins for the newly developed plasma processing system, and MRR remains constant at 0.022 mm^3/min beyond 15 mins. It suggests that the flow system enables the removal of reacted fluorine radicals and ensures the availability of fresh fluorine radicals constantly at the fused silica substrate, as shown in Fig. 2.7. The above mechanism confirms the sustained material removal rate beyond 60 mins, which helps achieve a longer operation time.

2.5 Summary

A continuous gas flow system has about 300% higher MRR than a confined system with the same processing condition like the same pressure, composition, and input power. Plasma chemistry analysis during plasma processing validates the enhancement of MRR. Optical emission spectroscopy of plasma with a continuous flow system shows a linear increase in fluorine radicals with time. It suggests continuous machining of fused silica with time in the constant flow system. On the other hand, fluorine radicals' concentration decreases significantly within a few minutes of operation for the confined system. Even if

there is a higher MRR, a 5 to 20 % improvement in the surface finish is observed after plasma processing in the continuous flow system. Raman analysis results confirm the enhancement of surface chemistry with time after plasma processing with a constant flow system. Overall, there is an improvement in surface integrity and a reduction in time of operation with the newly developed plasma flow system. Moreover, the plasma flow system enables a sustained material removal rate for a longer operation time of 60 mins and beyond.

Chapter 3

Comsol® simulation for uniform plasma polishing of free-form surfaces

3.1 Introduction

The conventional chemo-mechanical polishing (CMP) process cannot be adopted for components like hemispherical shells with complex surfaces. Therefore, there is a need to develop a polishing process that replaces the role of wet chemical etching and CMP on components having freeform/complex characters like in the hemispherical shell. Hence, the demand for advanced non-contact type polishing is growing daily. Among non-contact polishing methods, plasma-based machining is an effective technique for sub-nanometer finishing brittle optics, thanks to its chemical interaction with the silicon-based substrates (Dev et al., 2018, 2016). During plasma processing, active radicals generally react with the substrate surface and remove the material uniformly on the atomic scale. Hence, radical distribution plays a prominent role in uniform plasma polishing. Simulating the plasma is essential; moreover, numerical simulation helps in many ways during plasma processing (Uchida and Hamaguchi, 2008). A thorough understating of plasma chemistry is attained by comparing simulation results with experimental observations. The number of time-consuming experiments can be avoided by optimizing plasma processing parameters using computer modeling of the process. These simulated results are used in the manufacturing processes. Electron density and temperature are fundamental parameters in gas discharges and play an essential role in understanding the discharge physics and optimization of plasma operation (Lieberman and Lichtenberg, 2005; Chen, 1984). This paper uses the Comsol® multiphysics software module to predict electron number density for various

configurations. Further, the simulation results are experimentally validated using optical emission spectrometer (OES) results at different chamber positions.

3.2 Experimental setup

A two-dimensional transient study uses a microwave plasma (MWP) module of Comsol®. The system's temperature and pressure are considered 300 K and 25 mbar, respectively, during plasma processing. The plasma in the system is assumed to be static. The following species are used during simulation; (a) active radicals as He*, O1d, O_2a1d, O_2b1s, and O1s, (b) neutral atoms/molecules as O_2 and He, and (c) reactive ions as O_2^+, O, e, O^+, and He^+. As the plasma is partially ionized and neutral, the number density of electrons and ions is considered equal. However, the radicals are generated at the latter stage of the reaction. Hence, radical densities are assumed to be negligible.

3.2.1 Computational domain and boundary conditions

The geometry of the 2D computational domain is designed as per the proposed experimental setup. The cross-sectional area in the setup is distinguished into three parts: electrodes, plasma, and dielectric bodies as shown in Fig. 3.1. The setup dimension is considered as 55×40 $mm^{2,}$ and the dielectric thickness is taken as 5 mm. A hemispherical shell of SiO_2 (i.e., fused silica) is kept at different positions in the chamber for simulation.

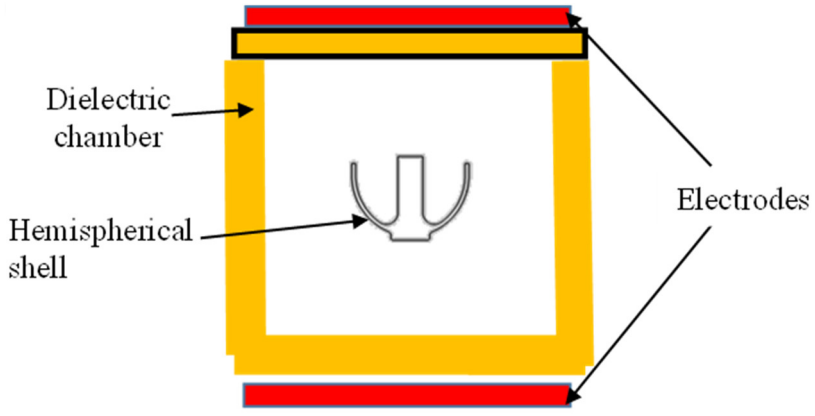

Fig. 3.1: 2D Computational domain of plasma chamber with the hemispherical shell inside

The free triangular finer mesh is considered to simulate charged particle collision at walls and physics-controlled reaction at the substrate interface. The plasma is contained within four boundaries of the chamber, considered borders. These four walls are grounded

for boundary surface reactions. Radiofrequency (RF) is applied to one of the electrodes, while others act as a ground for plasma excitation (Dev et al. 2018). The present simulation adopts the square wave RF signal for plasma excitation with 40 W power. Different transient analyses are adopted with various positions of the hemispherical shell with or without support with two different configurations of the electrodes, as explained in the computational domain.

3.2.2 Comsol® simulation results

Transient analysis is carried out using Comsol®, and steady-state has been achieved within one second. Hence, in the present study, the condition of the plasma inside the chamber is considered for 1s for all cases. The distribution of electron number density (n_e) is studied as discussed below. Uniform electron distribution surrounding the hemispherical shell is required for consistent machining throughout the workpiece surface. This study also examines uniform radial distribution with different shell configurations.

Figure 3.2 shows the electron number density distribution surrounding the hemispherical shell kept at the center (a) without and (b) with dielectric support. It is observed from Fig. 3.2 that the electron distribution pattern is similar for both cases. Hence, the dielectric stand has not affected the electron density distribution. However, for both cases, electron distribution is not uniform. About 70% more electron density inside the hemispherical shell than on the outer side may cause non-uniform machining and further deterioration of form accuracy.

Figure 3.3 shows n_e distribution of the hemispherical shell kept at the bottom of the plasma chamber in (a) regular and (b) inverted fashion. From Fig. 3.3, it is observed that for both configurations, the n_e distribution is non-uniform. Although, interestingly about a 20% increase in n_e is observed for the first configuration (Fig. 3.3 (a)), which is kept regularly, and a 20% reduction for the other one (Fig.3.3 (b)) as compared to to the one which is held at the center (Fig. 3.2). The inversely kept shell at the plasma chamber may obstruct the gas flow and input field, hence, results in less n_e than Fig. 3.3 (a) which is kept as a cup facing up. However, n_e distribution is more uniform inside the substrate in the case of an inverted configuration than in the standard configuration. These results suggest that the change in the position of the shell inside the plasma chamber does not affect the uniformity of n_e distribution. Hence, further simulation is carried out by changing the chamber configuration to achieve uniform electron distribution.

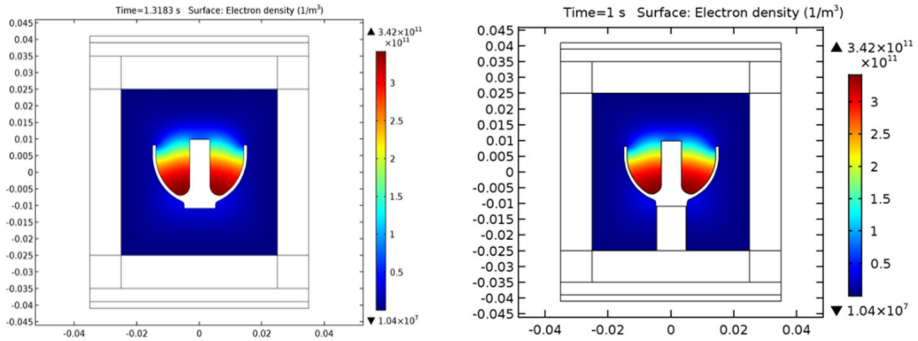

Fig. 3.2: Electron number density distribution surrounding the hemispherical shell kept at the center (a) without and (b) with dielectric support

Figure 3.4 shows n_e distribution surrounding the hemispherical shell kept at the center with (a) a dielectric customized stand, (b) a dielectric customized stand and V-shaped chamber, and (c) a hemispherical shaped chamber. Different customized chamber configurations are conceived to achieve uniform electron distribution. The calculated electron density is about 2 fold less for these configurations (Fig. 3.4) due to the reduction in the free volume of the chamber as the customized stand is induced than previous configurations (Fig. 3.2). The decrease in free volume causes more uniform n_e distribution for the entire substrate. However, the average number density comes down due to reduced molecule count. Among the three configurations shown in Fig. 3.4, the hemispherical-shell-shaped chamber configuration (Fig. 3.4 (c)) provides more uniform plasma distribution throughout the shell. However, the electron density is much lower (about one order less) than in other configurations. The realization of this configuration is practically difficult. Moreover, this chamber (Fig. 3.4 (c)) is substrate-specific. Hence, it cannot be considered for practical use. The configuration having a customized stand with a V-shaped chamber (Fig. 3.4 (b)) has shown a more uniform n_e distribution than the customized stand configuration (Fig. 3.4 (a)). However, the n_e distribution for design in Fig. 3.4 (b) is not uniform inside the hemispherical shell, although the percentage of non-uniformity is less than in other configurations. Hence, this configuration (Fig. 3.4 (b)) is optimized for plasma processing.

Table 3.1: Electron density with different shell positions, configurations and chamber configurations

	n_e distribution ($1/m^3$)	**Remark**
Shell position and configuration		
Shell dielectric support	3.42×10^{11}	
Shell without dielcric support	3.42×10^{11}	**n_e** was not affected by dielectric support
Shell regular fashion	4.21×10^{11}	20% increase in n_e is observed for this configuration compared to others
Shell in inverted fashion	2.21×10^{11}	
Shell with dielectric customized stand	8.27×10^{10}	
Chamber configuration		
Shell with dielectric customized stand and V-shaped chamber	8.29×10^{10}	More uniform distribution without change in **n_e** density
Hemispherical shaped chamber	1.79×10^{9}	Difficult to fabricate

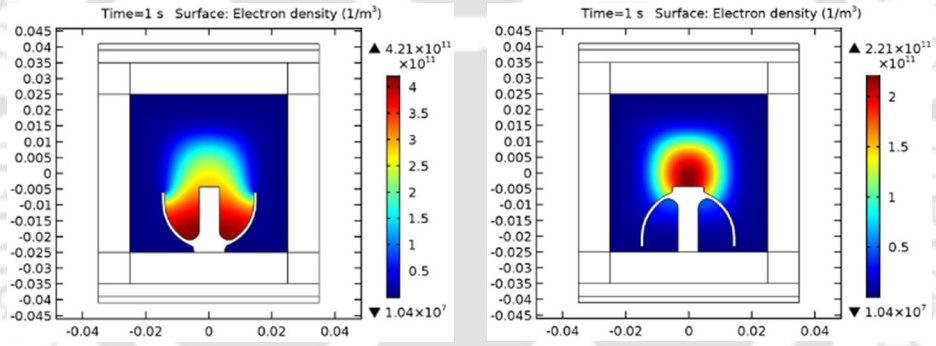

(a) (b)

Fig. 3.3: Electron number density distribution surrounding hemispherical shell kept at the bottom of plasma chamber with (a) regular and (b) inverted fashion

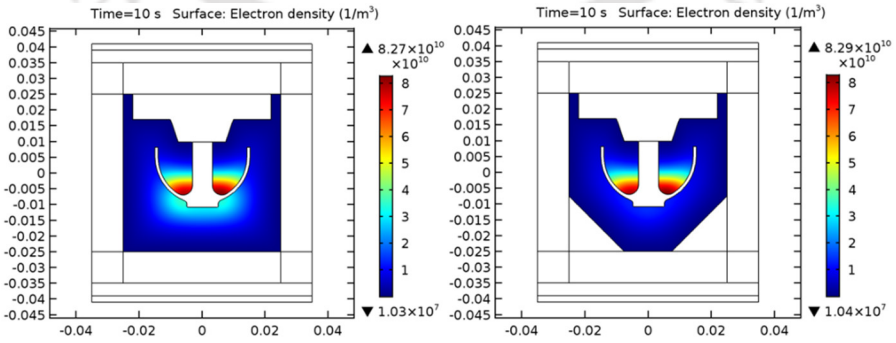

(a) (b)

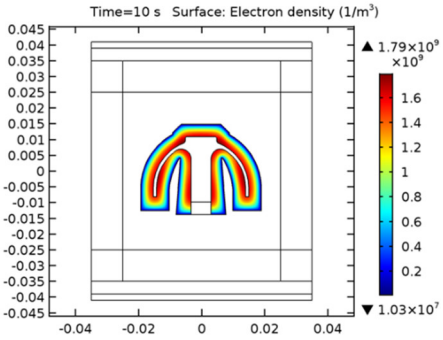

(c)

Fig. 3.4: Electron number density distribution surrounding hemispherical shell kept at the center with (a) dielectric customized stand, (b) dielectric customized stand and V-shaped chamber, and (c) hemispherical shaped chamber

3.3 Design of plasma chamber and validation of Comsol® model

In the present study, the results obtained from Comsol® simulation are validated based on the experimental spectroscopic measurement of electron density. The plasma chamber is designed based on Comsol® simulation results. Also, the uniform generation of reactive gases is considered while creating the chamber. The photograph of the plasma polishing system with a vacuum system and different gas units required for plasma processing is shown in Fig. 3.5. Also, the magnified view of the plasma chamber is shown in Fig. 3.5. Zerodur (dielectric glass-ceramic composite) is used to fabricate the plasma chamber. The chamber is sealed with an optically transparent lid plate for wavelengths 300 nm to 1200 nm. The vacuum pump is connected to the chamber with different tubes for feeding reactive and processing gasses (Fig. 3.5). The excitation frequency of RF is 40.68 MHz to minimize the bombardment of the ion. Optical emission spectroscopy is applied to analyze the light-emitting photons during plasma processing. In plasma, the outer shell electron of the atoms is excited to higher energy states by collision with free electrons. The excited state is unstable. Hence, the atom emits the absorbed energy through electromagnetic radiation. The emitted wavelength is related to power as per Plank's equation.

$$\lambda = hc/\Delta E \qquad (3.1)$$

Where λ is emission wavelength, ΔE is the difference in energy between two electronic states, h is Plank's constant, and c takes care of light speed. The plasma's relative densities and atomic transition are distinguished depending on the measure with the atomic spectra database of the National Institute of Standards and Technology (NIST).

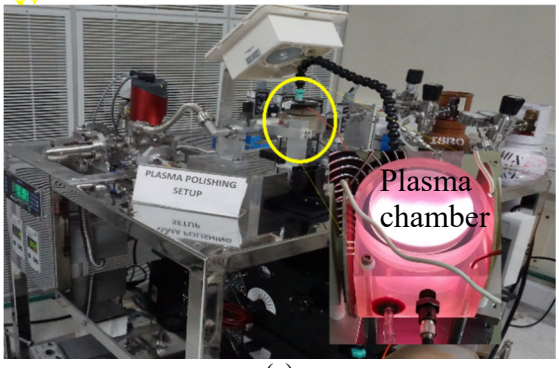

(a)

Fig. 3.5: Experimental setup of plasma polishing system and magnified view of the plasma chamber

3.3.1 Electron density measurement

Electron collisions in the plasma system play a vital role in plasma-chemical kinetics. Hence, electron density measurement is essential for the plasma system (Boudam et al., 2006). Among several diagnostic methods for measuring the plasma electron density, the plasma spectroscopy based on either Stark broadening of spectral lines or the Saha Boltzmann equation (Griem, 1997; Unnikrishnan et al., 2010) is well established. This study uses the Stark broadening of spectral lines method for electron density calculation and the following equation (Brugeat and Coitout, 2004).

$$\ln n_e = 1.2\ln(\Delta\lambda_{1/2}) + 44.2476 - 0.6\ln(T_e) \tag{3.2}$$

Where $\Delta\lambda_{1/2}$ is full-width-half-maximum of the selected wavelength and Te is electron temperature. Equation (3.2) suggests that electron density depends on the electron temperature of the plasma system. Hence, it is essential to calculate the electron temperature of the plasma.

3.3.2 Electron temperature measurement

In the present study, the line ratio method of the OES technique is adopted, where the emission line's intensity ratio is related to the temperature of the electron by a method called the collisional-radiative model (CRM) (Zhu and Pu, 2008). This method is generally used for medium and low-pressure plasma (Crintea et al., 2009; Kano et al., 2000; Zhu et al., 2009). The electron temperature is calculated as (Zhu and Pu, 2008).

$$T = \frac{(E_1 - E_2)\times\left(1/k\right)}{\ln\left(\frac{I_1}{I_2}\right) - \ln\left(A_1 g_1 \frac{\lambda_2}{A_2 g_2 \lambda_1}\right)} \tag{3.3}$$

Where A is Einstein's coefficient of respective transition, E is the energy of change, g is the degeneracy of state, I is the intensity of transition, and λ= wavelength. The value of Boltzmann's constant (k) equals 1.38×10^{-23} J/K. The wavelengths considered here are λ_1=706.52 nm and λ_2=667.82 nm. λ_1 and λ_2 are selected based on transition probability. These peaks have transition probabilities higher than other He transition; hence they are more intensive and sensitive to the analysis. Table 3.1 shows the spectral properties of the wavelength chosen for electron temperature calculated as shown in Eq. (3.3).

Table 3.2: Spectral line properties of the selected wavelength

Spectra line	Wavelength	Transition probability$\times10^{-7}$s^{-1}	Statistical weight	Energy of excited state eV
He I	706.5179	1.541	3	20.96 - 22.72 (L-U)
He I	667.8152	6.380	3	21.22 - 23.07 (L-U)

Figure 3.6 shows the different positions of the plasma chamber for measuring electron temperature to understand electron temperature distribution during plasma processing and (b) measured temperature at those positions. Figure 3.6 (b) shows a temperature difference of only about 20K throughout the chamber, indicating its uniform distribution during plasma processing.

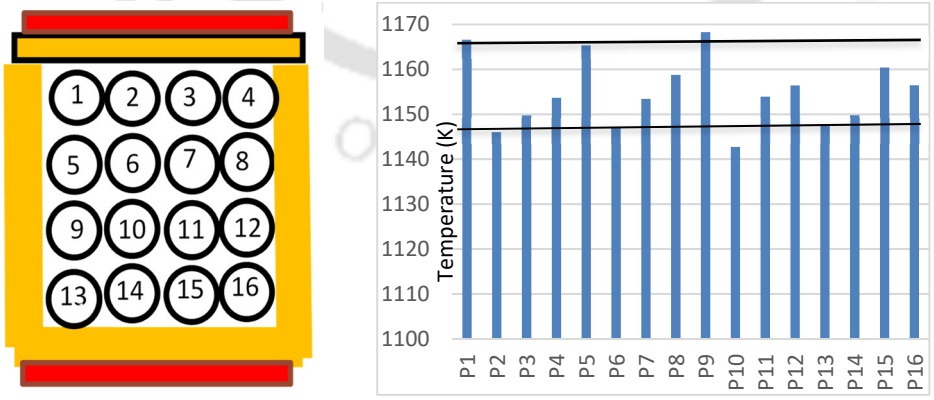

(a) (b)

Fig. 3.6: (a) Different positions of plasma chamber to measure electron temperature and (b) measured temperature at those positions

3.3.3 Calculation of full width and half maximum of spectral line

For the calculation of electron density, the full-width half maximum (FWHM) of the spectral line should be calculated. In this study, a high-resolution echelle grating spectrometer is used for characterization. It utilizes NIST data and Stark-broadening parameters for the calculation of FWHM. Figure 3.6 shows the spectrograph of the He 667.8 nm transition line (He I λ=667.8 nm ($1s2\ ^1S_0 - 1s2p\ ^1P_1$). The FWHM is derived from being 37.3 pm.

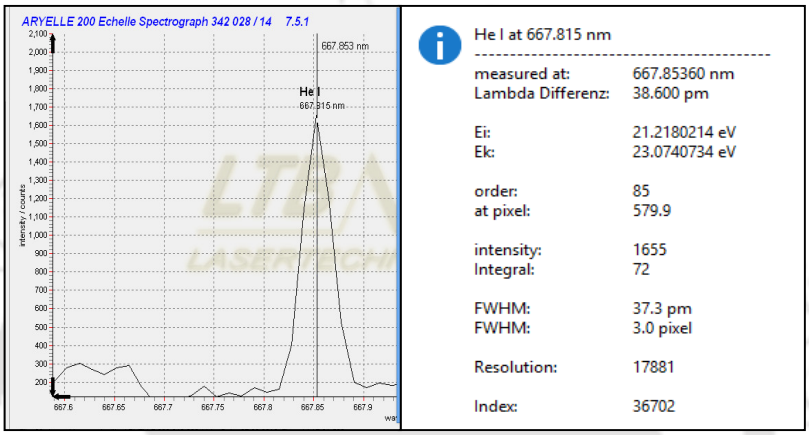

Fig. 3.7: Spectrograph of 667.8 nm He lines with FWHM

Table 3.2 shows the electron density at 16 various positions of the plasma chamber calculated from Eq. (2) for the 667 nm wavelength of the He transition. The Full-width half maximum is 37.3 pm for 667 nm, as shown in Fig. 3.7. It suggests that electron density distribution is uniform throughout the chamber. The electron density variation is less than 5% (minimum 2.94×10^{11} to maximum 2.98×10^{11}), offering more than 90% uniformity throughout the hemispherical shell. The average electron density is calculated as 2.96×10^{11}, which matches closely with the simulated electron number density of 0.82×10^{11} to 3.4×10^{11} for different configurations. Hence, Comsol® simulation results are successfully validated by experimental results.

Table 3.3: Electron number density calculated at 667 nm of He transition for different positions of the plasma chamber during plasma processing

Electron density, n_e $\times10^{11}$ (/m^2)	P1	P2	P3	P4	P5	P6	P7	P8
	2.95	2.98	2.97	2.97	2.95	2.98	2.97	2.96
	P9	P10	P11	P12	P13	P14	P15	P16
	2.94	2.98	2.97	2.96	2.94	2.98	2.97	2.96

3.4 Summary

- The Comsol® simulation study was carried out to optimize plasma chamber configuration. The custom-made chamber with a V-shaped groove has shown uniform reactive radical distribution for polishing free-form optics.
- The simulation was validated by experimental analysis of the entire chamber's plasma temperature and electron density using an optical emission spectrometer.

Chapter 4

In-situ and accurate monitoring of plasma polishing process

4.1 Introduction

Plasma processing is a complex phenomenon, and MRR depends on factors like power, time of operation, chamber condition, pressure, flow rate, etc. Any fabrication process optimized by knowing MRR. MRR can be obtained by analyzing the processed end product, but it is time-consuming, and real-time controlling is impossible. Sometimes it may not be possible to achieve the desired end product. Real-time Material removal rate analysis is essential for monitoring and controlling the process. Non-Invasive real-time monitoring is preferable.

Several ways establish the relationship between the material and volumetric removal rates. U. S. Pat. No.6, 068,783 (Steven Lee Szetsen, Hsinchu, 2000) discloses a method where plasma gas such as CO was used for monitoring the chamber condition. U.S. Pat. No. 5,877,032 (Guinn, Keith V., 1999) discloses a method where etch rate analysis was conducted using OES by monitoring the ratio of spectral intensities between the by-product of plasma and substrate interaction and reactive gas intensity. U.S. Pat. No. 8,747,686B2 (Bo Zheng, Saratoga, CA (US); Mei Chang, Saratoga, CA (US); Arvind Sundarrajan, San Jose, 2014) describes that the endpoint of the substrate fabrication was detected by analysis of the by-product of the plasma using OES in a separate housing in the processing chamber. In this invention, an optical emission spectrometer is used for real-time analysis.

The above methods utilize OES for monitoring the end product of the plasma interaction or concentration of plasma gas during etching. The by-product and reactive gas concentration during etching depend on the plasma interaction and the flow rate of the gases. Hence, these methods must provide an absolute and accurate determination of the material removal rate for the plasma polishing process described in the present invention.

In the present study, the material removal rate has been monitored using different ionizing species generated in the plasma during plasma polishing. Specifically, work includes monitoring silicon oxidation states generated in situ during plasma interaction with the substrate. These silicon oxidation states are treated as in situ probe gases for monitoring the plasma interaction with the substrate during processing time.

Advantages of the using silicone oxidation states

- Silicon oxidation states provide accurate plasma and substrate interaction predictions.
- Silicon oxidation states act as in-situ probe gases for MRR prediction.
- This is substrate-specific, independent of processing and reactive gases.
- Silicone oxidation states that relative intensity doesn't depend on the operation's flow rate, pressure, and power.

4.2 Experimental setup

Figure 4.1 shows the typical block diagram of the experimental setup. OES is a monitoring system separating plasma emission light into component wavelengths and their intensity. One example of an OES system has an Andore CCD array detector with Echelle grating coupled to a spectrograph. This system is sensitive to about 400 nm to about 950 nm emissions, has a resolution of less than 70 pm, and has Scan times of less than 1 second. RF generator of 40.68 MHz was used for the generation of plasma. A gas source provides a constant flow of gas to the plasma chamber as per the section 2.5.1.

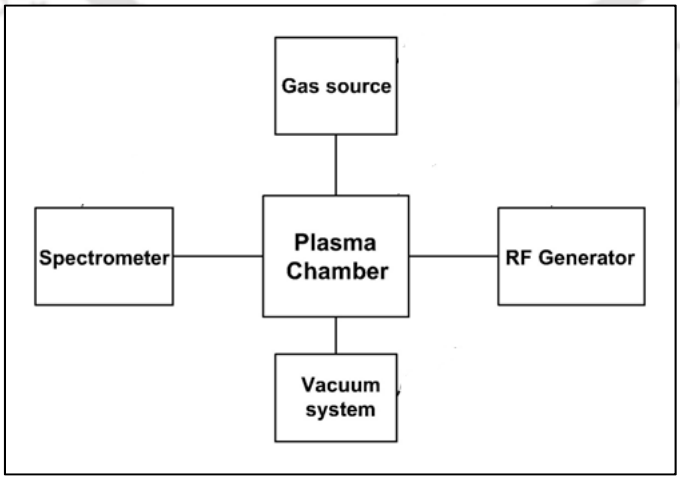

Fig. 4.1: Schematic block diagram of the experimental setup

The substrate thickness and weight were analyzed before plasma processing. A standard technological process appropriately cleaned the substrate before plasma polishing. The substrate was kept in a plasma chamber pre-cleaned by He and O_2 plasma. The plasma chamber was evacuated to 1×10^{-5} mTorr using a vacuum system to eliminate moisture and any other foreign gaseous impurities. A RF generator initiated plasma discharge in the section through capacitively coupled electrodes placed outside the chamber to eliminate plasma contamination. The light emitted from the plasma was collected by a lens and directed to a spectrometer through an optical fiber. The computer plotted the signal of the emitted light as wavelength versus intensity.

The experimental procedure includes:

- Selection of suitable spectral signals of silicon atoms as a probe for monitoring material removal rate.
- Measuring spectral intensities of the selected lines.
- Calculation of average ratio of selected spectral lines intensities over a while.
- Providing correlation between the average ratio of spectral intensities as well as average volumetric material removal rate/weight reduction;
- Prediction of weight reduction /average volumetric material removal rate over a while using the average ratio of spectral intensities; and
- Prediction of time required for a given material removal with the help of average spectral ratio.

4.3 Results and discussion

The emission spectrum of Si III at 481.97 nm, as illustrated in Fig. 4.2 (a), is a comparatively stable metastable state (marked as*) and has a relative intensity of 5264 with a transition probability of 1.256×10^{9} /s. Hence, the signal is susceptible to analysis. Similarly, Si II at 518.55 nm is also a reliable metastable oxidation state with transition probability 1.036E+08/s, as shown in Fig. 4.2 (b). The signal-to-noise ratio for these signals is also very high compared to other transitions. Hence, signs are always present during plasma processing. The intensity of the above-said signals was monitored during plasma processing using optical emission spectroscopy (OES). The intensity ratio was calculated for every second during the entire period of operation. The average ratio for the specified process period correlated with the calibration plot for quantifying the material removal and volumetric removal rates.

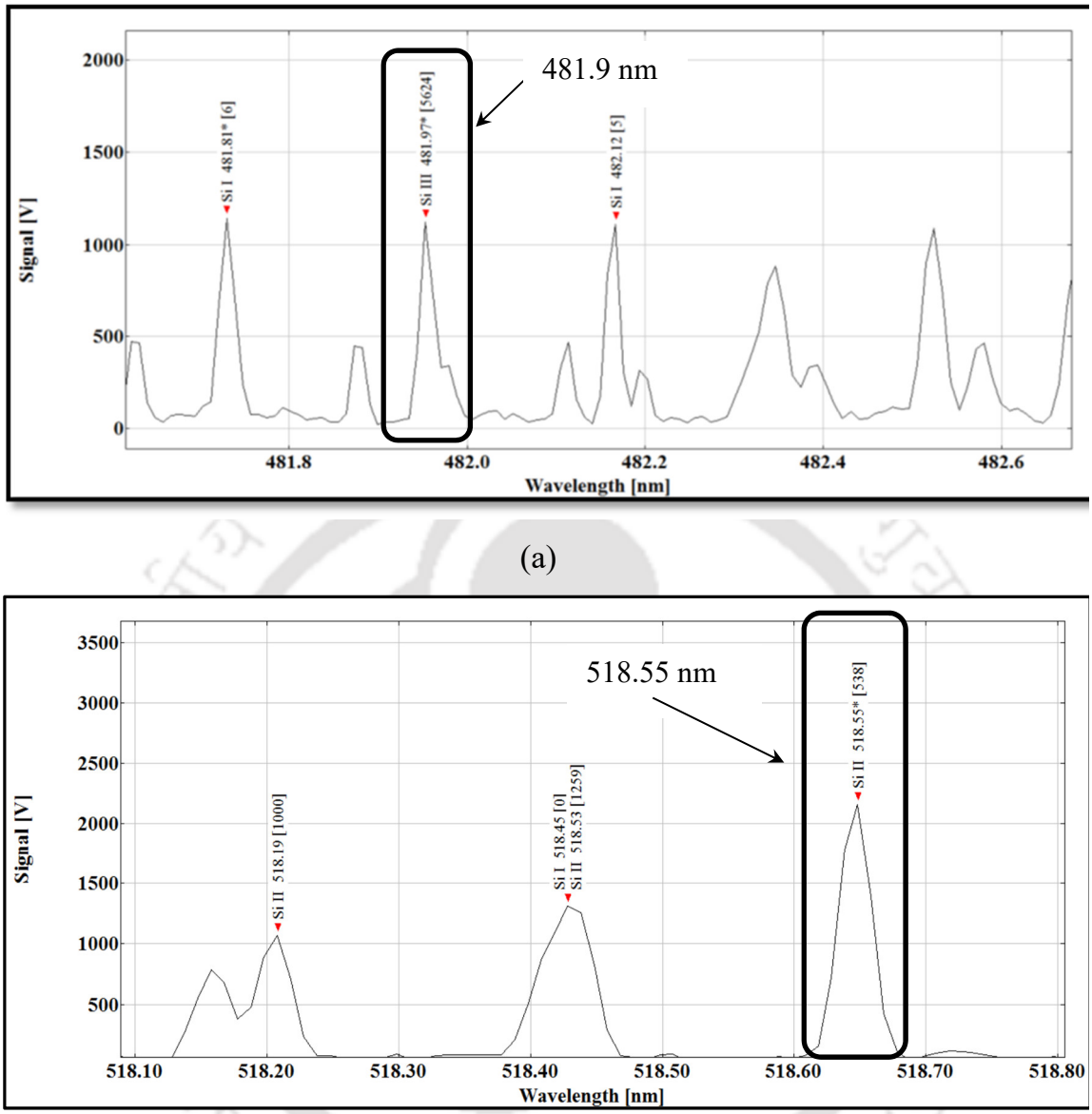

Fig. 4.2: Emission spectrum (a) near 482 nm for Si III transition and (b) near 518 nm for Si II transition

The plasma chamber is filled with gases SF_6, O_2, and He at a specific ratio and particular pressure by gas supply source for generating calibration plot. The calibration curve for monitoring plasma processing was obtained by processing the substrate at various periods and different Si II to Si III intensity ratios. The material removal or weight reduction was plotted for other Si II to Si III oxidation states' intensity ratios as described in Fig. 4.3. The experiment was repeated multiple times to minimize errors and complete calibration satisfactorily. A linear relationship between weight reduction at the end of the process and the calculated average ratio was obtained. This is graphically illustrated in Fig. 4.3. The

calibration plot's regression coefficient (R^2) was 0.97, suggesting the study's repeatability. For validation of the calibration plot, plasma processing was carried out for 40 mins continuously, and the process was repeated multiple times. According to the calibration plot, the predicted weight reduction was compared with the actual weight reduction concerning relative intensity ratios of SI II and Si III, as shown in Fig. 4.4. It was observed that the predicted value closely matched the actual weight reduction value. Maximum error amount to be 5% compared to substantial weight reduction. The generated calibration plot can be used for real-time monitoring during the plasma processing of fused silica.

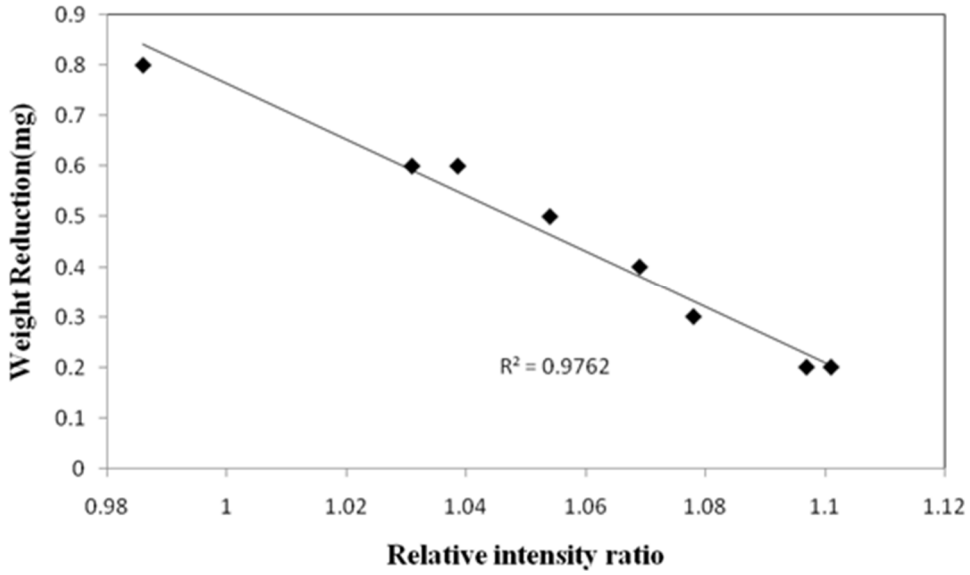

Fig. 4.3: Relationship between the relative intensity ratio Vs. weight reduction

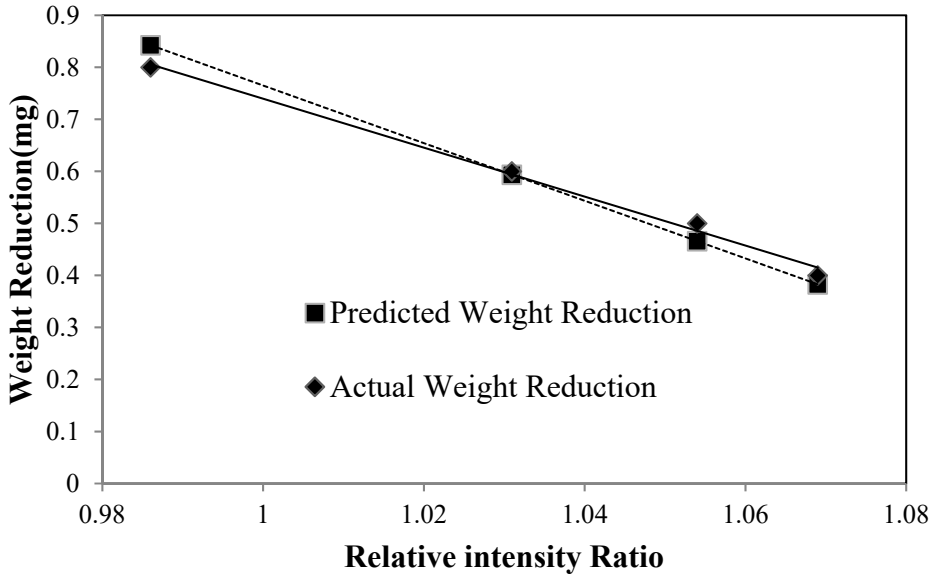

Fig. 4.4: Validation of calibration plot by comparing predicted weight reduction Vs. actual weight reduction

The calibration plot illustrated in Fig. 4.3 shows that the weight reduction of fused silica substrate was inversely proportional to Si II and Si III intensity ratios. Weight reduction of 0.15 mg to 0.85 mg was observed, while the intensity ratio of Si II to Si III varied from 1.11 to 0.95. The plasma process demands continuous operation for a more extended period. Therefore, process drift is unavoidable for a long time of operation. The volumetric material removal rate for plasma also depends on the time of plasma processing and machining conditions related to the duration of the procedure. Process drift also influences real-time monitoring. Hence, optimizing the operation time and understanding the calibration plot's validity is essential.

Figure 4.5 (a) illustrates the plasma processing for 20 minutes of continuous operation. As per the procedure, the plasma chamber was filled with optimized gas from the gas source, and an RF generator initiated plasma through copper electrodes. The light emitted from the plasma was monitored continuously using OES. The intensity ratio of Si II and Si III at specified wavelengths was calculated for each second for 20 minutes of operation, and an average change in ratio was noted. Weight reduction and change in thickness before and after 20 minutes of plasma processing were analyzed gravimateric method. Weight reduction with ratio was plotted in the primary axis, and volumetric material removal rate was plotted in the secondary axis, as shown in Fig. 4.5. This procedure is repeated multiple times to minimize the error and to study the repeatability of the experiment. The various experiments at 20 minutes of operation provide a regression coefficient (R^2) of 0.94, indicating the repeatability of the experiments.

Similarly, Fig. 4.5 (b) illustrates the plasma processing for 40 minutes of continuous operation. As per the procedure above, one-second data for 40 minutes has been complied with. The average intensity ratio correlation with material removal rate and volumetric material removal rate was plotted in Fig. 4.5 (b). Multiple experimental results were also plotted. A regression factor (R^2) of 0.99 was obtained, which validates the calibration plot and helps in monitoring the material removal rate and volumetric material removal rate. 40 mins of operation show better repeatability (R^2 factor 0.99) and percentage of error 1% than 20 mins of operation (R^2 factor 0.94, error 6%) since the initial substrate condition, such as moisture, may hamper the repeatability of 20 mins of operation slightly. For 60 minutes of continuous operation, as shown in Fig. 4.5 (c), the regression factor (R^2) for multiple operations was 0.9 (error 10%). The slight reduction in the R^2 factor compared to other causes may be due to the deposition of contamination due to prolonged operation, which may give erroneous results.

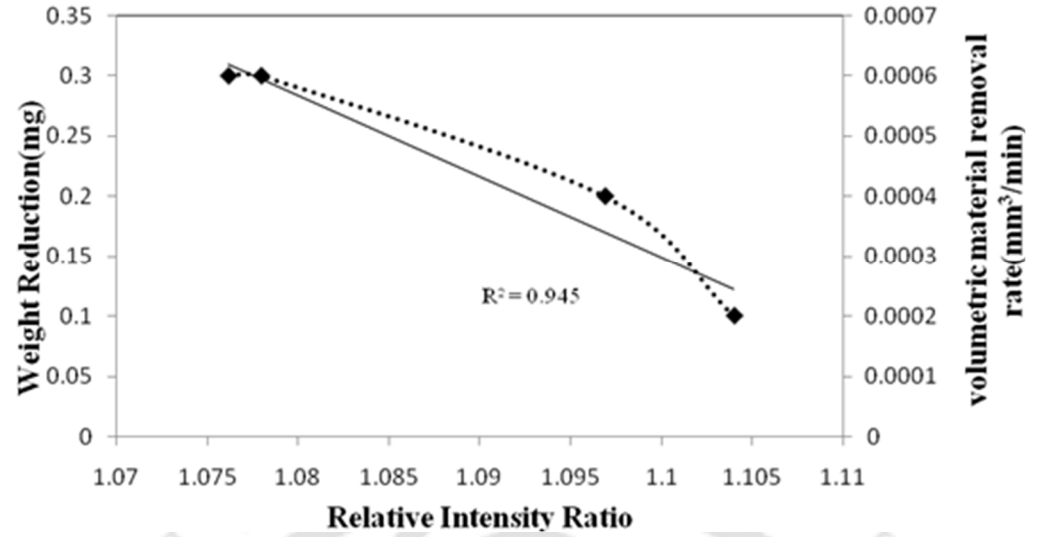

(a)

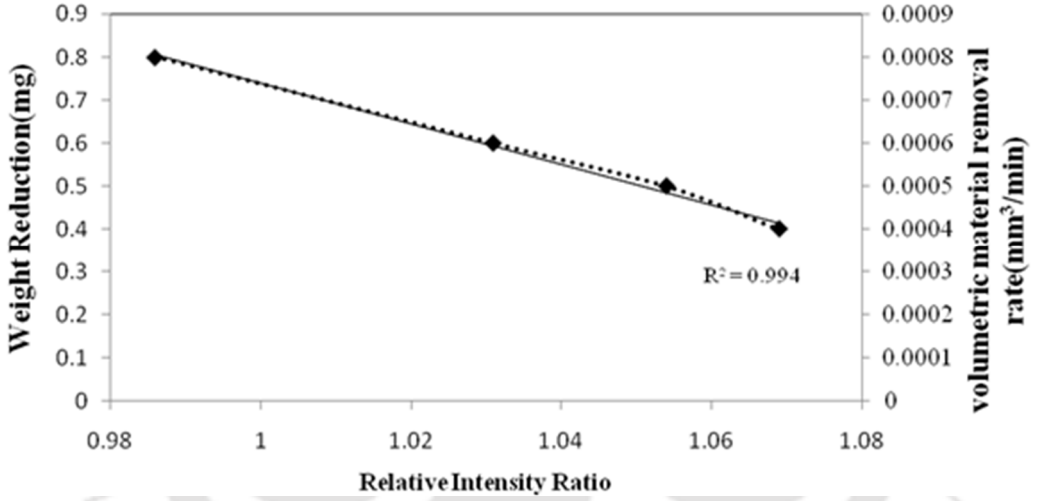

(b)

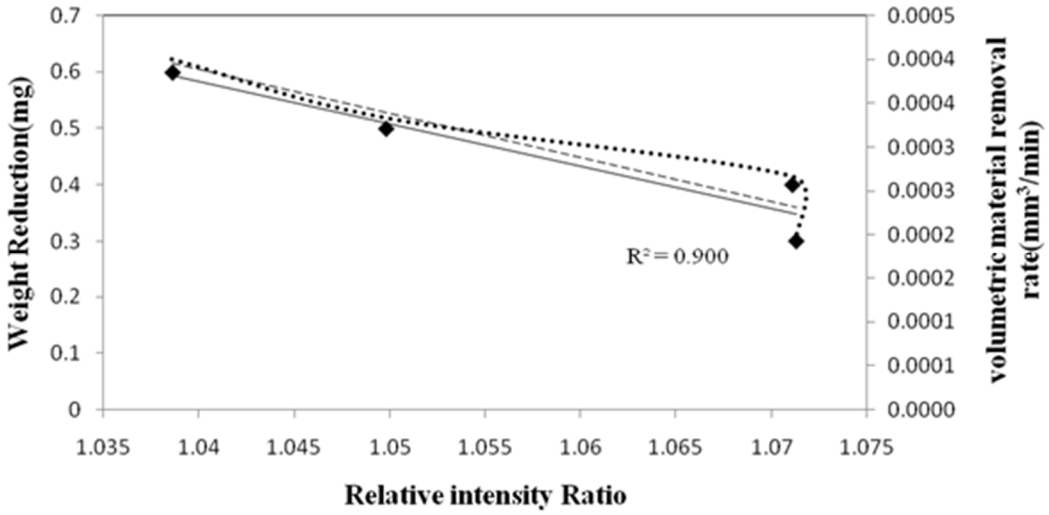

(c)

Fig. 4.5: MRR prediction for continuous operation of (a) 20, (b) 40, and (c) 60 mins

These results suggest that the invented process can be employed for real-time monitoring of a long operation time, such as 60 mins. Results indicate that if the duration of continuous operation is 40 mins, then the prediction error will be minimum.

4.4 Summary

Optical emission spectroscopy was used effectively for in-situ material removal rate prediction of fused silica substrate during plasma polishing. The 40 mins of continuous operation closely match the predicted MRR.

Chapter 5

Quantifying damage depth of fused silica substrate

5.1 Introduction

Especially for brittle substrates like fused silica materials, the knowledge of machine-induced mechanical stress is essential for the performance and yield of the devices. In Hemispherical resonator gyro (HRG), which works in the principle of Coriolis force, the quality factor Q (defined as the ratio of the amount of energy stored divided by energy lost at every cycle) is a very critical parameter for the performance of gyro. As shown in Fig 5.1, it depends on many factors, such as design, precise manufacturing, material selection, unique processing, and packing. With a well-defined design and given material, the Q factor predominately depends on precise manufacturing. Shell manufacturing without distortion of the chemical network is vital for the resonator's performance. Hence, the

Quality factor (Q) is proportional to the surface chemistry and molecular network. The contact nature of machining induces surface and subsurface defects in the brittle fused silica substrate. Hence, it is a prerequisite to quantify the depth of damage to the device. Quantifying the damage depth helps increase the production rate, improve performance, and achieve cost-effective manufacturing.

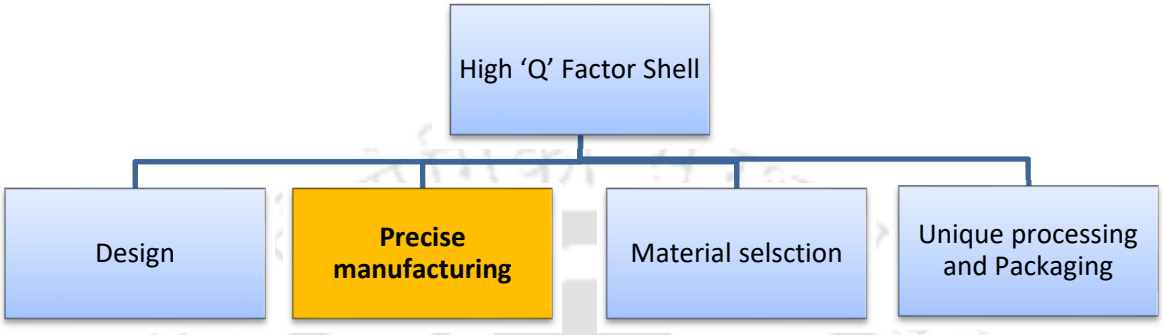

Fig. 5.1: Q factor-dependent parameters

Various methods are being under development stages, such as X-ray micro-diffraction (Tamura et al., 2003), electron-induced Kossel diffraction with a scanning electron microscope (SEM) (Bauch et al., 1999), and convergent beam electron diffraction with a transmission electron microscope (TEM) (Nucci et al., 2005) for analyzing the stress by knowing the elastic strain in a crystalline material. These diffraction methods provide direct information about the lattice parameters of crystalline materials. Hence, these methods need crystal periodicity, like metals. Raman spectroscopy is the only reliable method to analyze the local mechanical stress in the micrometer depth scale. Raman spectroscopy relies on the polarizability of the molecules upon exposure to photon energy. Hence, it limits materials like polymers, glasses, ceramics, and semiconductors.

5.2 Introduction to Raman spectroscopy

Raman spectroscopy depends on the inelastic scattering of incident light. The distribution is different from the absorption, which is the functional parameter of the most spectrometer. In diffusion, unlike absorption, there is no excitation of electrons from the ground state to the excited state due to additional energy. All states of the molecule undergo specific changes in the scattering process, and all states are mixed to form a distorted energy state called virtual. The energy of this state depends on the incident Laser energy, and the amount of distortion depends on the electronic environment of the molecule. These distorted states

are much shorter-lived compared to absorption states. There are two types of scattering processes that exist. The elastic scattering is most intense, involving the electron cloud without nuclear movement. Hence, there is no appreciable change in energy, and it is called Rayleigh scattering. On the other hand, Raman scattering is inelastic, with heavier nuclei movement, thus changing a considerable amount of energy during this process. This change can be lower than the incident energy, called Stokes scattering originates from the ground state. On the other hand, the vibrationally excited molecule can have a higher frequency than the incident Laser is called anti-stock scattering.

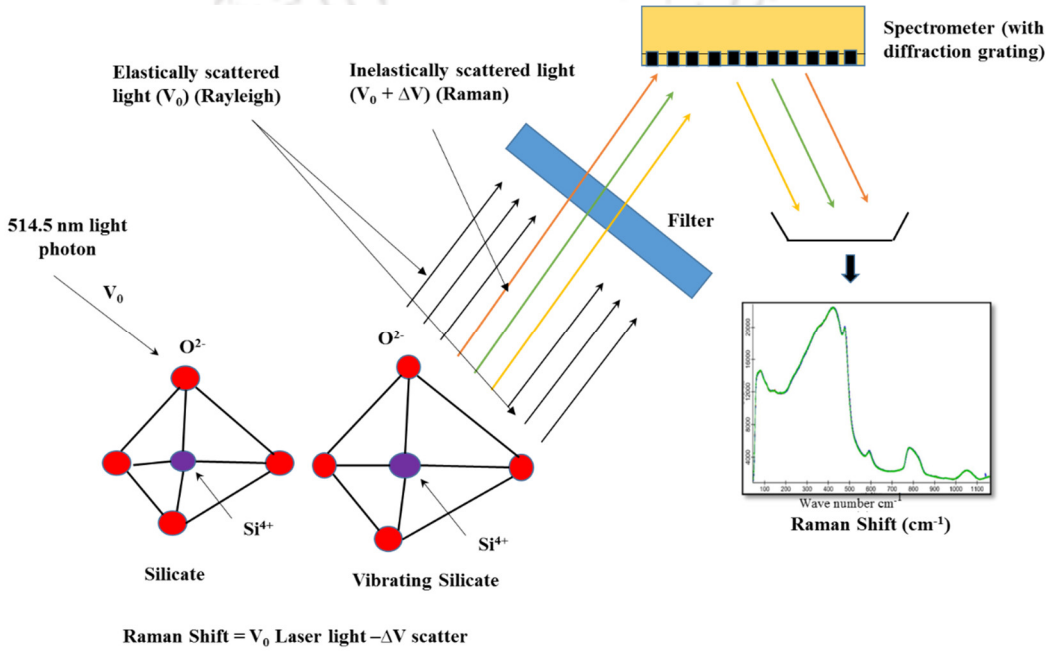

Fig. 5.2: Schematic of basic instrumentation of Raman spectroscopy (Avadhesh Kumar Yadav, 2012)

5.3 Instrumentation of confocal Raman microscopy

Raman spectroscopy is a weak scattering technique in which one in a million excited photons give gives to inelastic scattering. Moreover, this is a non-resonant interaction of light with the molecule. In contrast, fluorescence is a resonance phenomenon. Hence, it is essential to reduce the fluorescence background. This can be possible by selecting the appropriate Laser excitation for a specific substrate or reducing the detection volume. However, a change in excitation frequency with the substrate is not feasible; hence, a confocal setup limits detecting the fluorescence light emitting from the same focal plane. Confocal is defined as having the same focus where the illuminating source and pinhole

are positioned in the same focal plane in front of the detector. Raman microscope system works with the help of a laser source, a microscope objective, and a spectrometer with a CCD detector.

5.3.1 Excitation laser source

The intensity of Raman scattering is proportional to υ of the laser source. υ is the frequency of the laser source. On the other hand, high frequency leads to strong fluorescence. Hence, the typical laser source should have the following properties;

- It should have a single Gaussian beam with TEM00 mode for focusing on the minor spot.
- The light should be linearly polarized to analyze polarized dependent samples also.
- The FWHM should be narrow to achieve a reasonable resolution of about 1 cm-1.
- The frequency should be very stable (variation <0.01 cm^{-1}) for very accurate stress analysis.
- The intensity should be stable (<1–2% power fluctuations) for accurate concentration analysis.

5.3.2 Microscope objective

A microscope objective with a high numerical aperture (NA) is preferred over the lens for Raman application. Higher NA provides better spatial resolution along with collection efficiency.

5.3.3 Spectrometer with grating

The spectrometer should have the capability to work from U V to IR. The grating generally disperses the signal to the spectrometer depending upon the incident wavelength. The dispersion characteristics rely on the grove density (number of grooves per mm).

5.3.4 CCD detector

The detector is one of the most critical components for Raman application. The CCD with a higher quantum efficiency (QE) is preferable for detecting the weak incoming signals of the Raman spectrometer. Furthermore, the back-thinned CCD with an excellent cooling system suits a Raman spectrometer with good sensitivity.

5.4 Specification of Raman microscope

TECHNOS STR-250 system with 532 nm Nd-Yag laser of 100 mW output power, equipped with 2400 and 600 g/mm gratings, has a 0.2 cm^{-1} spectral resolution in the 50-5000 cm^{-1}. As shown in Fig. 5.3, the Raman spectrum provides the quantum of information regarding material science and chemistry. Widely used to provide information on:

- Chemical structures and physical forms,
- Identifying substances from the characteristic spectral patterns ('fingerprinting'),
- To determine quantitatively or semi-quantitatively the amount of a substance in a sample.
- This instrument can be used for any critical substrates due to its non-contact nature and free from specific sample preparation.

5.5 Application of Raman microscopy

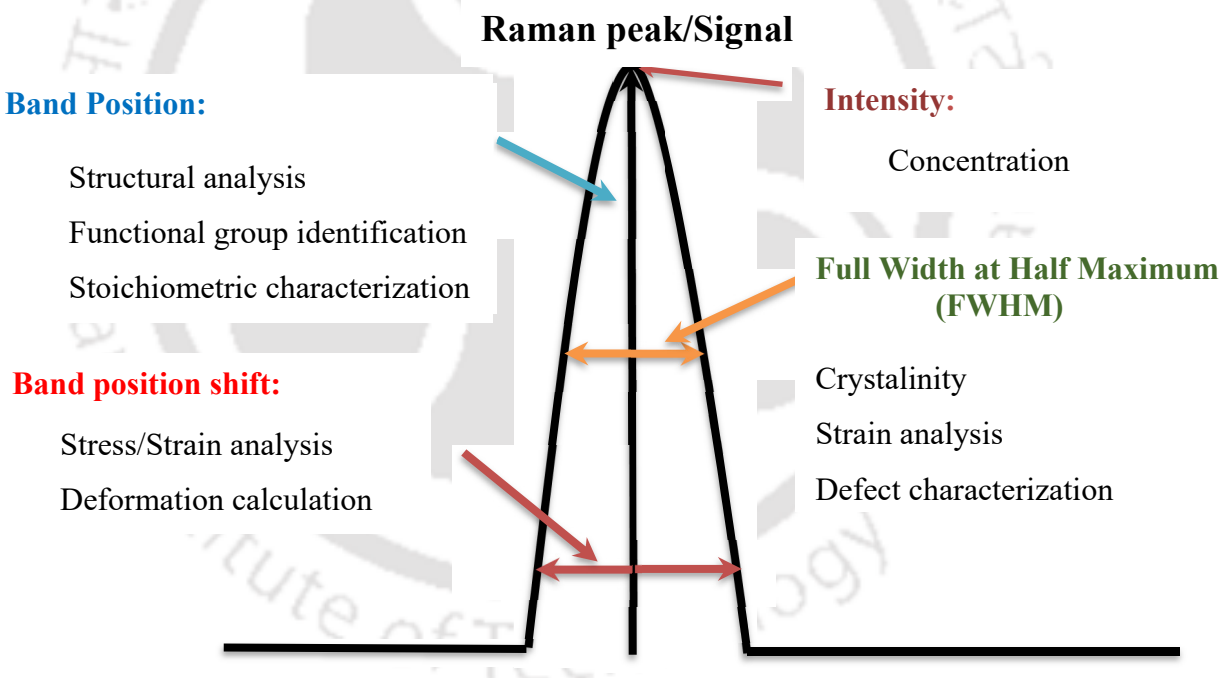

Fig. 5.3: Typical schematic of Raman signal and its functions

5.6 Basic application for material processing and manufacturing

Identification of molecular change before and after the fabrication/manufacturing process, which includes:

- Understanding the difference in characteristic frequency of the molecular network.

- To understand mechanical densification during machining.
- Analysis of machine-induced molecular defects.
- Optimization of machining parameters and quantify the damaged layers.
- Quantification of damaged layer removal after the subsequent process.

5.7 Raman spectrum of fused silica material

Tetrahedron six-membered Si-O-network of fused silica vibrates in incident light at 440 cm^{-1} due to bond rocking vibration, where the oxygen atom moves perpendicular to the Si–O–Si plane. The peak at 800 cm^{-1} is attributed to the bending vibration of Si-O-Si. At the same time, peak at 1064 cm^{-1} and 1200 cm^{-1} corresponds to Si-O asymmetric stretching.

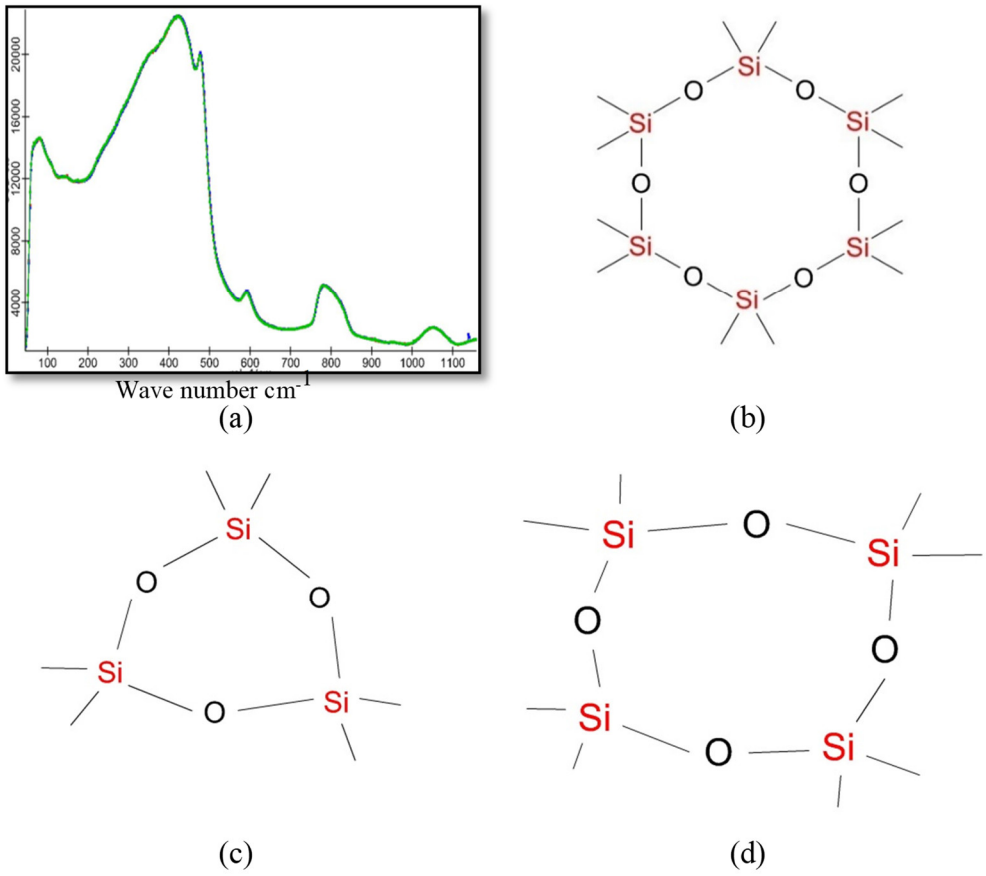

Fig. 5.4: (a) Typical Raman spectrum of fused silica, the schematic shape of (b) six-membered ring, (c) defective (D2) three-membered ring, and (d) defective (D1) four-membered ring

But due to stress or deformation, the ideal relaxed six-membered Si-O-Si- ring converted to strained four and three-membered structures, as shown in Fig. 5.4. These

strained rings vibrate at 490 cm^{-1} (four-membered (D1)) and 600 cm^{-1} (three-membered (D2)); hence these

are denoted as D1 and D2 peaks, respectively (Galeener and Geissberger, 1983). Therefore, a detailed interpretation of the Raman signal provides insight into surface stresses induced by mechanical machining (Liu et al., 1997) .

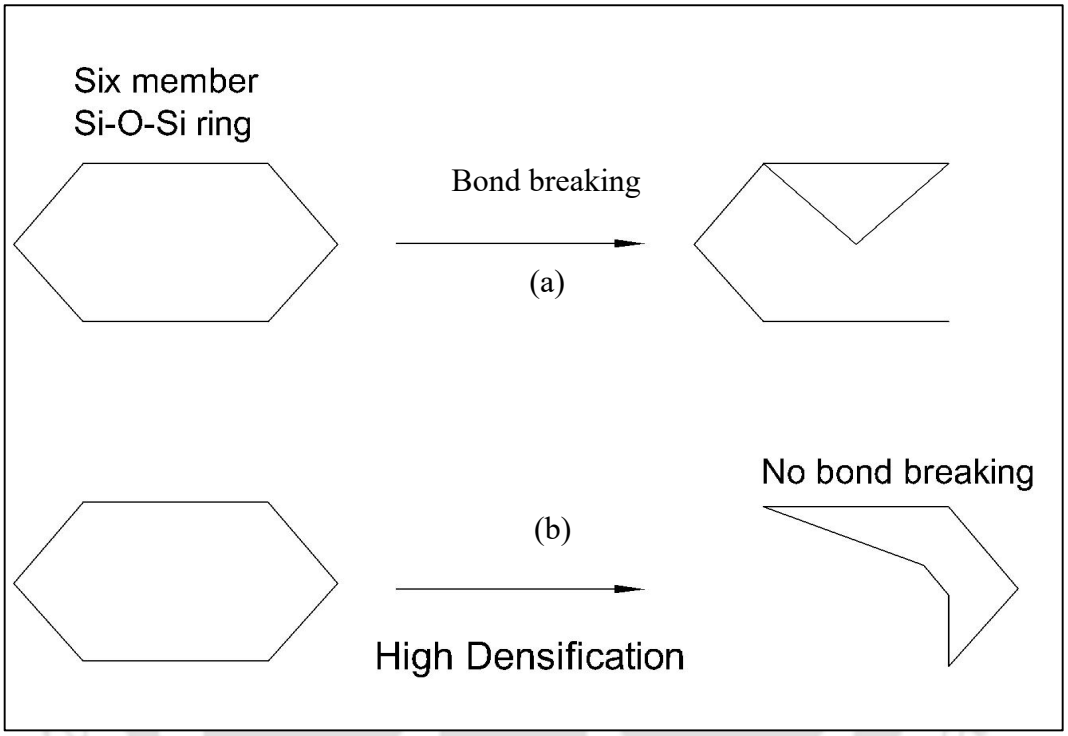

Fig. 5.5: Schematic of fused silica chemical structural change (a) bond breaking and (b) no bond breaking (high densification)

While there is stress on the fused silica, the six-member molecular network may break and be converted into fewer members. Suppose the pressure is not enough to break the six-member ring. In that case, it may deform it and result in high-densification molecular layers, as shown in Fig. 5.5. Machining can induce mechanical damage where bond-breaking predominates, and structural damage leads to densification.

Tables 5.1 and 5.2 show the detailed Raman observation and the interpretation for distinguishing mechanical damage from structural damage. These studies confirm that Raman microscopy is one of the most powerful techniques for analyzing the chemical network distortion of fused silica. Hence, this method optimizes fused silica's rotary ultrasonic machining parameters and quantifies damage depth after the jig grinding process.

Table 5.1: Analysis of mechanical damage

Description	Observation in Raman spectrum	interpretation
Conversion of 6 members to 4 and 3-member rings	Shift in Raman peak (490 and 600 cm^{-1}) towards high frequency and increase area under the peak.	Increase in concentration and energy of defect peaks
	Shift in 440 cm^{-1} peaks towards low frequency and decrease in area under the peak.	Decrease in density and frequency of 6-member peaks.
	The appearance of peaks at 1100 to 1050, 1000-950, 900, and 850 cm^{-1} for di-, meta, pyro, and orthosilicate, respectively	Formation of di-silicate, metasilicate, borosilicate, and orthosilicate vibrational peaks.

Table 5.2 Analysis of structural damage

Description	Observation in Raman spectrum	interpretation
The deformation of 6 member ring is known as mechanical densification.	The appearance of sharp peaks instead of broad peak	The center of the wide six members 440 cm^{-1} peak induced multiple sharp peaks. **FWHM of these peaks is proportional** to stress concentration.
	The overall broadness of the six-member peak increases	FWHM of 440 cm^{-1} peak increases due to the deformation of the 6-member ring.

5.8 Optimization of ultrasonic machining parameters

Among the various methods, Rotary Ultra Sonic machining (RUM) is best suitable for shaping advanced brittle materials like Fused silica (Jiao et al., 2005). It is a hybrid machining that utilizes both grinding and conventional ultrasonic machining. It is effectively used for machining brittle and difficult-to-machine advanced materials like ceramics, fused silica glasses, etc. Generally, the material removal mechanism for the RUM process originates as a brittle fracture or chipping of the substrate. But, the material removal rate can follow the plastic deformation with optimized parameters (Zhou et al., 2016).

However, the RUM induces surface and sub-surface damage to the brittle fused silica substrate (Hed and Edwards, 1987). Especially for brittle workpieces like fused silica, optimizing the machining parameters is essential based on subsurface damage induced by machining. Various destructive and non-destructive methods did SSD assessments. In the case of the destructive processes, SSD can be measured by microscopic methods after removing each layer by magnetic rheological polishing or by HF etching ((Suratwala et al., 2006), (Neauport et al., 2009a), (Randi et al., 2005)). These destructive methods are very accurate but need a complementary way to access SSD, and these methods are cumbersome and cannot be adopted for all the samples. On the other hand, non-destructive methods like confocal fluorescence microscopy (Neauport et al., 2009b) and light scattering methods (Trost et al., 2013) are used for accessing the SSD. But these are complicated methods that cannot be suitable for industrial application. Blaineau et al. (Blaineau et al., 2013) studied the quick accessing of SSD concerning the surface roughness developed during different grinding processes. This study also established the relationship between surface roughness with subsurface defects of the precision ground surfaces. The Abbott-Firestone curve has shown a better fit for the fused silica substrates. The Confocal Raman microscopy was used for accessing the SSD and optimizing the RUM parameters such as feed rate, spindle speed and depth of cut, etc. The non-destructive confocal capability of Raman microscopy was aptly used for depth analysis of fused silica substrate after and before machining.

5.9 Experimental methodology

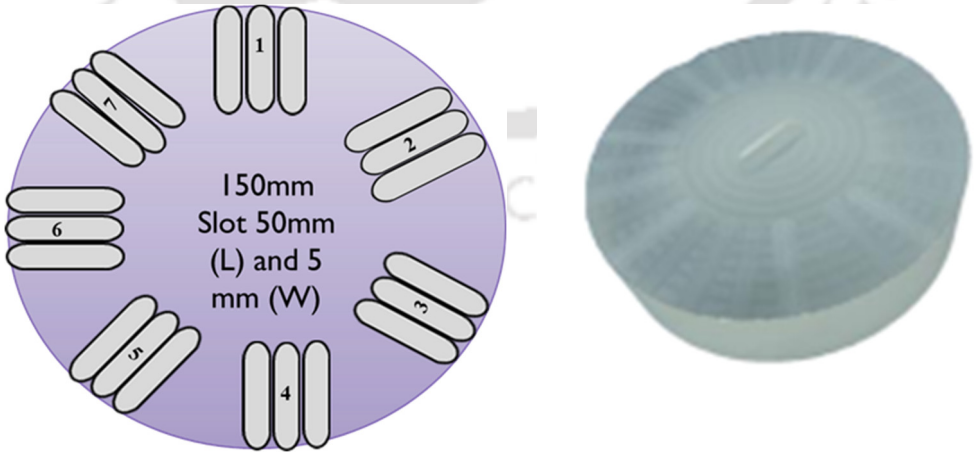

(a) (b)

Fig. 5.6: (a) Schematic of ultrasonic machined substrate, (b) actual substrate

The RUM machine with 25 kHz ultrasonic frequency and linear axis resolution of 0.1µm. The disc sample of 150 mm diameter is used for the experiment. Various slots about 50 mm long and 5 mm wide in this disc were made using different RUM parameters, as shown in Fig. 5.6. Minimum of three slots were realized with the same parameter for analysis. Raman spectrum was obtained before machining the substrate, and subsequently, Raman analysis was conducted after machining. The cutting tool has diameter of 3 mm and grit size of 1.6 mm.

Table 5.3: Ultrasonic Machining Parameters

Slot No.	Cutting speed (m/min)	Feed rate (mm/min)	Depth of cut (µm)
Slot 1	25	100	5
Slot 2	5	300	25
Slot 3	5	100	5
Slot 4	5	100	25
Slot 5	25	300	25
Slot 6	25	100	25
Slot 7	25	300	5
Comparison of slots with parameters	Slot 1 and Slot 3	Slot 5 and Slot 6	Slot 1 and Slot 6
	Slot 2 and Slot 5	Slot 1 and Slot 7	Slot 3 and Slot 4
	Slot 4 and Slot 6	Slot 2 and Slot 4	Slot 5 and Slot 7

5.10 Raman spectroscopy analysis

After machining, samples were cleaned under an ultrasonic bath with acetone before analyzing under a Raman microscope. The Raman spectrum was taken at the surface and the depth with 2-micron steps till 20 microns for accessing the SSD for transparent samples higher than the 20 microns can be accessed. Three points were captured from each slot, and the average was compared with other places. Machining can induce the following distortion at the molecular network.

- During RUM machining, abrasive indentation load can cause breakage of chemical bonds, which induces chemical defects at the fused silica ring network, as shown in Fig. 5.5 (a). This mechanism of removal is called chipping mode. This is mainly concentrated at the surface (Lv et al., 2016). This can be assessed by Raman

microscopy by analyzing the area ratio of the area under the curve of a six-membered ring with defect peaks (three or four-membered).

- If the indented force is not enough can cause deformation in the silica network. It can extend deeper than the cracks. This deformation can induce distortion to the silica network. This distortion result in the densification of the silica layer can form local crystallites. This can be analyzed by understanding the change in FWHM of six-membered rings by Raman microscope.

5.10.1 Raman microscopy results with the variation of cutting speed

Figure 5.7 shows that the six-membered ring concentration is higher than defect peaks for the substrate machined at 25 m/min cutting speed (C) than the 5 m/min cutting speed keeping other parameters the same. The same trend was observed with the depth of the sample. It suggests that with an increase in cutting speed, the load exerted by the tool reduces; hence, the formation of chemical defects also reduces with an increase in cutting speed. Similarly, Fig. 5.8 shows that the full-width half maximum (FWHM) for six-membered rings increases with the cutting speed (c). The FWHM increases with depth also. An increase in FWHM with cutting speed indicates a reduction in deformation due increase in cutting speed.

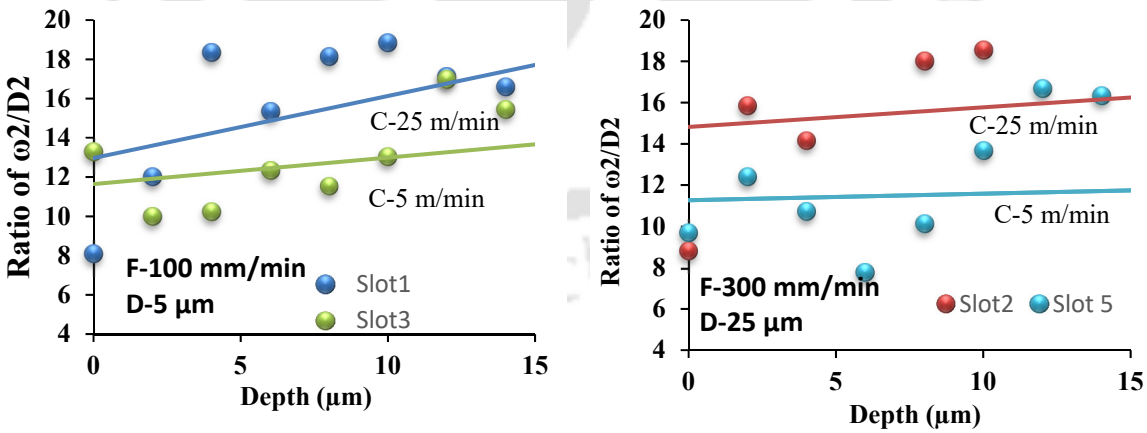

(a) (b)

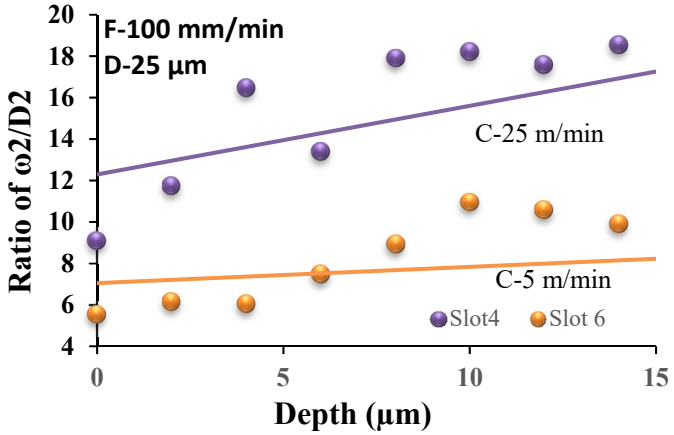

(c)

Fig. 5.7: Ratio of the area under the six-membered ring (800 cm-1) to three-membered (600 cm-1) ring with the depth of the machined substrate while changing the cutting speed at (a) feed rate 100 mm/min and depth of cut 5 µm, (b) feed rate 300 mm/min and depth of cut 25 µm, and (c) feed rate 100 mm/min and depth of cut 25 µm

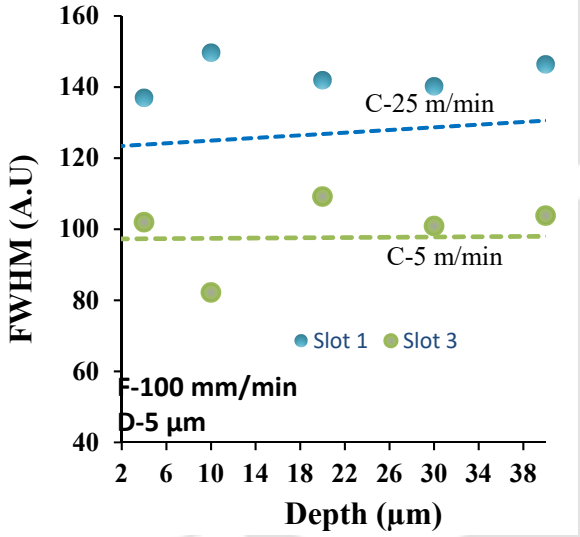

(a)

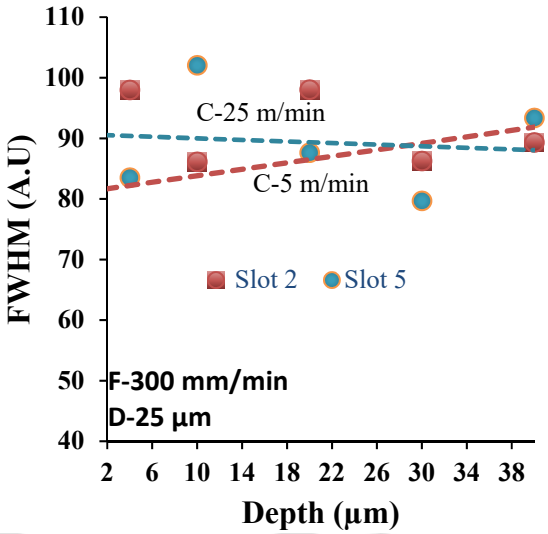

(b)

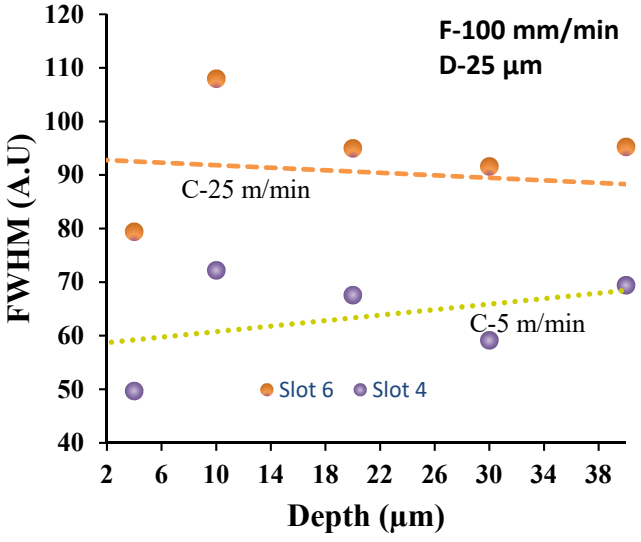

(c)

Fig. 5.8: FWHM of six-membered ring depth of the machined substrate while changing cutting speed at (a) feed rate 100 mm/min and depth of cut 5 µm, (b) feed rate 300 mm/min and depth of cut 25 µm, and (c) feed rate 100 mm/min and depth of cut 25 µm

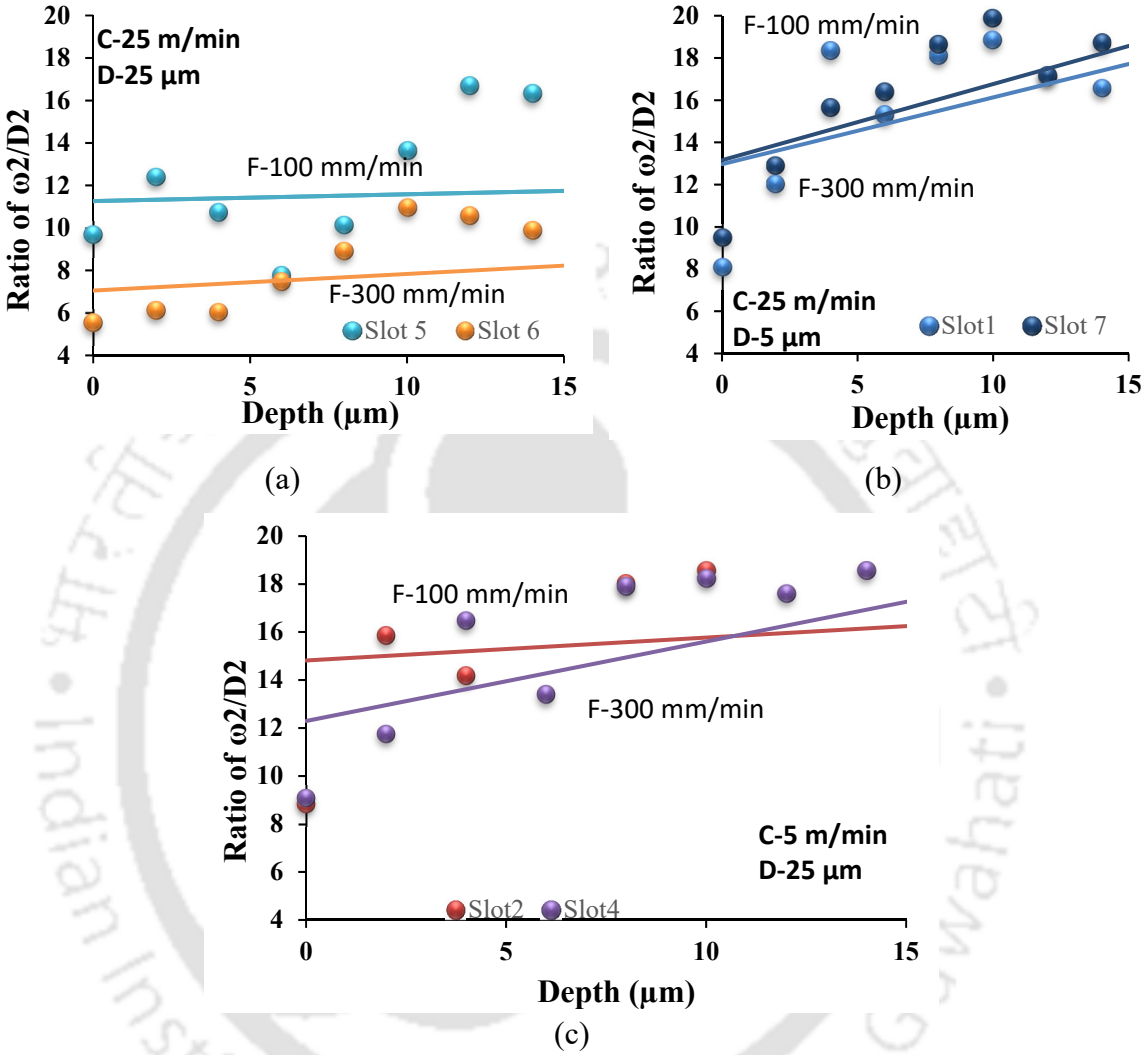

Fig. 5.9: Ratio of the area under the six-membered ring (800 cm-1) to three-membered (600 cm-1) ring from with depth of the machined substrate while changing feed rate at (a) cutting speed 25 m/min and depth of cut 25 µm, (b) cutting speed 25 m/min and depth of cut 5 µm, and (c) cutting speed 5 m/min and depth of cut 25 µm

5.10.2 Raman microscopy results with a different feed rate

Figure 5.9 shows that with an increase in feed rate (F) from 100 mm/min to 300 mm/min, the surface integrity is also reduced, such as chemical defect concentration increases. The increase in feed rate induces more load at the substrate surface; due to the increase in load, the chemical defects were formed more during machining, where the feed rate is high.

Figure 5.10 shows that the FWHM is less for the slot with a higher machining feed rate. Hence, a decrease in FWHM and an increase in chemical defect correlates to the rise in subsurface damage of the fused silica substrate with the increase in feed rate.

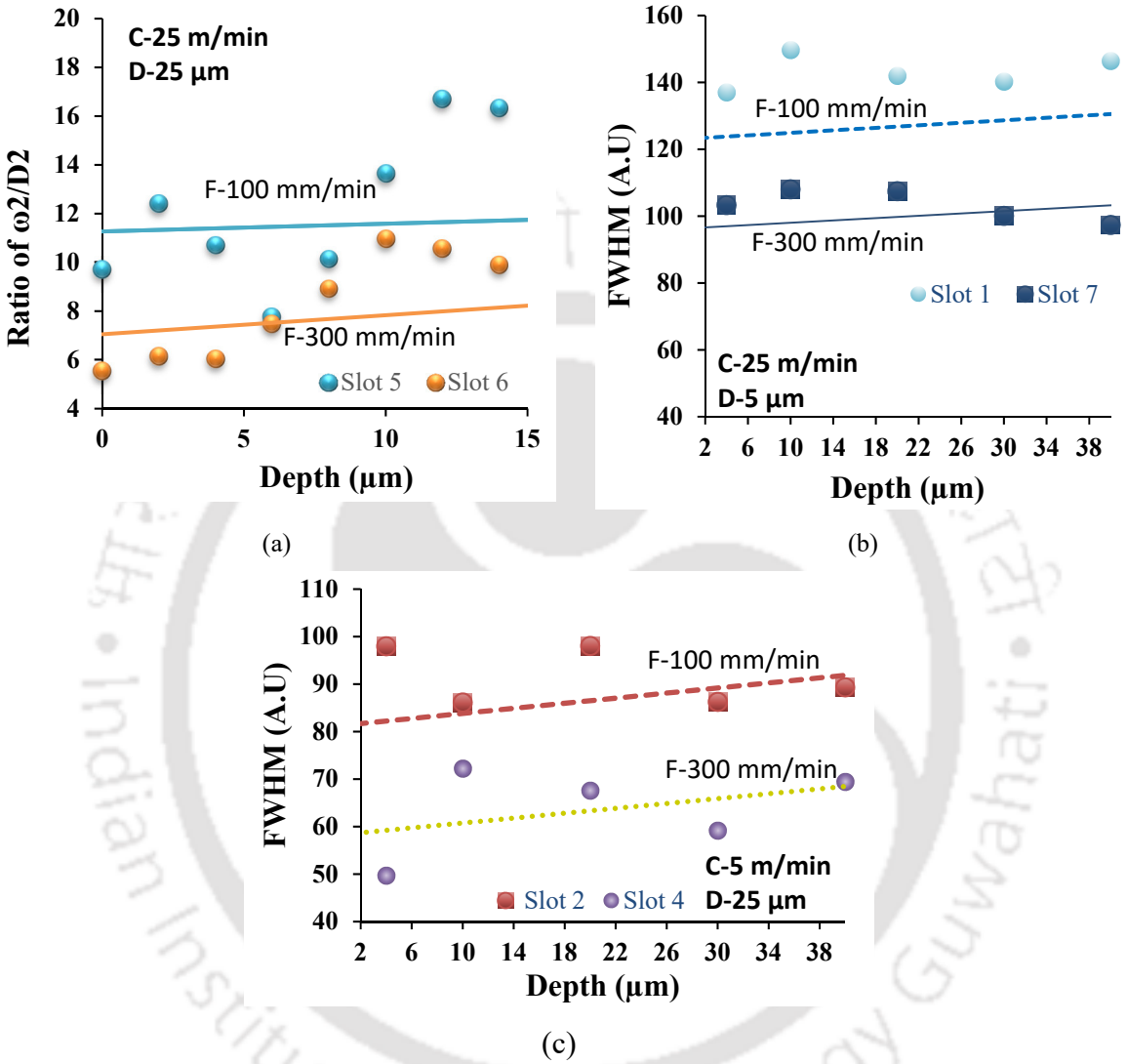

Fig. 5.10: FWHM of the six-membered ring with the depth of the machined substrate while changing feed rate at (a) cutting speed 25 m/min and depth of cut 25 µm, (b) cutting speed 25 m/min and depth of cut 5 µm, and (c) cutting speed 5 m/min and depth of cut 25 µm

5.10.3 Raman microscopy results with the variation of depth of cut

Depth of cutting (D) is another machining parameter that influences the substrate surface and subsurface characteristics. Figure 5.11 shows that with the increase in depth of cut from 5 µm to 25 µm, the chemical defect concentration also increases. Hence, the ratio of a six-membered ring to a three-membered ring decreases with an increase in the depth of cut. An increase in the depth of cut induces more indentation compressive load, leading to more

chemical defects. Similarly, Fig 5.12 shows that FWHM is also inversely proportional to cutting depth. An increase in cutting depth causes the substrate deformation's growth, leading to more distortion of six-membered networks, hence, less FWHM with depth.

The cutting speed, feed rate, and depth of cut are the three machining parameters that influence the surface and sub-surface characteristics of the brittle substrates. Lv et al. (Lv et al., 2016) studied these characteristics with SSD of the BK7 glass. A similar trend is noticed for these parameters for the fused silica substrate and Raman microscopy used to access the subsurface defects.

This study shows that SSD can be correlated in a non-destructive way using Raman microscopy. FWHM of the six-membered ring provides vital information about the plastic deformation of the substrate other than the analysis of chemical defects was done in most of the literature ((Xu et al., 2008) (Pilla et al., 2003) (Piao et al., 2000) (Xu et al., 2007) (Pilla et al., 2003) (Galeener and Geissberger, 1983).

The FWHM of the six-membered transition of Raman spectra provides vital information regarding the plastic deformation of the fused silica glass material. Due to the machining load, local crystallites are generated at the indented load. This local short-range crystallinity vibrates at a different frequency than the ideal six-membered ring. The local crystallinity causes the sharpening of the spectrum and reduction of FWHM. Hence, Raman microscopy can access the SSD and optimize the machining parameters for the brittle glass substrates. This study optimized the cutting speed of 25 m/min, the feed rate of 100 mm/min, and the depth of cut 5 µm to shape fused silica substrate using rotary ultrasonic machining.

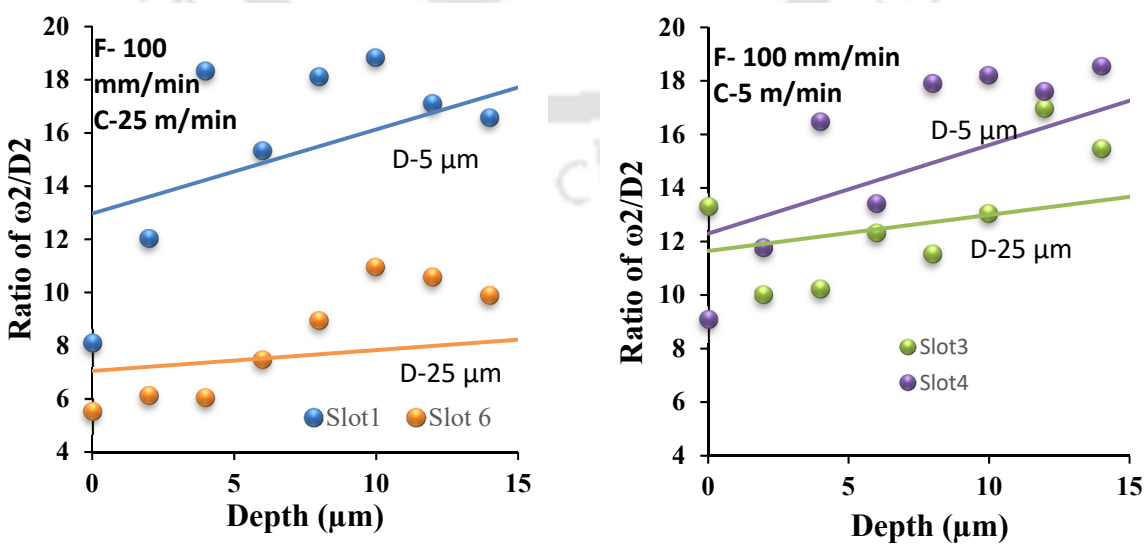

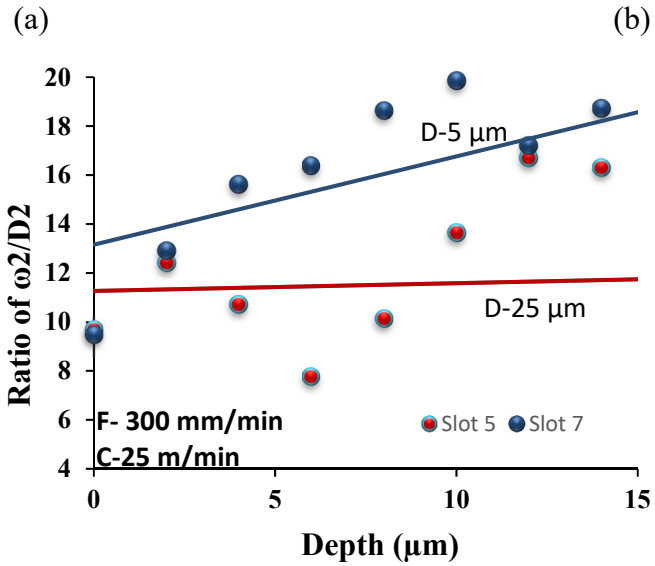

(c)

Fig. 5.11: Ratio of the area under the six-membered ring (800 cm-1) to three-membered (600 cm-1) ring with the depth of the machined substrate while changing the depth of cut at (a) feed rate 100 mm/min and cutting speed 25 m/min, (b) feed rate 100 mm/min and cutting speed 5 m/min, and (c) feed rate 100 mm/min and cutting speed 5 m/min

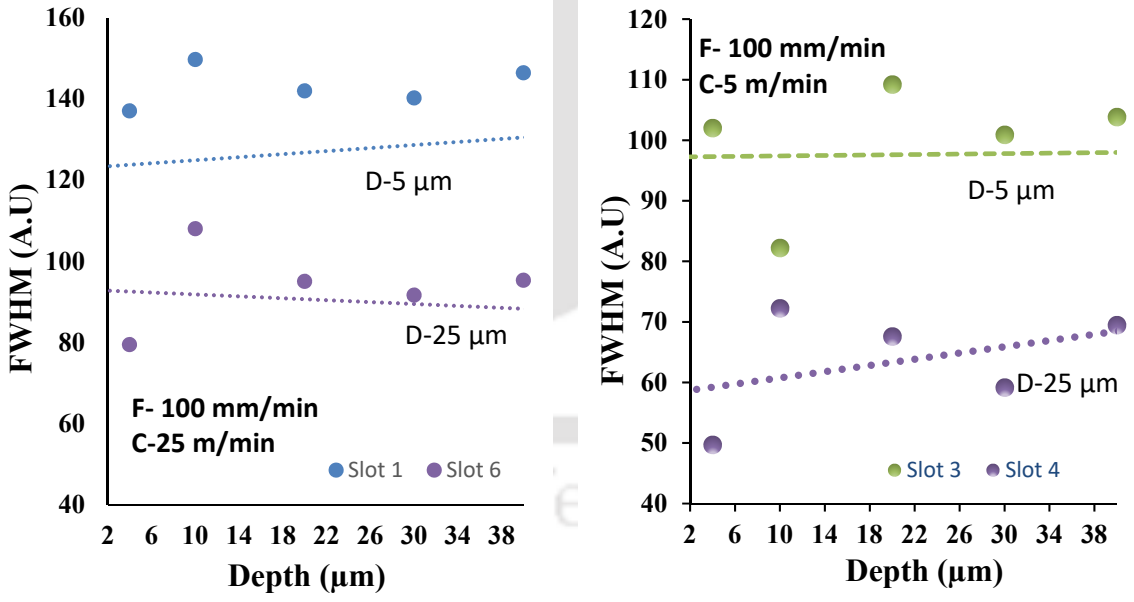

(a) (b)

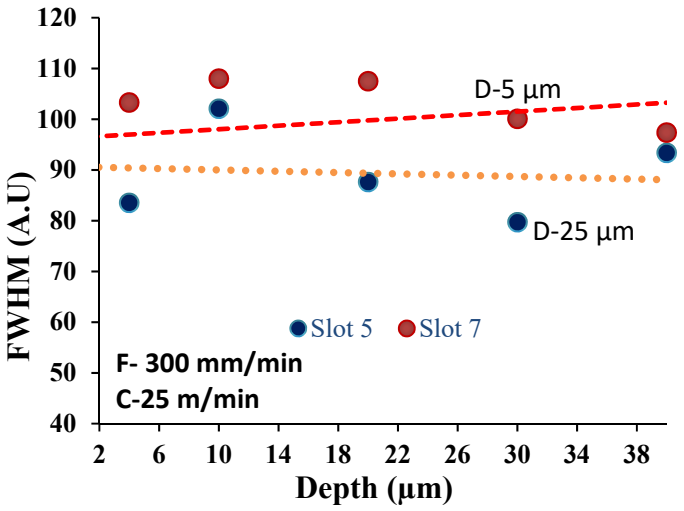

(c)

Fig. 5.12: FWHM of the six-membered ring with a depth of the machined substrate while changing the depth of cut at (a) feed rate 100 mm/min and cutting speed 25 m/min, (b) feed rate 100 mm/min, and cutting speed 5 m/min, and (c) feed rate 100 mm/min and cutting speed 5 m/min

5.11 Quantification of depth of damage of precision ground HRG shell and its correlation with Q factor

The previous study shows that RUM induces SSD, which extends to 40 to 50 µm for most machining parameters but extends to 20 to 25 microns for the optimized parameter. Hence, it is essential to eliminate this damaged layer with subsequent processing. Therefore, the precision grinding (DMG MORE make, model DMU 40, cutting speed 1200 rrpm, cutting depth 5 mm and machining diameter 200 mm) method was adopted to improve the surface quality and achieve strict dimension tolerances of the fused silica substrate. After the precision grinding using a jig grinding machine, the surface was analyzed using Confocal Raman microscopy to access the surface and subsurface defects. These results were compared with the ultrasonic machining substrate.

5.11.1 Comparison of ultrasonic machining with precession grinding

Generally, precession grinding is adopted for brittle substrates to achieve better foam accuracy, good surface quality, and improved surface integrity. For brittle material always preferable to have ductile machining to meet the above requirement. Hence, a ductile machine induces plastic deformation instead of chipping and subsurface cracking. Figure 5.13 shows the typical Raman spectrum of fused silica substrate machined by RUM.

Machine-induced compressive stress causes an increase in the concentration of D1 and D2 defect peaks, as shown in the section. In addition, there is an increase in the intensity of the D1 and D2 peak with proportional induced stress, and frequency shift also occurs due to distortion of inter-bonding angles. As shown in Fig. 5.13, the three-membered rings have peaked at a higher frequency at the surface than at depth. It suggests that the machined substrate shows more concentration of three-membered ring at the surface and stiffer bonds, hence, more compressive stress at the surface and relaxed with depth.

Figure 5.14 shows the Raman spectrum of precession ground fused silica substrate. Unlike ultrasonic machined substrate, there is no evidence of a shift in the frequency of the characteristic peaks. Also, the surface has a lesser defect peak concentration than the ultrasonic machined substrate and more secondary damage depth. Hence, it implies that grinding machining generally occurs at the ductile or brittle transition to the flexible regime for fused silica substrate. This observation has been reflected in the Raman spectrum, defects were observed after machining. But ductile machining can also induce compressive stress and cause plastic deformation to the fused silica substrate.

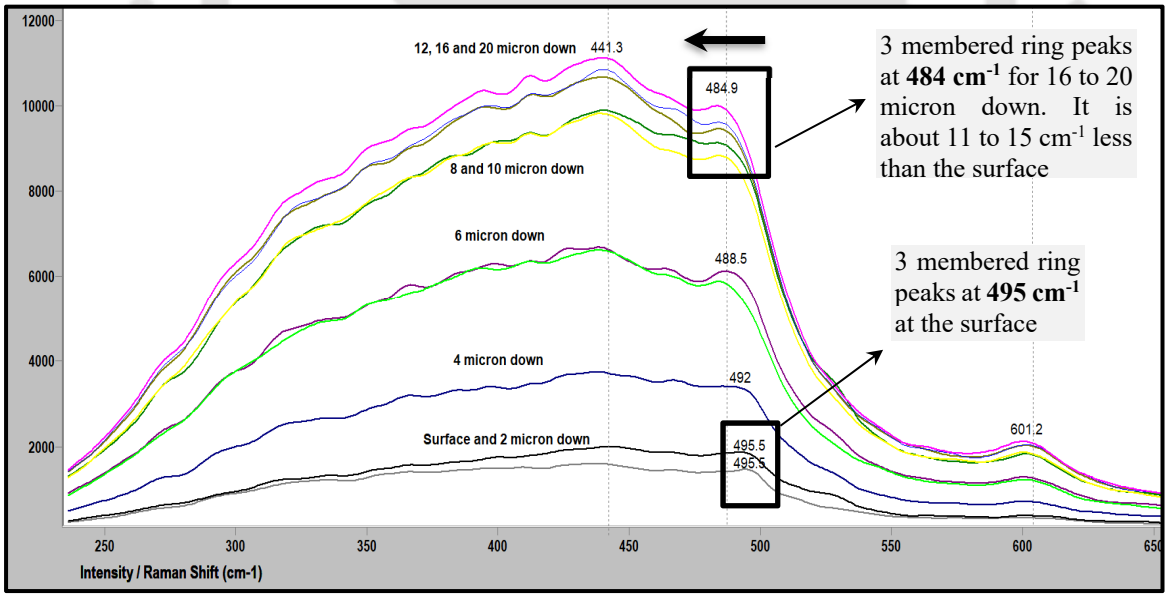

Fig. 5.13: Overlay Raman spectrum of ultrasonic machined HRG shell

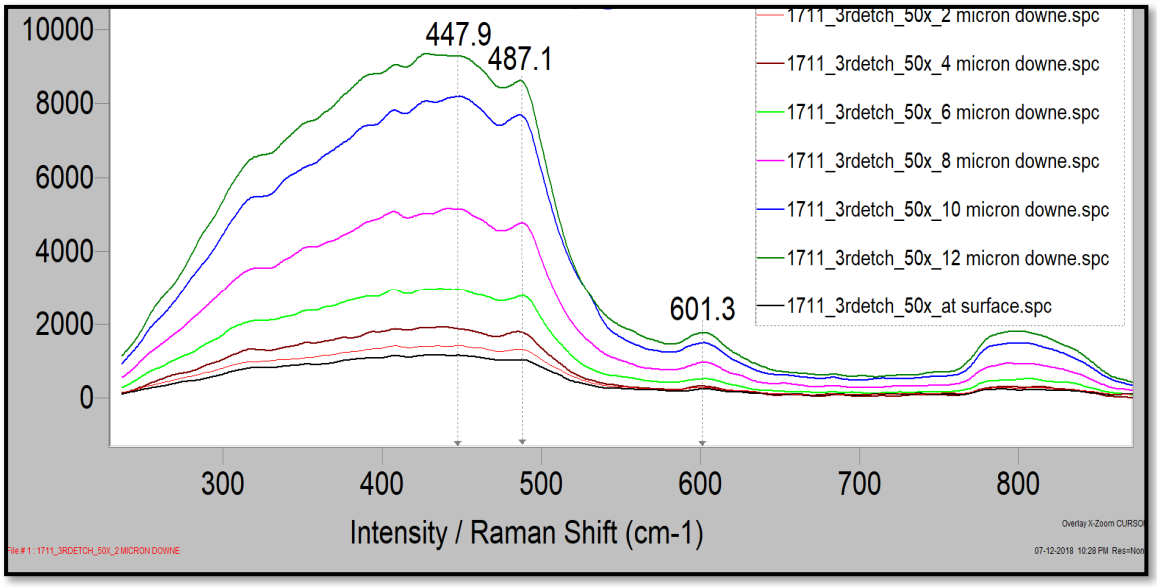

Fig. 5.14: Overlay Raman spectrum of precession ground HRG shell

Figure 5.15 shows the overlay spectrum surface at a 10-micron depth of the fused silica substrate machined by precision grinding. The surface six-membered broad peaks centered at 440 cm^{-1} becomes split into multiple sharp peaks compared to 10 micro depths, as shown in Fig. 5.15. This observation indicates the densification or compaction of surface layers due to compressive machining stress. This machine-induced stress disrupts the six-membered tetrahedral network of the fused silica surface; hence, variation in Si-O-Si angle proportional to pressure.

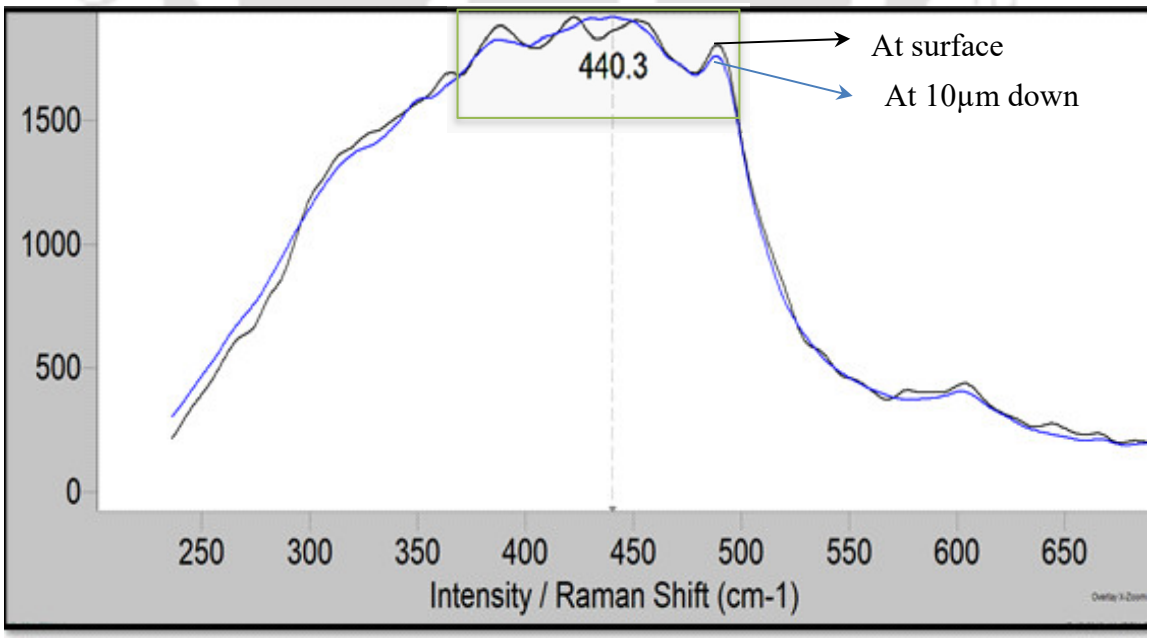

(a)

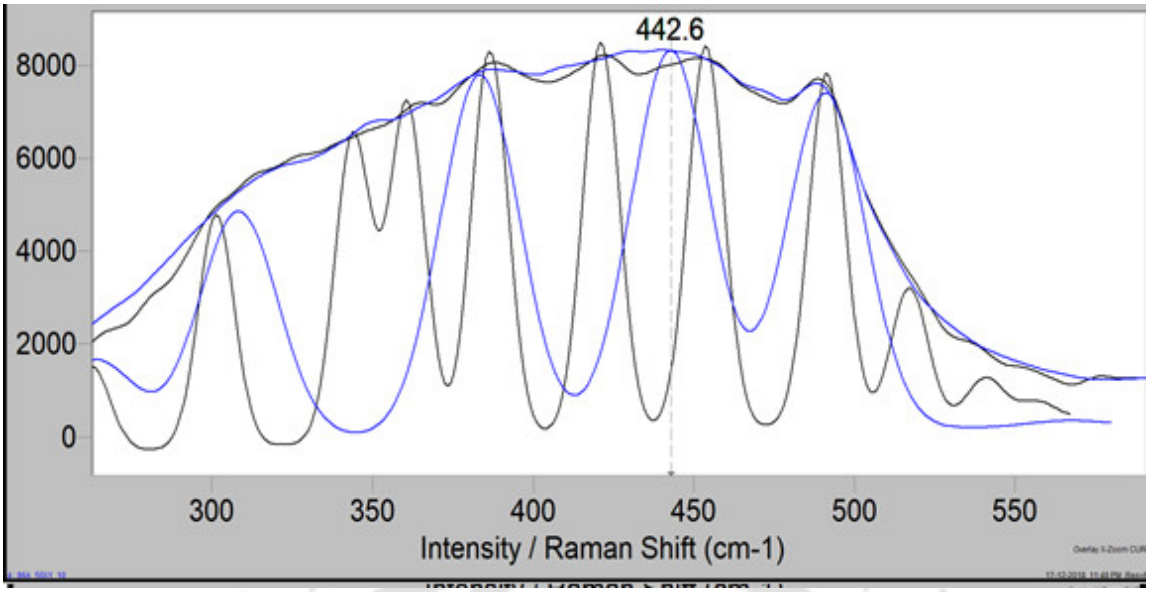

(b)

Fig. 5.15: (a) shows the overlay spectrum surface and at a 10-micron depth of the fused silica substrate (b) peak fitting of Raman spectrum captured at the surface machined by precision grinding.

Due to stress, the broad peak converted to multiple sharper peaks. Hence, the Full-Width Half Maximum (FWHM) of the characteristic six-membered peak of the Raman spectrum provides the direct correlation of stress. Hence, the variation of this FWHM with depth provides the stress distribution of the machined surface. Subsurface surface damage (SSD) depth can be calculated based on the interpretation of the FWHM of a six-membered ring.

5.11.2 Characterization of fused silica HRG shells

Hemispherical shells machined by the grinding process were characterized by Raman microscopy. As explained earlier, the sub-surface mechanical damage layers were formed during manufacturing. These damage layers significantly reduce the resonator's quality factor (Q). High Q is an essential parameter for resonators, which decides the final performance of the device. For a particular design and fused silica material of construction, the Q factor for the resonator predominately depends on the surface and subsurface chemistry of the molecular network. Hence, the resonator Q factor depends on the surface damage layers and the thickness of the mechanical damage layers. Therefore, in this study, the thickness of the damaged layer has been quantified with the help of Raman microscopy and verified the Q factor after machining and post-damage layer removal.

Hemispherical shells were fabricated using a jig grinding machine, and the Q factor of the resonator post-machining was analyzed using Laser Dopper Vibrometer (LDV) (Polytec make, model PSV I 500, 633 nm He Ne Laser, angular resolution <0.002°, angular stability <0.01°/h, max. 50 scan points/s). The depth of the damaged layers of each resonator was quantified using Raman microscopy. The damaged layers were removed using buffered oxide etchant. The post-etched substrates were analyzed using Raman microscopy, and the Q factor was also measured using LDV.

5.11.2.1 Procedure of Raman analysis

- Raman spectra of the HRG shell are taken before and after each process
- Spectra from the surface up to a depth of 20 microns are obtained with an accumulation time of 200 s using a 532 nm laser
- Post-processing operations like smoothing and peak fitting are done on the Spectra to accurately obtain the Full-width half maximum (FWHM).
- The FWHM trend indicates the surface stress layer, which differs from the bulk condition.
- This process quantifies the depth of the stress layer

5.11.2.2 Results and discussion

Figure 5.16 shows the typical Raman spectrum with peak fitting of the substrate after machining and post-etching. The broad peak at 440 cm^{-1} is attributed to the ideal six-membered Si-O-Si ring. The peak fitting of this broad peak reveals that broad peak is a combination of multiple (as shown in Fig. 5.16) peaks along with one 4-membered defect peak centered at 496 cm^{-1}.

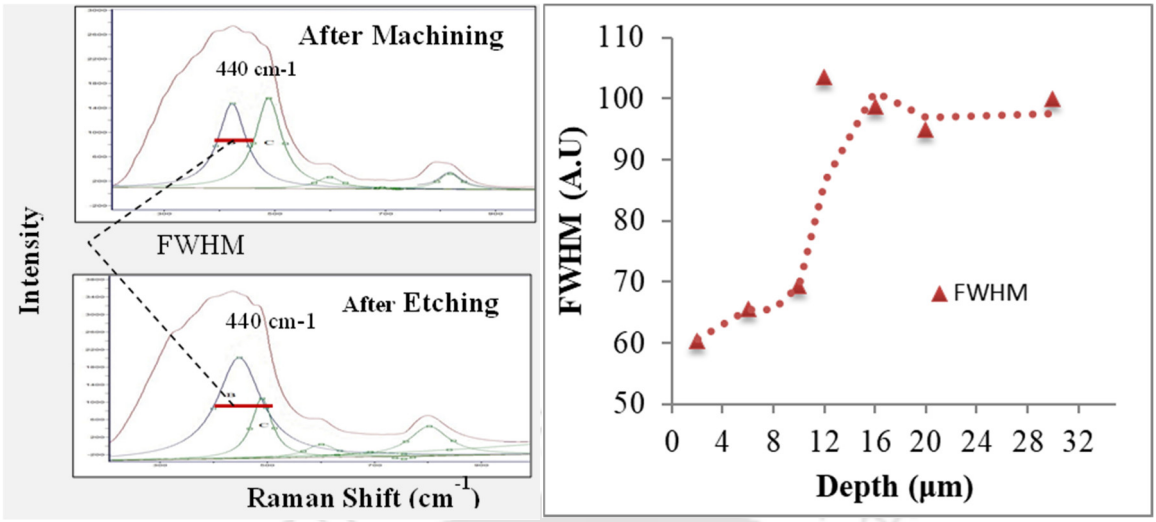

(a) (b)

Fig. 5.16: (a) Typical Raman spectrum of the fused silica HRG shell before and after etching along with its peak fitting and (b) variation of FWHM with the depth of the substrate

Post-measurement hemispherical shell etched to remove 15-micron thickness using buffered oxide etching solution (BOE etching using ammonium biflouride). Shell was again analyzed using Raman microscopy. Figure 5.17 compares the FWHM of the resonator shell after and before etching. Post-etching shell displays significant improvement in FWHM compared to after machining. It suggests that damaged layers have been entirely removed after etching hence, improvement in FWHM. Figure 5.18 shows the time domain curve captured by LTB before and after etching.

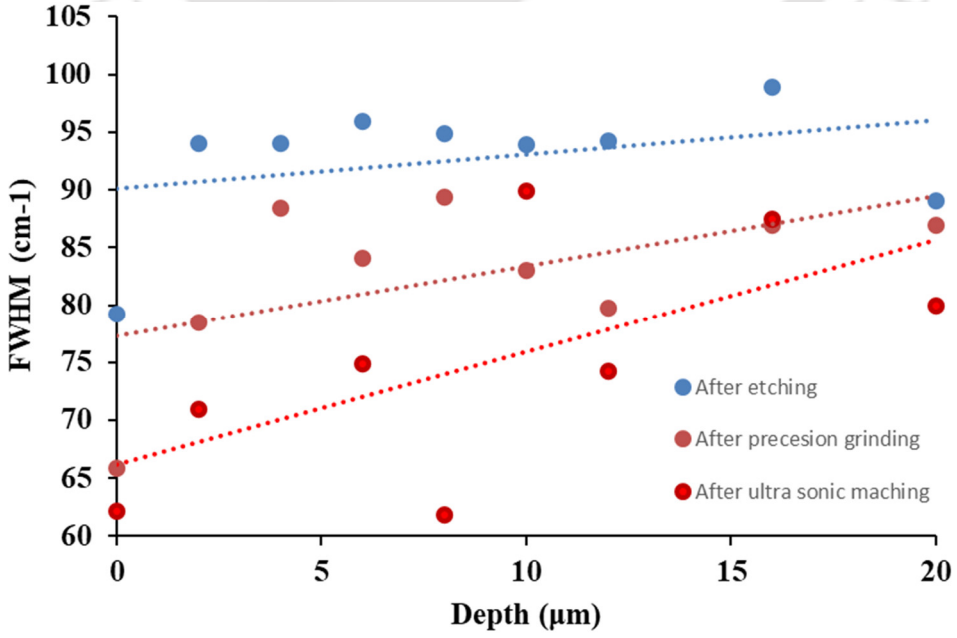

Fig. 5.17: FWHM of the shell at various stages of operation

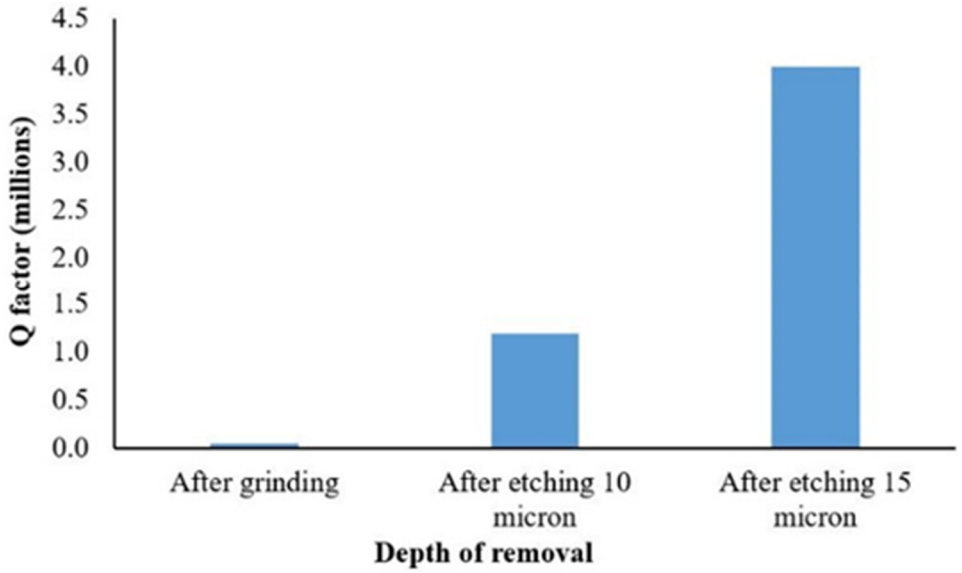

Fig. 5.18: Change in Q factor after removal of damaged layers

The Q factor was deduced from the plot before and after etching. A quantum jump in the Q factor was noticed after etching 15 microns as quantified by Raman microscopy. After etching, the Q factor is improved from approximately 0.05 million to 4 million. The improvement of the Q factor further indicates the enhancement of the surface integrity of the shell after etching.

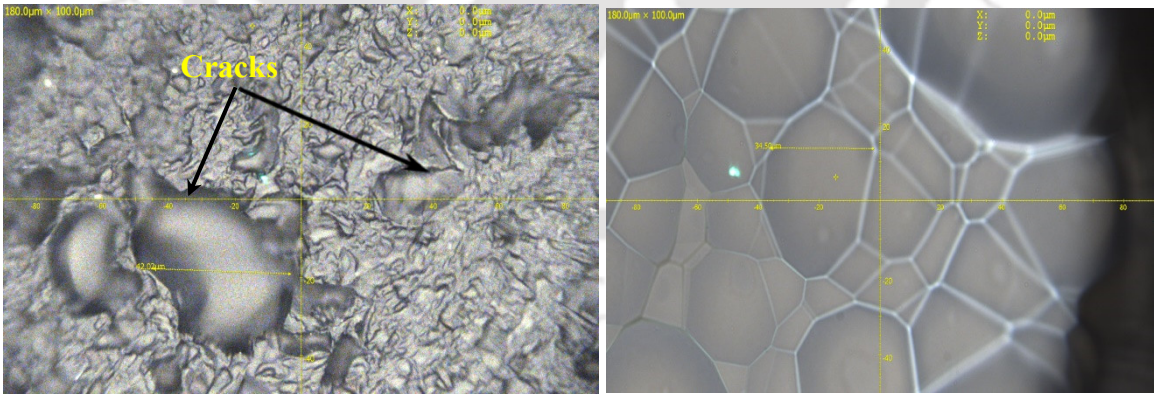

(a) (b)

Fig. 5.19: Images of the shell surface (a) after machining and (b) after etching at 50X captured by Raman microscopy

Figure 5.19 shows the Raman microscopic images of the shell surface captured at 50X before and after etching. As shown in Fig 5.19 (a), the machined fused silica substrate

resulted in many cracks and digs, but these cracks were removed during etching, as shown in Fig. 5.19 (b). Hence, it suggests that etching improves surface quality and eliminates the damaged layers. These results have complied with the FWHM values analyzed by Raman spectroscopy.

5.12 Summary

- This study utilized the confocal capability of Raman microscopy to quantify the damage depth of the machined and ground optics in a non-destructive way.
- A frequency shift of ideal six-membered transitions at the surface to bulk provides information about the machine-induced damage depth.
- Grinding induces plastic deformation or densification on the optics. The densification causes short-range local crystallinity in the optics. Hence, the Full Width at Half Maximum (FWHM) of the transition at the surface to bulk indicates the extension of plastic deformation in the optics.
- The ultra-sonic machining parameters such as feed rate, depth of cut, and cutting speed were optimized by analyzing the damaged depth using confocal Raman microscopy.
- The quality factor (Q) of the hemispherical resonator shell, which is the function of damaged layers for a given design and material, is measured using Laser Doppler Vibrometer (LDV).
- The Q of the shell at various stages was measured, and simultaneously, damage depth was analyzed using Raman microscopy. The Q factor was highest where stress analyzed by the Raman microscopy study was less. It shows that the developed non-destructive Raman microscopy methodology for quantification of damage depth was validated.

Chapter 6

Quantification and mitigation of defect layers of the ultrafine optics

---

6.1 Introduction

In Chapter 5, the non-contact and accurate methodology was developed to quantify sub-surface mechanical damage (SSD) layers of the fused silica on a micrometer scale using confocal Raman microscopy. Thus Raman microscopy failed to analyze the damaged layer of the substrates where the SSD exists only within the sub-nanometer range. Total internal reflection (TIR) prisms are critical optical components used in ring laser gyros (RLG) for navigation applications in the avionic sector. It acts as a corner optics for folding the Laser beam path, resulting in a reference standing wave interference pattern for measuring a precision rotation angle using the Sagnac effect. Furthermore, in RLG beam passes through the bulk of the TRP. Therefore, the surface-to-bulk characteristic is critical for the application.

High-quality total reflecting prisms used in ring laser gyros need ultrafine smoothness and defect-free surface chemical bond structure. Generally, optical prisms are fabricated sequentially, which includes shaping the optics, abrasive grinding, second grinding with

fine abrasives, polishing using CeO_2 abrasive (chemo-mechanical polishing), small aperture figuring, etc., as shown in Fig. 6.1. This complete procedure results in ultrafine surfaces with a surface roughness of less than 5 Angstrom units. Thus, these processes induce numerous structural, mechanical, and chemical defects at the surface and subsurface in the nanometer range. Therefore, the presence of these damaged layers has a detrimental effect on the device's performance in continuous operation. In addition, it affects the device's lifetime under constant laser radiation.

Fig. 6.1: Standard polishing methods

6.2 A probable mechanism for device failure

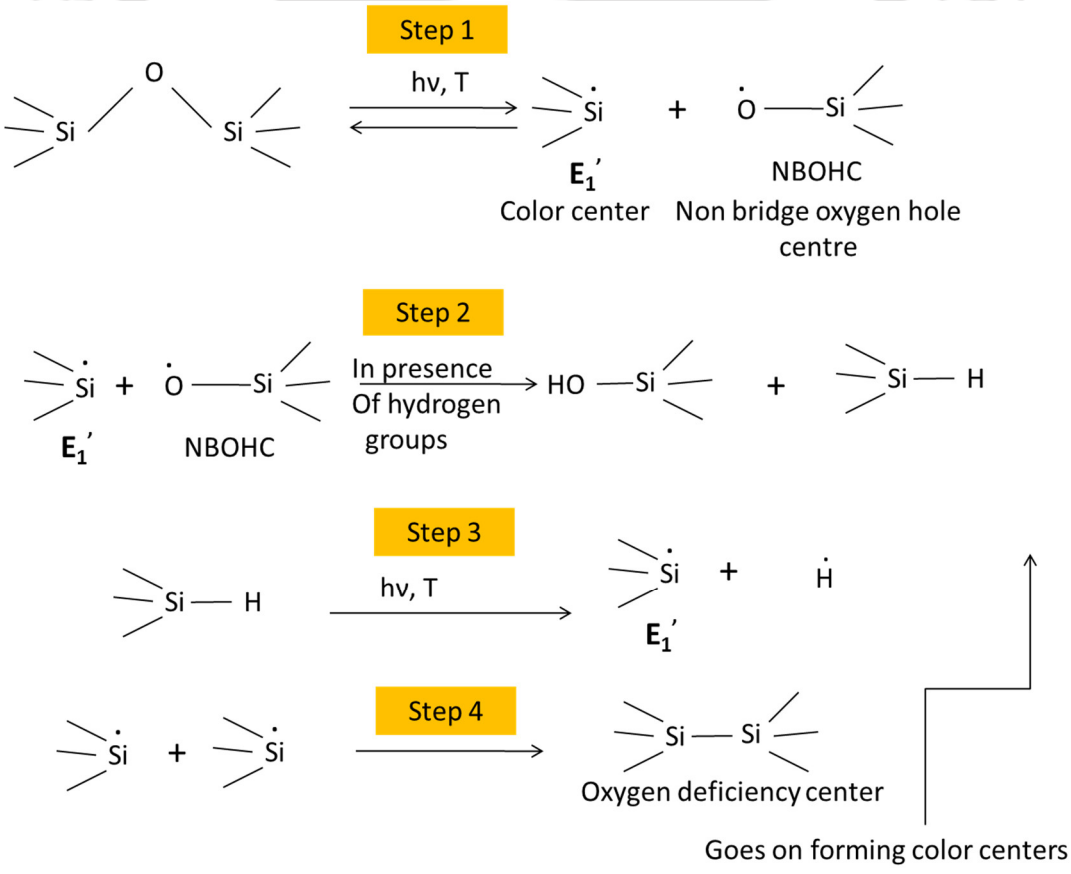

Fig. 6.2: Mechanism of color center formation

These damaged layers act as an absorbing centers called color centers. These color centers drastically reduce the optics' transmission, reducing the device's output power. The Color center is generated due to the catalytic activity of the incident photon. It depends on the cumulative fluence of the photon radiation. As it is a time-dependent phenomenon, the device performance deteriorates with time. The mechanism of color center formation is shown in Fig. 6.2 (Liu et al., 2003). The mechanism suggests a damaged layer is a precursor for the color center formation.

6.3 Characterization of color centers

The above mechanism leads to sub-oxide formation, which changes surface polarity. These stoichiometric surface changes act as active UV and visible radiation absorption centers. To understand this mechanism and validate the above mechanism, the substrate exposed to continuous laser radiation was analysed using a fluorometer. Figure 6.3 shows the photoluminescence spectrum of the substrate. It shows the characteristic peak at 350 nm, attributed to the oxygen deficiency centre (Zhou et al., 2014a). To improve the device's lifetime, it is essential to quantify the depth of damage to the ultrafine fused silica substrate and eliminate it without affecting the surface quality.

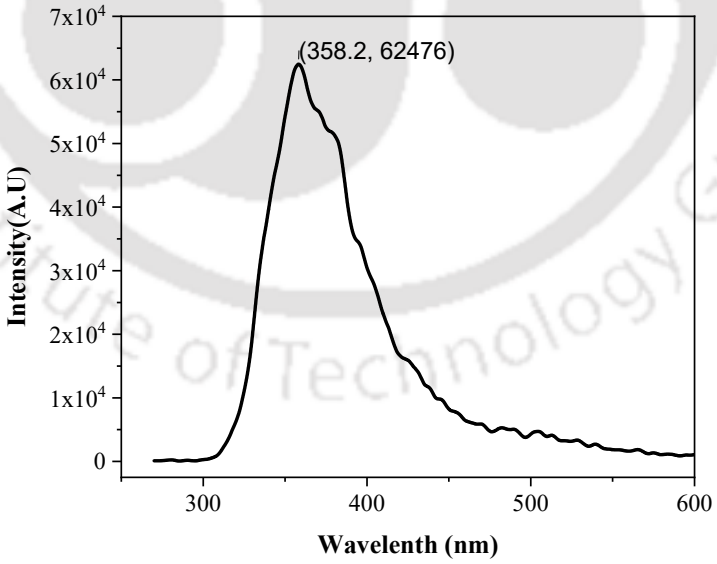

Fig. 6.3: Photoluminescence spectrum of prism substrate

6.4 Quantification of damaged layers of the ultra-fine fused silica substrate

Material removal occurs during polishing below the fracture limit by nano-plastic deformation or chemical reaction. Nano plastic deformation induces densification or brittle cracks on a nanometer length scale. Material removal by chemical reaction generates a modified amorphous or hydrated layer called the Beilby layer. Polishing causes, mechanically and structurally, are distinctly different from the bulk characteristics, as shown in Fig. 6.4. These damaged layers have a lower laser damage threshold than the bulk due to luminescence defects. Hence, continuous Laser exposure causes significant degradation to the properties of the optics.

As these layers are very thin poses challenges to characterize them. However, a few techniques are reported here for characterizing these thin layers. Trogolo and Rajan (Trogolo and Rajan, 1994) imaged the cross-section of the Beilby layers using transmission electron microscopy, later by Lodha et al. (Lodha et al., 1998). The cross-section image shows two distinct layers extending up to 15 to 20 nm. Liao et al. (Liao et al., 2014) carried out a similar study using field emission scanning electron microscopy. Yokota et al. characterized the surface's refractive index and substrate's bulk using X-ray reflectivity and ellipsometry. This study confirms a higher refractive index of about 0.003 to 0.005 at the surface than at the bulk (Yokota et al., 1964). Thus, in this study, the X-ray photoelectron spectroscopy technique utilized to analyze the chemical network change caused due to plastic deformation, the secondary ion mass spectroscopy (SIMS) method for characterizing the Beilby layer of the ultra-fine prism substrate, and the analysis of luminescence defects using photoluminescence method.

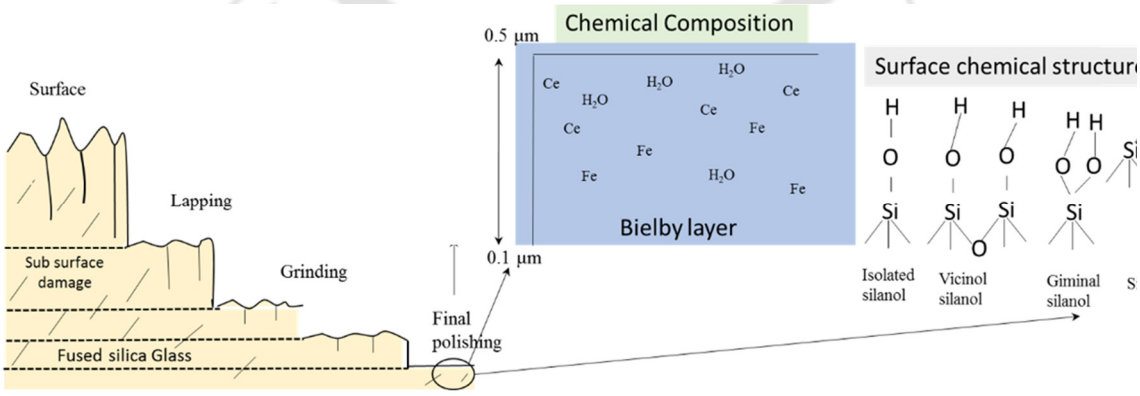

Fig. 6.4: Typical chemical defects after final polishing of the fused silica substrate

6.4.1 Characterization of plastic deformation

Plastic deformation induces densification, which causes the deformation of the silica network. The comparative XPS results before and after plasma processing were described in the chapter.

6.4.2 Characterization of Beilby layer

The Beilby layer was formed during chemo-mechanical polishing, where material removal occurs due to the chemical reaction of cerium oxide with the silica surface. Hence, the chemical interaction of Ce causes diffusion of Ce impurities into the bulk or adsorb at the surface can modify the chemistry of the fused silica surface layer. These impurities exponentially reduce with depth. Hence, the fused silica's texture and depth were analyzed using SIMS for various impurities like Ce, Fe, K, etc.

6.4.3 Analysis of photoluminescence

Photoluminescence was analyzed using Steady-State Fluorescence Spectro-fluorometer. The substrate is illuminated with a laser wavelength of 266 nm and captures the emitted fluorescence using a photomultiplier detector. This analysis provides insight into various luminescence defects present in fused silica substrates.

6.4.4 Results and discussion

Figure 6.5 shows the atomic concentrations of various atoms such as cerium (Ce), potassium (K), iron (Fe), and silicon (Si) with the depth of the CMP polished fused silica substrate. The results suggest that the contaminations reduce significantly with depth profile. Thus, K and Fe are present mainly at the surface where the Ce atoms distribute at the bulk of the substrate till 200 nm. Hence, in these particular substrates, the Bielby layer predominately contains the Ce atoms to the depth of 300 nm.

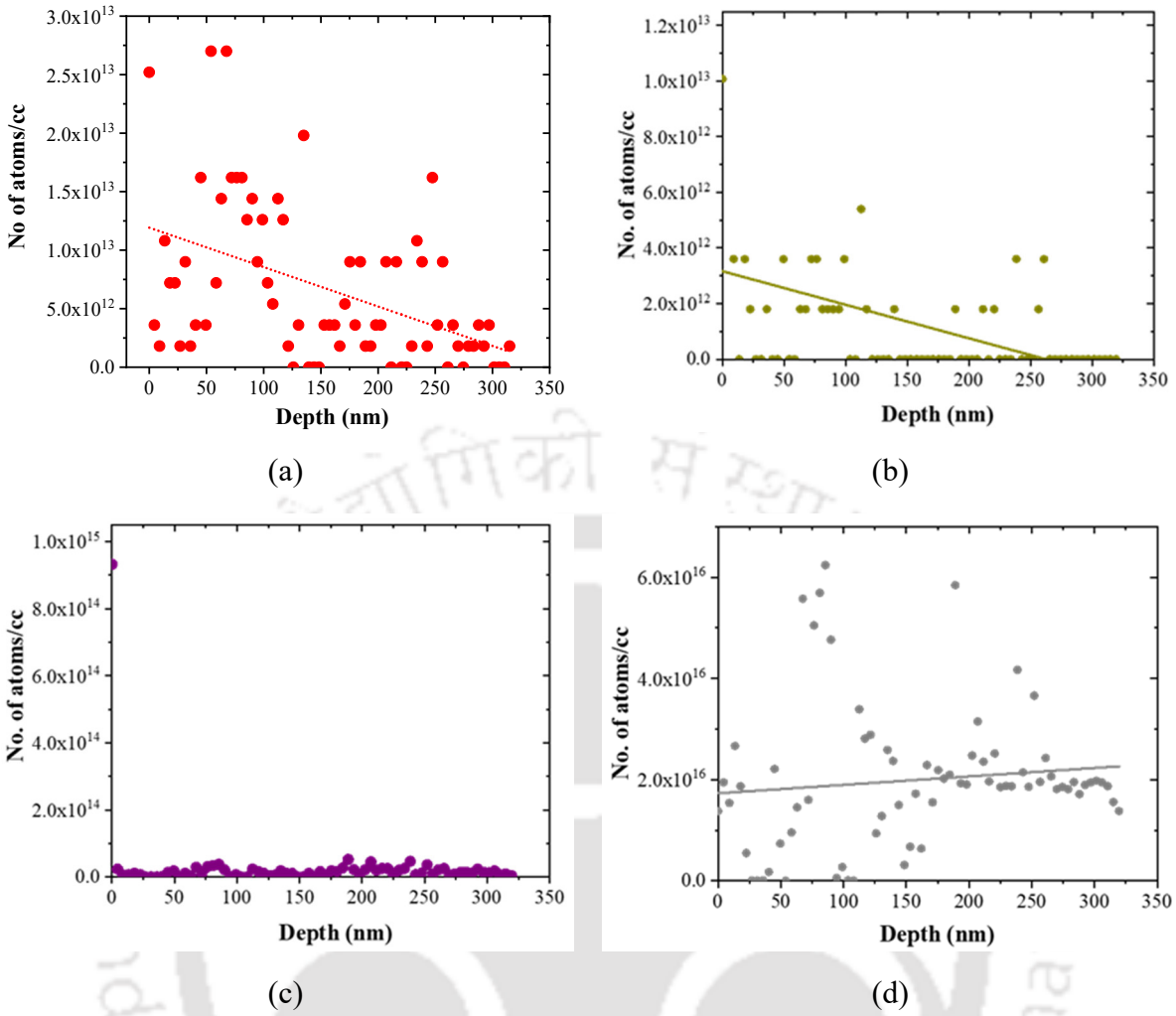

Fig. 6.5: Concentration of (a) Ce, (b) K, (c) Fe, and (d) Si atoms per CC of the ultra-fine optical prism after polishing analyzed by SIMS

The slope of the trendline indicates a reduction of Ce concentration with the depth of the substrate. The trendline slope for the Si atom remains constant with the deep as expected. Hence, it suggests that the SIMS results correlate well with the atoms. The silicone atoms can be a reference for understanding the relative ratio of the foreign atoms. The results show that one Ce atom presents out of 200 Si atoms (Si: Ce- 200:1), which is two-fold higher than the one studied by Suratwala et al. (Suratwala et al., 2015). The adopted CMP method is not deterministic to achieve surface integrity, combining surface quality and surface chemistry.

The mechanism of the output power reduction of the device with time was understood and verified using photoluminescence spectroscopy. The results suggest that a very thin polished layer acts as an absorbing center, and the absorption of the radiation increases with time with metallic impurities in the Bielby layer. The characterization methodology was

established for quantifying the ultrafine fused silica substrate's very thin polished damaged layers. The results suggest that the adopted CMP methods are not deterministic to achieve surface integrity concerning surface metallurgy.

6.5 Improvement of surface integrity of ultrafine fused silica

As studied in section 6.4, Ce is the major impurity redeposited during polishing. Wet Etching using hydrofluoric acid (HF) or buffered oxide etchant (BOE) is the established method to remove the damaged layer and improve the surface quality of the fused silica optics (Ye et al., 2015), (Zheng et al., 2012), (Liu et al., 2014). Thus, fluorine-based etching often suffers from the following disadvantages:

- HF/HNO3 etching causes homogenous scattering haze throughout the surface. Acid etching also increases surface roughness and degrades surface quality (Pfiffer et al., 2017).
- Also, the HF etching process under static and uncontrolled conditions leads to the redeposition of silica compounds and absorbing defects (Suratwala et al., 2011).

Pfeiffer et al. (Pfiffer et al., 2017) adopted the alkali etching of fused silica using a KOH solution, which has an advantage over acid etching. KOH etching displays no change in the surface quality of the fused silica substrate. The material removal rate of the KOH solution could be better. It causes diffusion of K impurities, acting as an absorbing center.

Hence, this study adopted a plasma polishing methodology to eliminate the plastic deformation layer through non-contact means. A chemical leaching process was established to eradicate the Ce concentration after the plasma polished surface. SIMS analysis was carried out for the ultrafine substrate after plasma processing to verify the effectiveness of the process.

6.5.1 Plasma polishing process

The plasma polishing method removes the 200 to 300 nm damaged layer without affecting the surface roughness and quality. Various experimental trials were carried out to achieve the above-said goal. The plasma-processed prisms were screened using a laser screening jig, as shown in Fig. 6.6 The jig contains three known TIR prisms bonded by optical contact, and to complete the resonator, the test prism is kept very close to the fourth side, which meets the in-situ resonator.

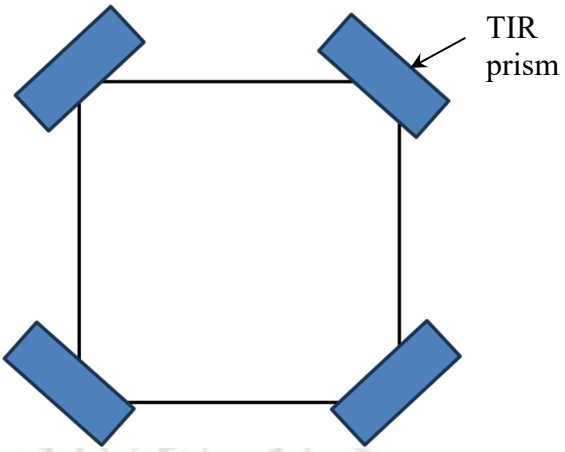

Fig. 6.6: Schematic of the laser screening jig

The generated laser beam was used to characterize the test prism before and after processing. This laser screening jig was used to describe the surface quality of the post-plasma processed prisms.

Table 6.1: Experimental trials for plasma processing

Exp. Trial no.	**Processing conditions**	**Removal (mg)**	**Observations under screening jig**	**Remark**
1	SF6-2.8 sccm (1.1 mbar), O2-0.5 sccm (0.5 mbar), He-100 sccm(18.5 mbar), **40 W power, 4 minutes processing time**	0.2 (120 nm)	**No beam** after processing. suspected contamination	0.2 mg removed after ultrasonic cleaning
2	SF6-2.8 sccm (1.1 mbar), O2-0.5 sccm (0.5 mbar),He-100 sccm(18.5 mbar),**40 W power,4 minutes processing time**	0.2 (120 nm)	**No beam** after processing. suspected contamination	Weight reduction of 0.1 mg observed after ultrasonic cleaning
	Plasma Cleaning (O2-2 sccm (2.5 mbar), He- 30 sccm (6.5 mbar), duration:5 minutes			Degassing cycle

The valve was changed to reduce contamination suspected deposition during air admittance.				
3	SF6-2.8 sccm (1.1 mbar), O2-0.5 sccm (0.5 mbar), He-100 sccm (18.5 mbar), **40 W power, 4 minutes processing time**	0.2 (120nm)	The beam was there but worsened after processing. Still worse after wiping	
Chamber was cleaned, the glass lines cleaned, and degassing was done.				
4	SF6-4 sccm (1.1 mbar), O2-0.5 sccm (0.5 mbar), He-130 sccm (18.5 mbar),**40 W power, 4 minutes processing time**	0.3 (180 nm)	The beam was after that processing but deteriorated in shape of the beam. Defects formed during cleaning	0.2 mg weight reduction observed after ultrasonic cleaning
It shows surface finish gets deteriorates after plasma processing.				
Trials with Reduced power of 20 W				
5	SF6-4 sccm (1.1 mbar), O2-1 sccm (0.5 mbar), He-130 sccm(18.5 mbar), **20 W power, 4 minutes processing time**	0.1 (60 nm)	The beam obtained after processing was thin. Surface scattering had increased.	Suspected that non-uniform processing is taking place. The material removed from one surface gets deposited on another. So it was decided to use multiple electrodes.
6	SF6-3 sccm (1.1 mbar), O2-0.4 sccm (0.5 mbar), He-130 sccm(18.5 mbar), **20 W power, 4 minutes processing time**	0.1 (60 nm)	The beam obtained after processing was thin. Surface scattering had increased.	Non-uniform gas flow due to Helium Cylinder leakage. In this trial, two electrodes were kept perpendicularly using 2 RF generators. The trial has to be repeated.

Re-deposition can be minimized by following the ways • Introduced the degassing cycle during the plasma process, but beam condition becomes worst with degassing cycle (Low-pressure degassing may induce more external contamination) • Plasma processing was done after chemical cleaning (still redeposition sustains) • Reduce the continuous operation from 4 mins to 0.5 min.				
7	SF6-3 sccm (1.1 mbar), O2-0.4 sccm (0.5 mbar), He-130 sccm(18.5 mbar), **20 W power, 0.5 minutes processing time**	No weight loss	Beam was intact	No weight loss after cleaning also. 0.5 mins may not be sufficient
8	SF6-3 sccm (1.1 mbar), O2-0.4 sccm (0.5 mbar), He-130 sccm(18.5 mbar), **20 W power, 1 minute processing time**	0.1 mg (60 nm)	Beam was intact	Optical contact also achieved

Plasma processing was established without affecting the surface quality. Thus, a slight scattering increase was noticed after plasma processing. To understand the scattering phenomena, the TIR prism's surface was analyzed using scanning electron microscopy (SEM) (Fig. 6.7) integrated with energy dispersive x-ray spectroscopy (EDX).

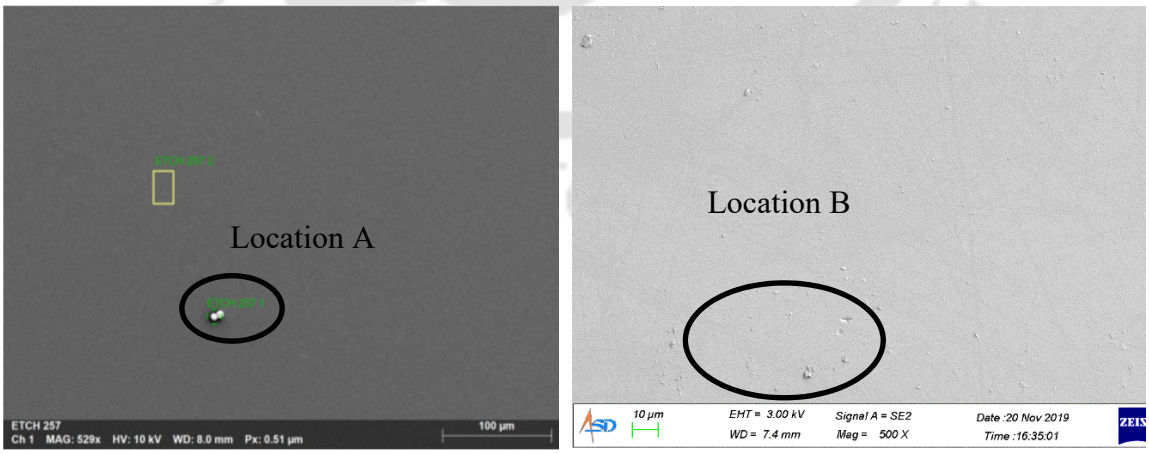

(a) (b)

Fig. 6.7: SEM images after plasma processing before chemical leaching at locations (a) and (b)

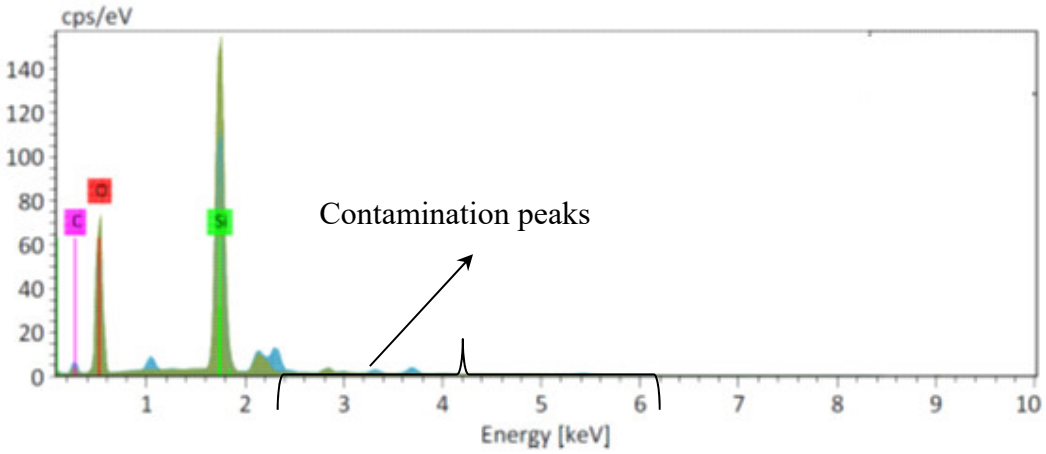

Fig. 6.8: EDAX spectrum before chemical leaching

After plasma processing, the SEM images show micron and submicron contamination on the fused silica substrate. The scatter sites were identified as deposits. In addition, the energy dispersive x-ray spectroscopy (EDAX) indicates various contaminations like Ce, Al, and traces of C (as shown in Fig. 6.8). Figure 6.8 shows the EDX spectrum of the scatter deposit. The deposit was identified as Ce contamination. After plasma processing, the contaminations present at a depth of 300 nm were exposed to the surface as described in Fig. 6.9, the schematic of the fused silica surface before and after plasma processing.

Hence, it is essential to remove this contamination from the surface; the chemical process established is called leaching to remove surface metallic contaminations.

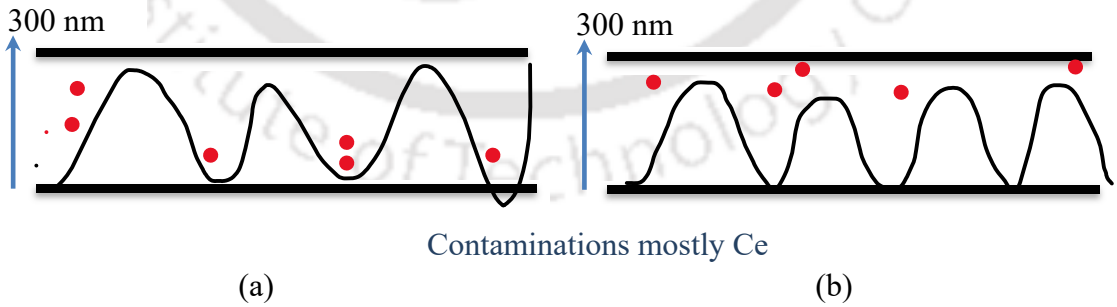

Fig. 6.9: Schematics of the surface profile (a) before and (b) after plasma processing

6.5.2 Establishment of chemical leaching process

The chemical leaching process should eliminate the above contaminations without affecting the surface quality of the ultrafine prism. The chemical selected for the experiment is described in Table 6.2.

Table 6.2: Selection of chemicals for leaching

Chemicals	Indented purpose
Concentrated hydrochloric acid	To remove metallic contaminations like Al and Ce etc.
A mixture of HNO_3 and H_2O_2	For oxidizing the carbon contamination as well as the leaching of minerals
A mixture of ammonium hydroxide and H_2O_2	Bleaching biological contamination and neutralizing acid traces

Table 6.3: The experimental trials were conducted to optimize the chemical leaching procedure

Exp. Trial	Procedure	Screening under jig	Inference
1	Treated with con. HCl solution for 30 minutes. Followed by cleaning in DI water	Visible patches were found on the surface.	Patches may be formed due to the reaction of an acid with a prism surface.
2	Treated with 50% HCl solution for 30 minutes. Washing in hot DI water.	The condition was better. No visible patches.	Fine traces were still present.
3	Treated with 50% HCl under an ultrasonication bath	No visible improvement by ultra-sonication.	Same as the previous trial.
4	Treated with 15% HCl	After cleaning condition worsened	Metallic impurities are not eradicated. Hence,

	50% HCl is optimized for further experiments as diluted solution helped to dissolve salt traces formed during the reaction with HCl		
	Trials to remove fine spots		
5	a. Treated with 50% HCl for 30 mins, followed by washing under hot DI water. b. Treated with 3:1 HNO3 and H_2O_2 solution for 30 mins and followed by washing under hot DI water.	Fine spots got eliminated, but the beam was deformed due to patches.	It May be formed due to the presence of untreated acid traces.
6	Trial 5 was followed by treatment with ammonia solution and H_2O_2 solution	Condition improved significantly	Improvement in condition may be due to the removal of acid traces by ammonium solution.
7	Other conditions are as in trial 6, but treatment with ammonia solution and H_2O_2 solution was under an ultra-sonication bath.	Patches were removed completely	Ultra sonication helped to remove patches (acid traces) effectively
	A chemical leaching procedure was established to remove fine deposits after plasma processing.		

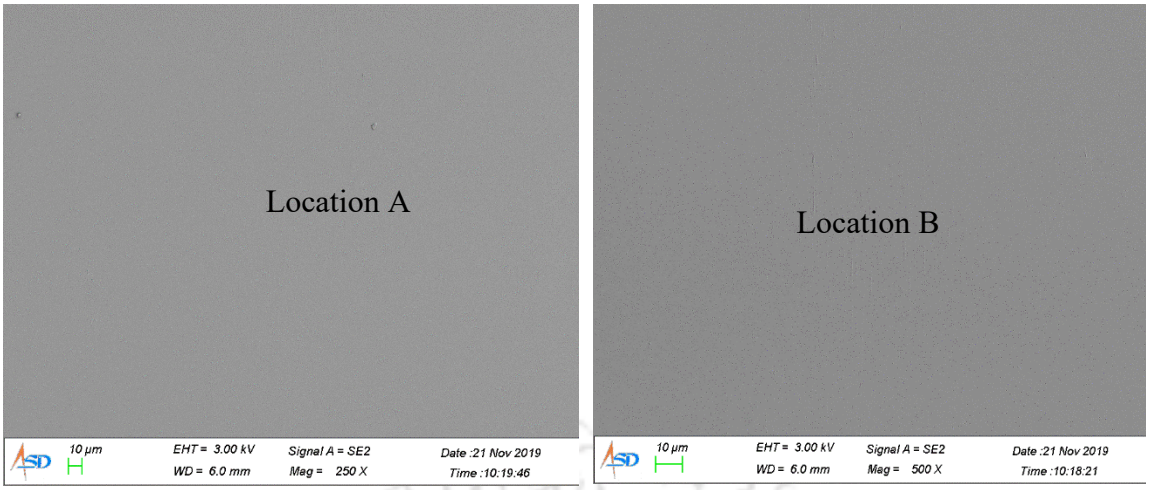

(a) (b)

Fig. 6.10: SEM images after chemical leaching at locations (a) and (b)

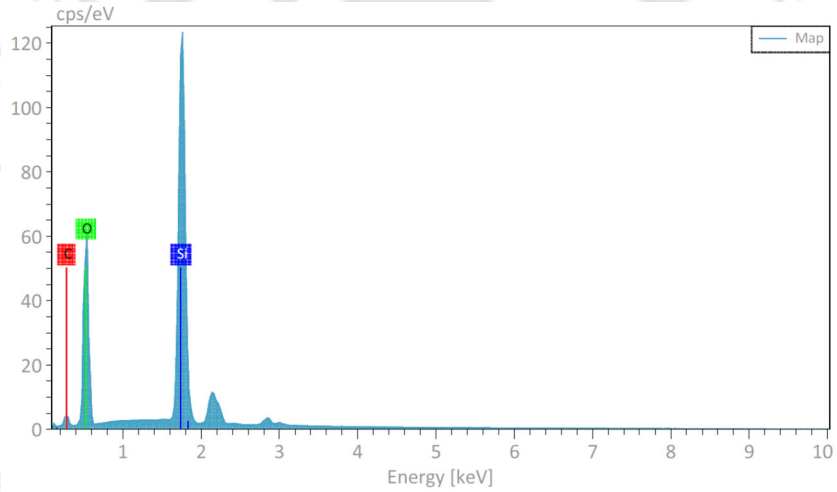

Fig. 6.11: SEM images after plasma processing after plasma processing and chemical leaching

Post-chemical leaching samples were analyzed using SEM, as shown in Fig. 6.10. No spots and contaminations were present. The EDX spectrum shown in Fig. 6.11 also confirms the absence of contaminations and the presence of only silicon and oxygen.

6.5.3 Characterization of ultrafine prisms after plasma treatment

Ultrafine prisms were treated with medium-pressure plasma to remove the thin, damaged layer, and subsequently, prisms were chemically leached to remove the diffused metallic contaminations. Thus, to ascertain the elimination of the plastic deformation layer and Beilby film, the plasma-treated substrates were analyzed again using x-ray photoelectron spectroscopy (XPS) and SIMS.

6.5.4 SIMS Analysis of prisms after plasma processing

The Comparison of Ce atomic concentration is shown in Fig. 6.12 (a). it suggests a significant reduction in Ce atom concentration after plasma processing and chemical leaching. Similarly, the number of Si atoms per Ce atom is shown in Fig 6.12 (b). it indicates that plasma processing followed by chemical leaching helped reduce Ce concentration from 200: 1 to 3000 :1 (Si: Ce).

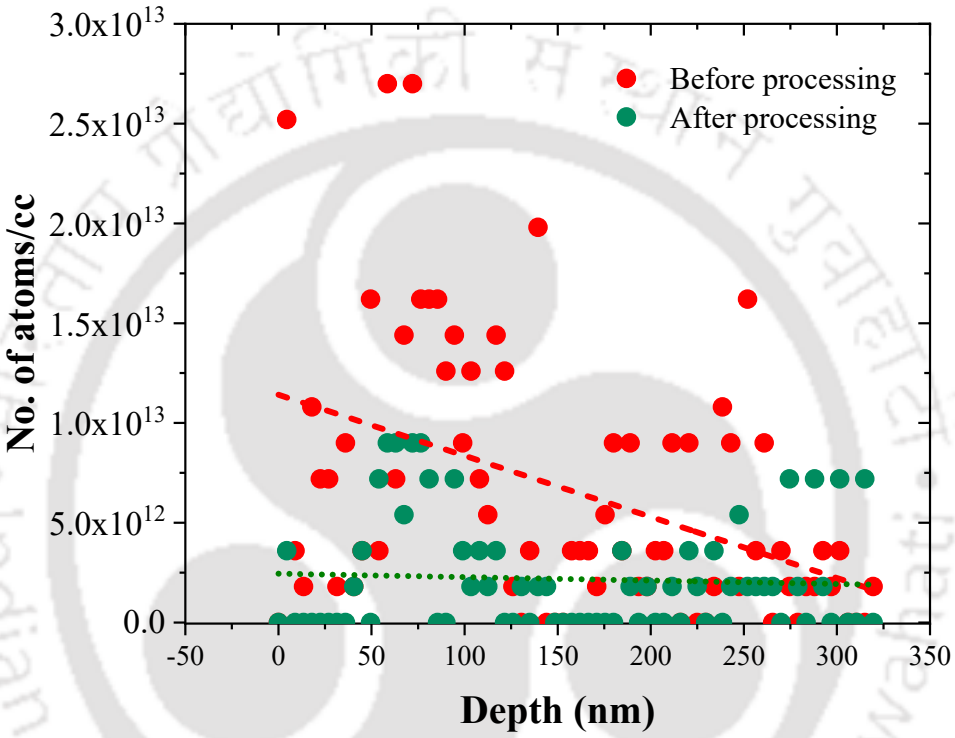

(a)

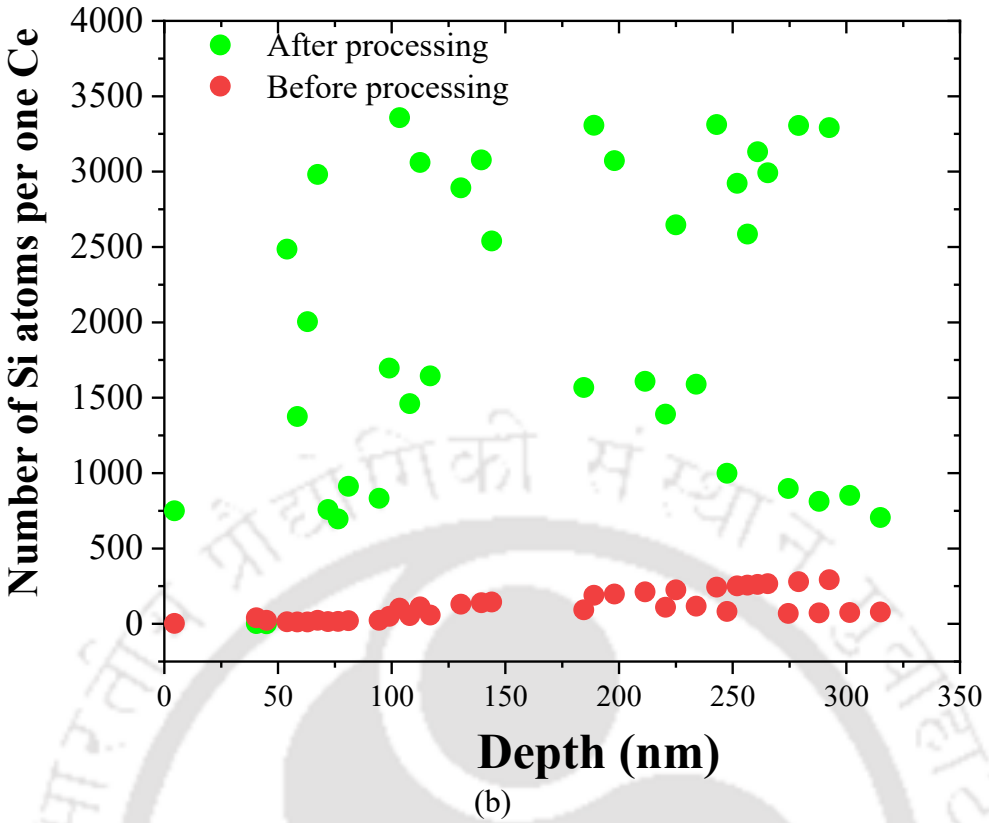

(b)

Fig. 6.12: Comparison of SIMS spectra (a) concentration of Ce atom and (b) number of Si atoms per Ce atom with the depth of the prism substrate

6.5.5 Characterization of photo luminescence defects

SIMS successfully analyzed the presence of trace polishing impurities at the subsurface of the fused silica substrate. The chemical network defects, especially oxygen deficiency centers (ODC), proved detrimental to the laser transmission of high precession fused silica substrate. (Salh, 2011). Therefore, fluorescence spectra for different depths of sample removal were analyzed to optimize the depth of removal for improving Laser-induced damage threshold characteristics of fused silica. Thus, fluorescence analysis was done for different material removal depths to quantify chemical defects at the surface of the ultra-precession fused silica.

Figure 6.13 shows the overlay of a fluorescence spectrum of samples plasma processed for different depth removal. Florence spectra centered around 380 nm attributed to the oxygen deficiency center (ODC). The shoulder peak at 382 nm arises due to self-trap exciton and peak approximately at 650 nm credited to non-bridging oxygen hole center (NBOHC) (Zhong et al., 2020) (Chen et al., 2021) (Schreiber et al., 2005) (Zhou et al., 2014b).

Figure 6.13 suggests the presence of significant chemical defects before plasma processing. There is a reduction in chemical defects amplitude with a depth of material removal. Interestingly, about 10000 counts of fluorescence amplitude are still present after the removal of 250 nm depth of material as quantified by SIMS analysis. It suggests that there is a presence of absorbing centers in the form of ODC, which extends beyond 250 nm, as stated by Zoong et al.(Zhong et al., 2020). The amplitude of ODC became flat after removing approximately 350 nm of material. There was no significant change in ODC amplitude after 450 nm depth of material removal, as shown in Fig. 6.13.

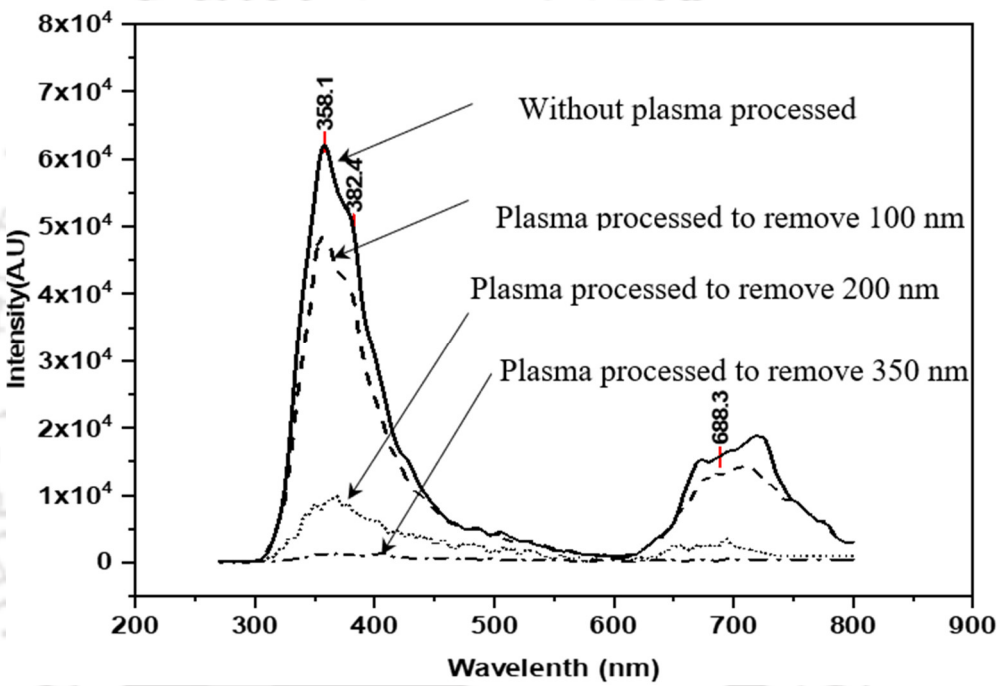

Fig. 6.13: Overlay of Fluorescence spectra of different depth removed plasma processed samples

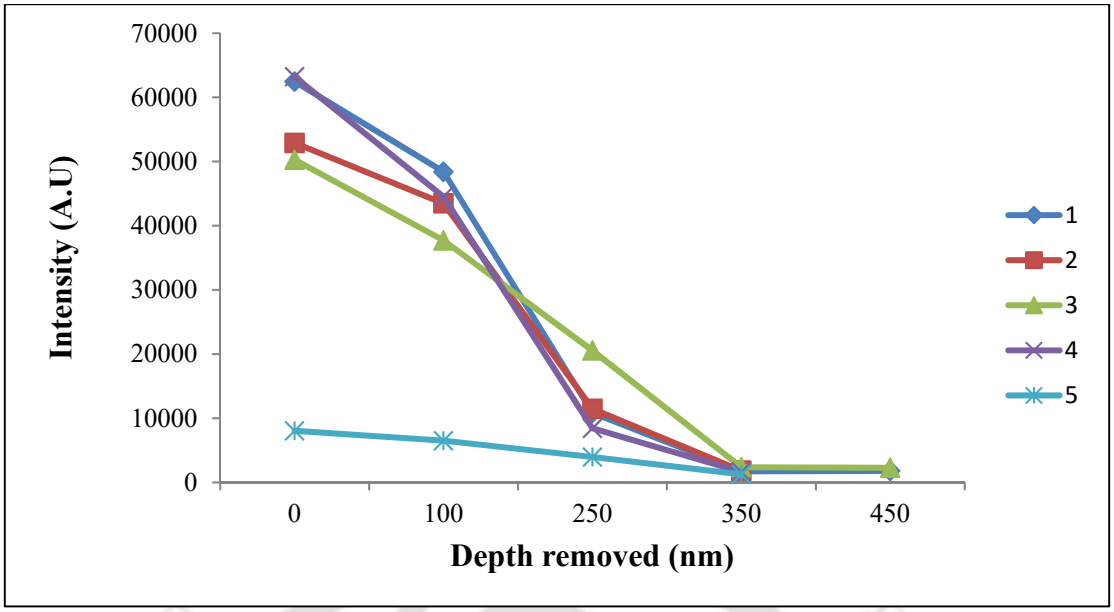

Fig. 6.14: Comparison of ODC spectra with depth removal of various samples

Figure 6.13 shows the change in counts of ODC with a depth of material removal for multiple instances. The ODC amplitude reduces with material removal depths. The fluorescence amplitude remains the same after 350 nm material removal for five different samples. Hence, a fluorescence spectrometer optimized the material removal depth to 350 nm.

6.5.6 Optimization of the process to remove 350 nm depth of material

Section 6.5.1 process was established for removing 200 to 250 nm depth of material. The fluorescence analysis confirms the presence of chemical defects till 350 nm. Hence, it is essential to optimize plasma processing to remove 350 nm of the depth of material. Figure 6.15 shows the optimized process flow for removing 250 nm depth of material and the modified process to eliminate another 100 nm depth of material. In the modified method, 50% concentration. The HCl leaching process was introduced to remove the metallic impurities, followed by a mandatory degassing cycle before plasma processing for removing 150 nm depth of material. The process was optimized primarily to remove the material without affecting surface quality.

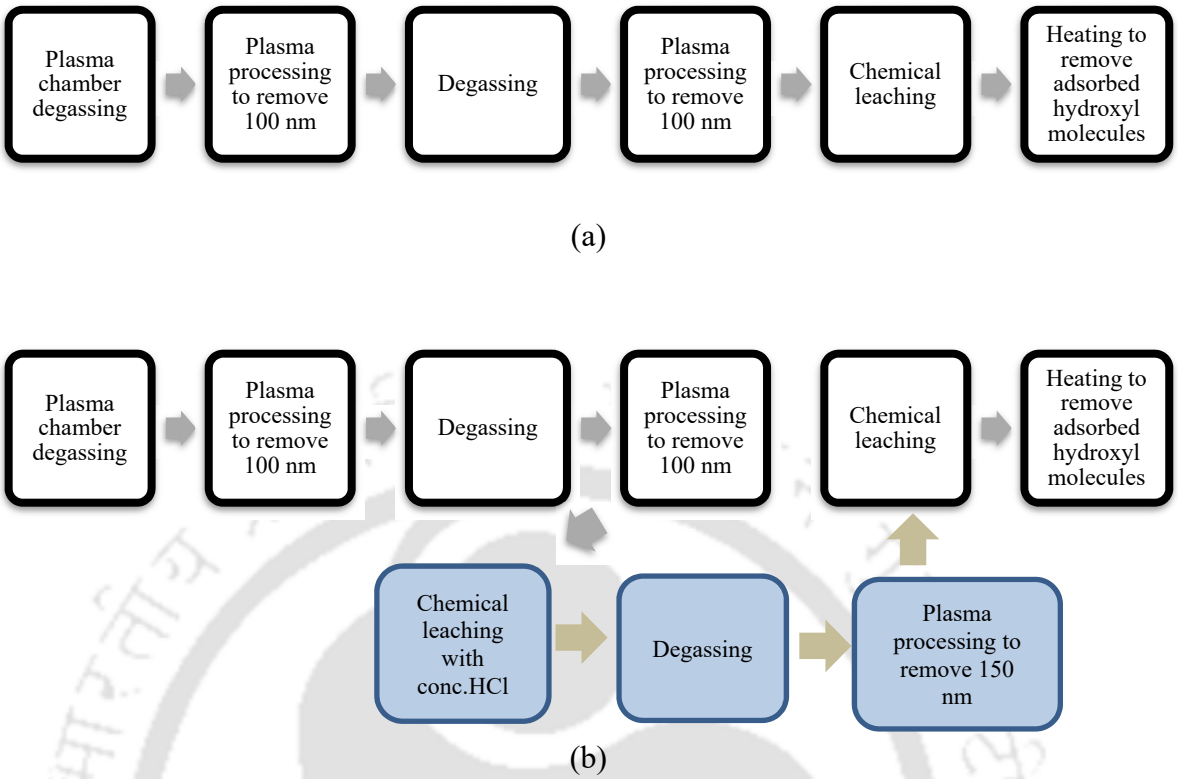

Fig. 6.15: Process flow of plasma processing (a) 250 nm and (b) 350 nm depth of material removal

6.5.7 Surface finish analysis before and after processing

The surface finish of the sample is an essential criterion for the performance of the Gyro device. Hence, this study utilizes the non-contact optical 3D surface profiler to investigate the substrate's surface roughness before and after 350 nm depth of material removal. Figure 6.15 The change in surface finish with a depth of material removal for various samples shows the piece's surface image and profile plot before and after plasma processing. A 50% surface finish (Sa) increase is observed after plasma processing. It suggests that the profile peaks were removed preferentially compared to valleys during the plasma process. Interestingly, the surface roughness Ra reduced significantly and achieved a sub-angstrom unit surface roughness. The surface finish improvement indicates the complete removal of subsurface cracks.

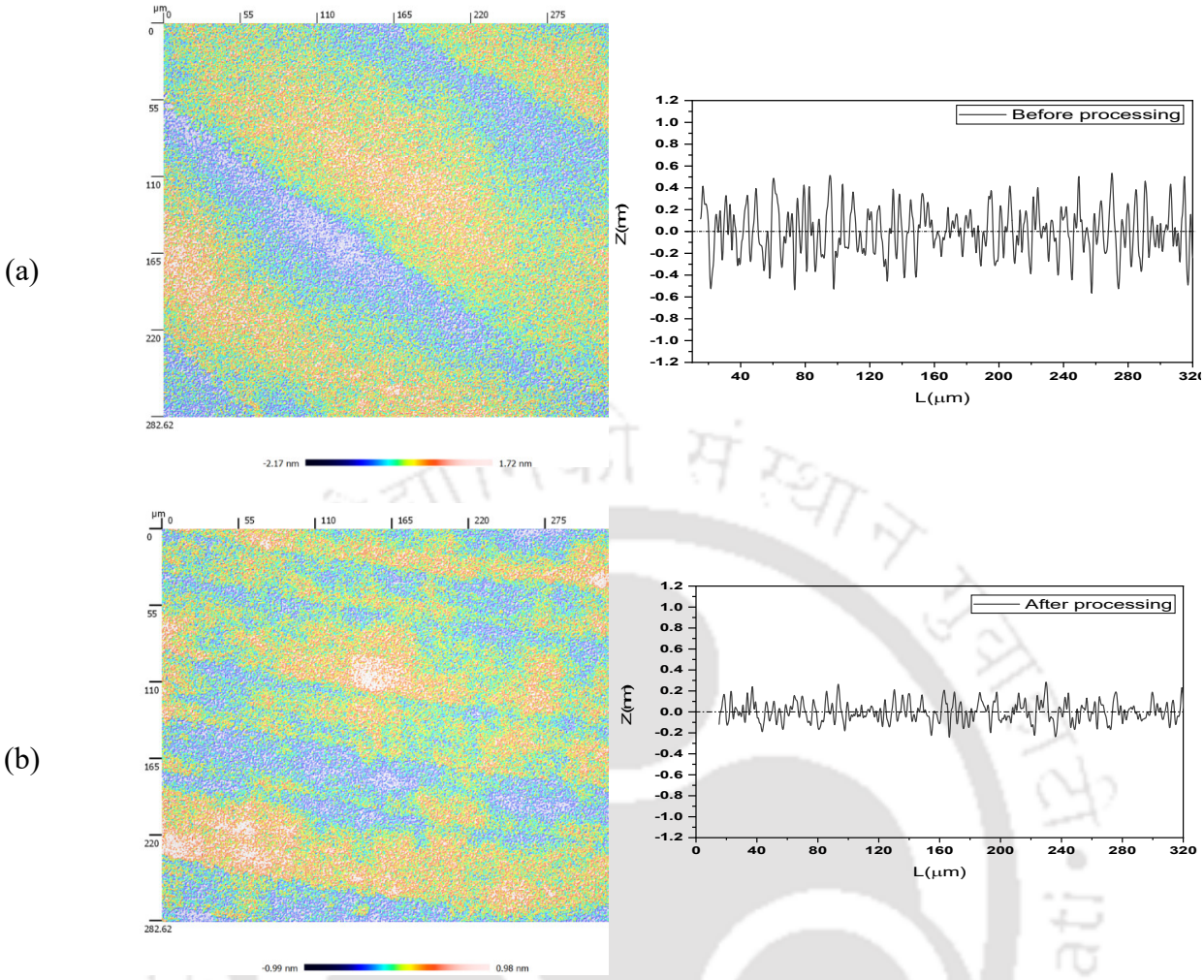

Fig. 6.16: (i) Surface and (ii) profile plots (a) before (Sa: 0.3 nm and Ra: 0.15 nm) (b) after (Sa:0.16nm, Ra: 0.06) plasma processing

6.5.8 PSD analysis

The utility of PSD is that it contains statistical information that is unbiased by the particular scan size and pixel resolution chosen by the researcher. The PSD of a surface is a mathematical tool that decomposes a surface into contributions from different spatial wavelengths or spatial frequencies (Duparré et al., 2002). Mathematically, PSD is the Fourier transform of the autocorrelation function of the signal, which contains just the power (height/depth) across a range of wave vectors. This allows the identification of the spatial wavelengths present in the signal. Higher spatial wave lengths represent shape or optical figure (deviation of the surface from the desired shape). Lower spatial wavelengths represent the roughness of the character. The PSD increases from low to high spatial wavelengths for most isotropic surfaces. How it increases depends on the process by which the surface is made.

Figure 6.17 shows the power spectral density plot of precession fused silica optics before and after the depth of material removal. The PSD for both samples increases from low to high spatial wavelengths, indicating the sample's isotropic. However, about an 80% reduction in low-frequency amplitude (nm^2) was observed after plasma processing at 350 nm depth of material removal. It suggests that, as indicated by surface finish analysis, there is an improvement in surface topography after plasma processing.

Figure 6.18 shows the PSD overlay plot after each processing step. It indicates that the PSD value is constantly reduced with a depth of removal material. The plot suggested an overall reduction in spatial frequency amplitudes with plasma processing. The plasma processing reduces the surface finish and improves the surface figure.

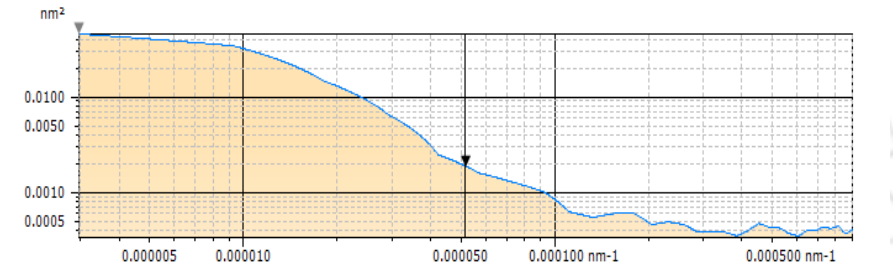

Information	
Zoom factor	x2
Smoothing	3
Number of angular profiles	180
Windows function	Hanning

Maximum amplitude of 0.04 nm2

Parameters	Value	Unit
Spatial frequency	5.17426e-05	nm-1
Amplitude	0.00184742	nm²
Dominant spatial frequency	2.96254e-06	nm-1
Maximum amplitude	0.0450992	nm²

(a)

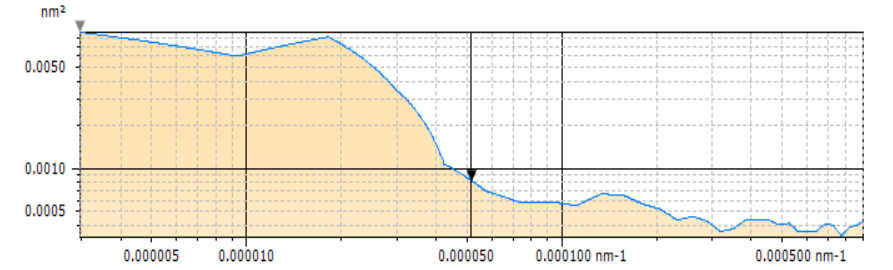

Information	
Zoom factor	x2
Smoothing	None
Number of angular profiles	180
Windows function	Hanning

Maximum amplitude: 0.008 nm2

Parameters	Value	Unit
Spatial frequency	5.17426e-05	nm-1
Amplitude	0.000804875	nm²
Dominant spatial frequency	2.96254e-06	nm-1
Maximum amplitude	0.00876384	nm²

(b)

Fig. 6.16: PSD plot of (a) before (b) after plasma processing

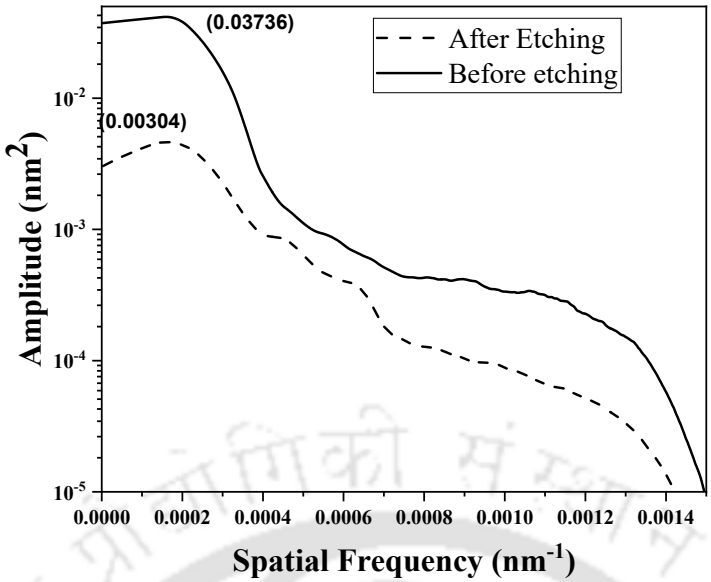

Fig. 6.18: Layout of PSD plot with different processing

6.6 Summary

This chapter described the criticality of precession-finished TIR prisms. This study elaborated on the various methods to characterize the nanometer range defect layers. Secondary ion mass spectroscopy (SIMS) successfully quantified the Beilby layer of the precession fused silica prism by indicating the presence of impurities at a depth of the substrate. It quantified the depth of damage of the precession optics as approximately 200 to 250 nm. Hence, the methodology removes this damaged layer without affecting the precession TIR prism's surface quality and functionality. This methodology includes optimizing plasma processing for removing damaged layers and introducing a chemical leaching process to dissolve foreign metallic impurities. Various experimental trials arrived at a method for mitigating the subsurface damage without affecting the surface topography. Non-destructive fluorescence analysis revealed the presence of oxygen deficiency centers (ODC). These chemical defects are primarily responsible for laser transmission loss of precession fused silica substrate during device operation. Therefore, the depth of removal is optimized using a fluorescence spectrometer. This study suggested that plasma processing significantly removed these luminescence defects after 350 nm depth of removal. Hence, the process is optimized for eliminating 350 nm depth using plasma processing without affecting the surface figure. The surface topography after plasma processing was analyzed using a 3D non-contact surface profiler.

Interestingly, surface quality improved after plasma processing, and the power spectral density (PSD) plot also validated the results. Plasma processing considerably

reduces the amplitude spatial frequency. Hence, this study successfully mitigated the mechanical, structural, and chemical defects without affecting the surface finish. Moreover, there is an improvement in surface figures observed after plasma processing.

Chapter 7

Wet chemical etching Vs. plasma processing

7.1 Introduction

Chapter 5 describes optimizing rotary ultrasonic machining (RUM) parameters for brittle fused silica substrate machining. This optimization process results in a 50% reduction in damage layers. But damaged layers formed on the substrate due to mechanical machining (Dev et al., 2016). Chemical etching is the only known method for removing machine-induced damage (Shu, 2019; Suratwala et al., 2015). The HF-based chemical etching process produces higher surface roughness due to a higher etch rate. Hence, buffer HF solution is preferred for the chemical etching process to remove defect layers and achieve a uniform etch rate (Feit et al., 2009; Knotter, 2000; Michael J. Parent, Oakdale, MN (US); Patricia M. Savu, Maplewood, MN (US); Richard M. Flynn, Mahtomedi, 2007; Stevic, 2018).

These damaged layers were eliminated successfully using a buffered HF solution, as mentioned in Chapter 5 of Section 5.11.2. But chemical etching increases surface roughness and deposition of unwanted foreign substrates. Hence, in this chapter, a comparison study was carried out with a fused silica substrate coupon, where damaged material layers were removed using wet chemical etching and dry gases etching processes at constant material removal rates (MRR). The wet chemical etching process consists of buffered Hydrofluoric acid, and the plasma process utilizes helium, oxygen, and sulfur hexafluoride gases at 96.25%, 1.25, and 2.5%, respectively.

7.2 Optimization of buffered HF solution

Among the various HF etching processes, the buffered HF etching process with NH_4F solution provides a better surface quality. As per Chapter 2, plasma processing occurs with an MRR of 0.02 mm^3/min at 40 W of the 40.68 MHz radiofrequency (RF) generator. Hence, optimizing the buffered HF etching process is essential to achieve the 0.02 mm^3/min as of the plasma process. Experiments were carried out on the fused silica sample of dimension 10 mm×10 mm×3 mm (L×B×T). The MRR of the piece after Etching was computed using the gravimetric method. The procedure for the etching process is described in the flow diagram as per Fig. 7.1.

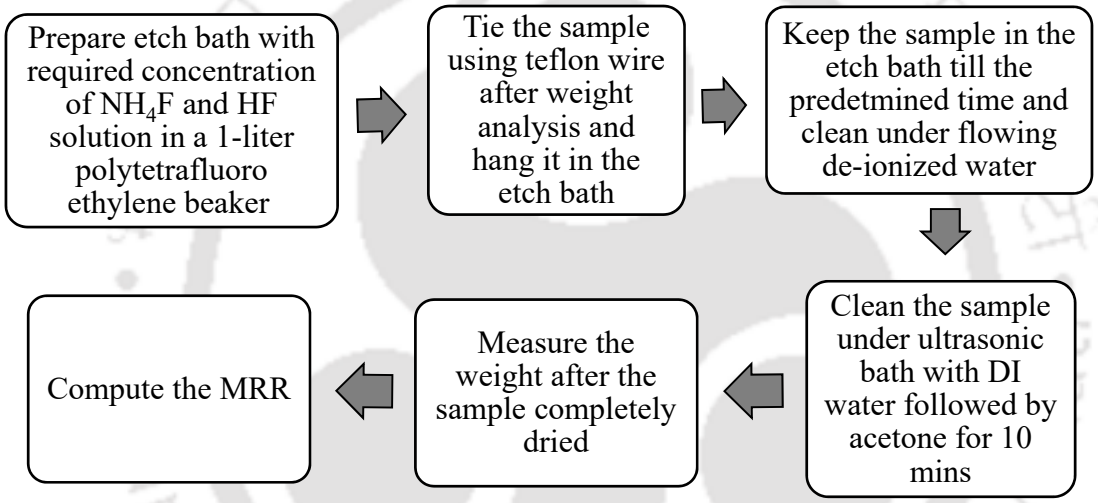

Fig.7.1: Flow diagram of an etching process

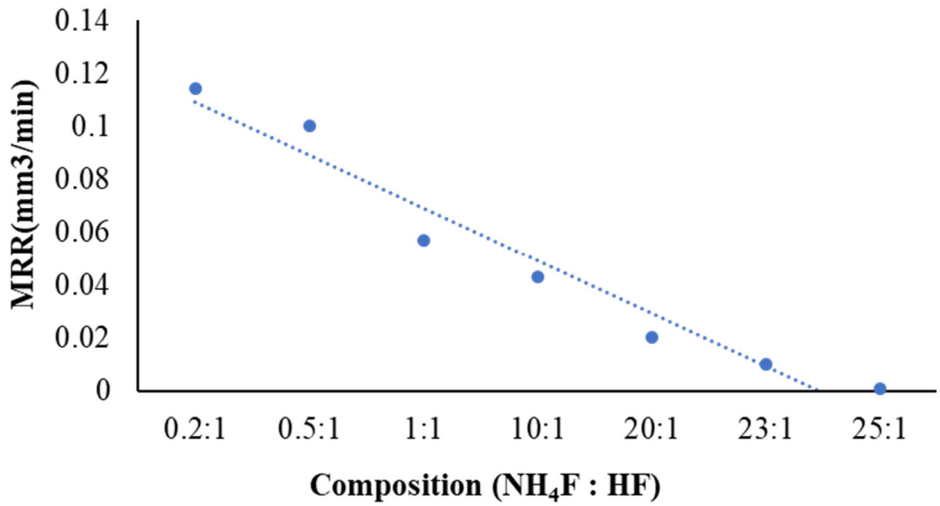

Fig. 7.2: MRR in mm^3/min with different concentrations of buffered HF solution

At least three samples were etched for each concentration of the buffered HF solution, and the average MMR was plotted. Figure 7.2 shows the resultant MRR in mm^3/min with different concentrations of buffered HF with NH_4F solution. MRR drops linearly with a decrease in the concentration of HF solution. Composition 20:1 provides the MRR of 0.02 mm^3/min as of plasma processing. Hence, 20:1 buffered HF with NH_4F solution was used for further comparative study.

7.3 Comparison of plasma etching process vs. buffered HF etching

Typically, a mechanically machined sample yields a surface finish of 0.1 microns. Hence, this study utilizes a 0.1 µm machined piece to evaluate both processes' substrate surface quality. This experiment evaluates the surface quality of the sample after removing the material of one µm, five µm, and ten µm with the plasma etching and wet chemical etching process. After processing, the surface finish of the samples was analyzed using Sensofar make 3D optical profiler. Surface and subsurface defects were evaluated using confocal Raman microscopy.

7.4 Evaluation of surface finish

The surface finish of the samples before and after processing was analyzed with the help of the confocal mode of the 3D optical profiler. Figure 7.3 shows the comparison of surface roughness value Sa for plasma etched and buffer HF etched prisms by removing one µm, five µm, and ten µm depth of material.

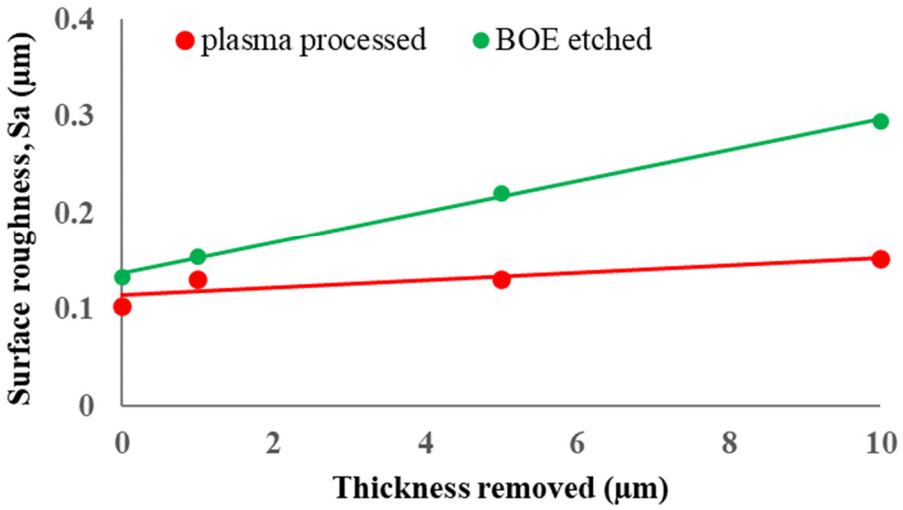

Fig. 7.3: Comparison of surface roughness value Sa for plasma etched and buffer HF etched process with a depth of removal

Figure 7.3 suggests surface roughness increases with removal depth for buffered HF solution. A 150% increase in surface roughness was observed for wet chemical etching samples. At the same time, there was an increase in only 50% surface roughness for the plasma-processed instance. The increase in surface roughness for the wet chemical etching process may be attributed to the rise in crack size due to isotropic machining of chemical etching. Plasma processing reduces the peaks preferentially compared to valleys. Due to higher collision density at peaks, there is an increase in chemical kinetics at peaks. Hence, peak to valley difference is lower compared to chemical etching.

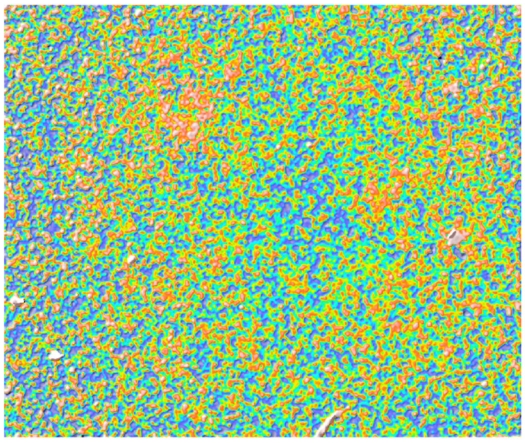

Scan area: 0.85 × 0.7 mm, Sa =0.13

(a)

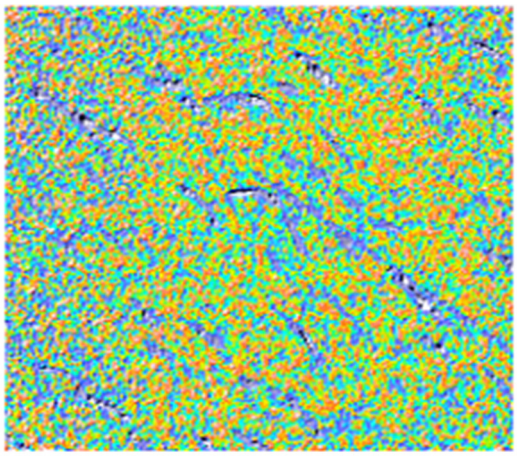

Scan area: 0.85 × 0.7 mm, Sa =0.16

(b)

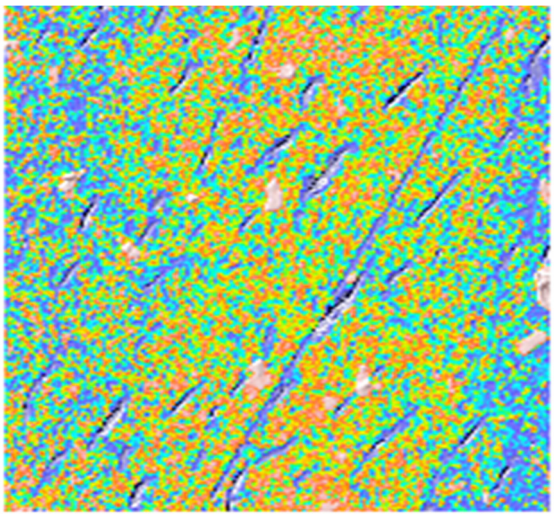

Scan area: 0.85 × 0.7 mm, Sa =0.22

(c)

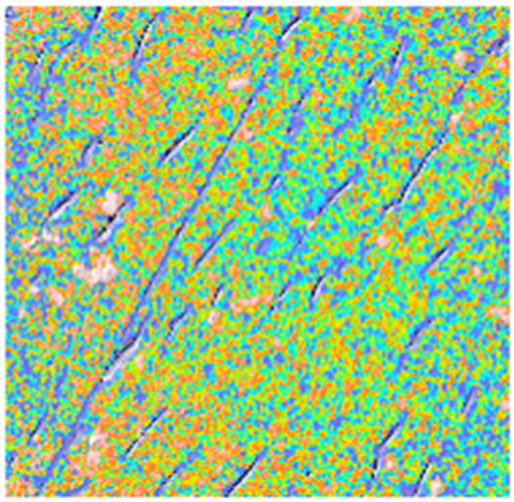

Scan area: 0.85 × 0.7 mm, Sa =0.30

(d)

Fig. 7.4: Surface profiler images of chemical etching (a) before etching, (b) after 1 µm removal, (c) after 5 µm removal, (d) after 10 µm removal

Figure 7.4 shows the surface profiler images of the samples before processing, after the removal of 1 µm, after the removal of 5 µm, and after the removal of 10 µm depth using the HF buffer etching method. Surface profiler images confirm that with the removal of the sample, depth causes a rise in crack size, so an increase in surface roughness.

Figure 7.5 shows the profiler images of the samples before processing, after the removal of 1 µm, after the removal of 5 µm, and after the removal of 10 µm depth using plasma processing. There is less change in crack size with removal in material depth.

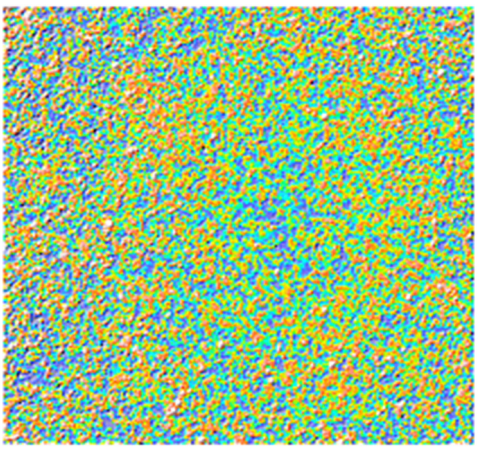

Scan area: 0.85 × 0.7 mm, Sa =0.1

(a)

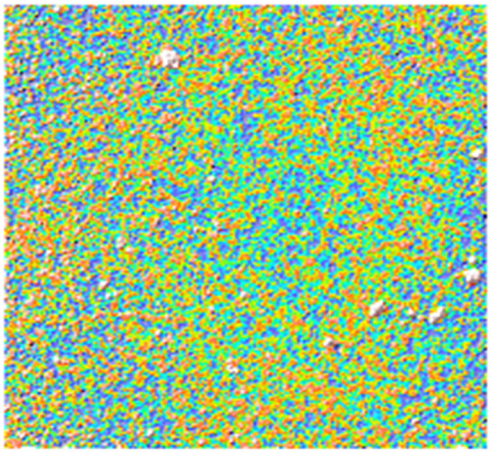

Scan area: 0.85 × 0.7 mm, Sa =0.13

(b)

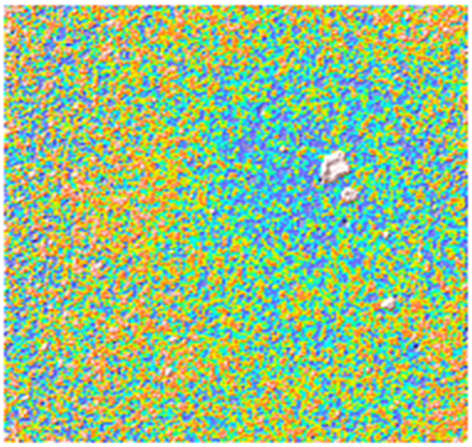

Scan area: 0.85 × 0.7 mm, Sa =0.13

(c)

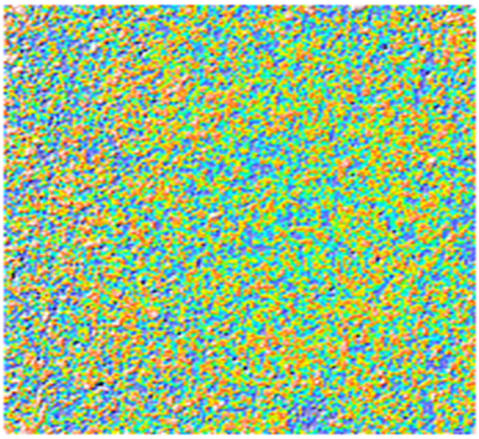

Scan area: 0.85 × 0.7 mm, Sa =0.15

(d)

Fig. 7.5: Surface profiler images of plasma processed (a) before processing, (b) after 1 µm removal, (c) after 5 µm removal, (d) after 10 µm removal

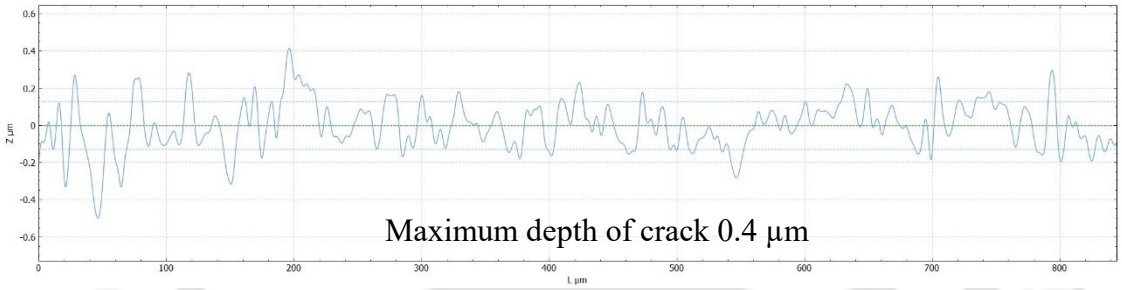

(a)

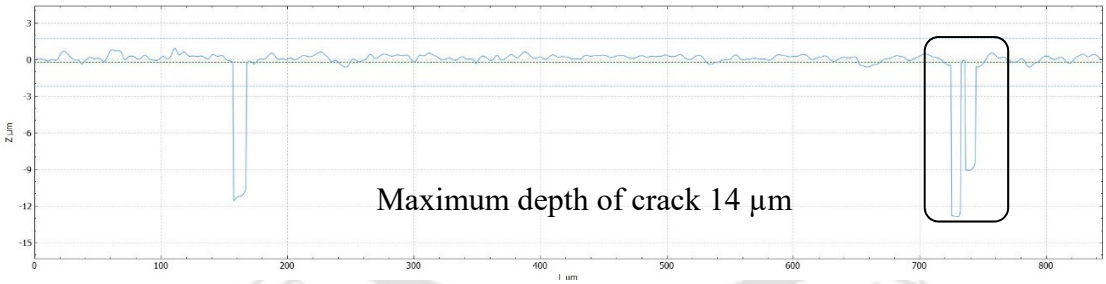

(b)

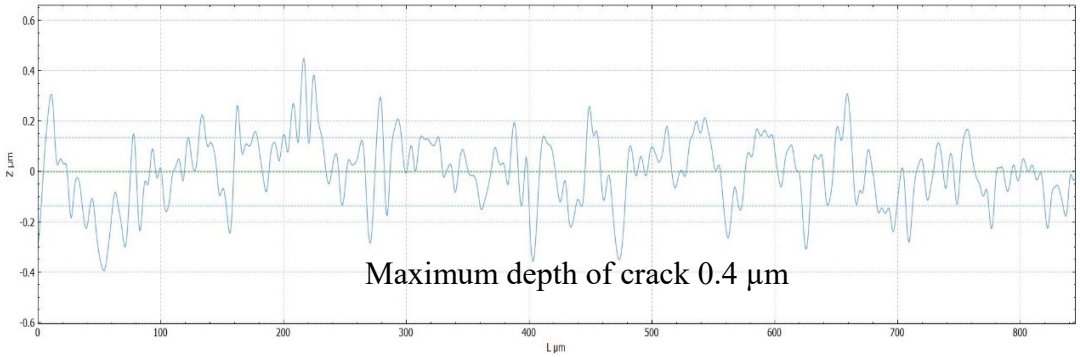

(c)

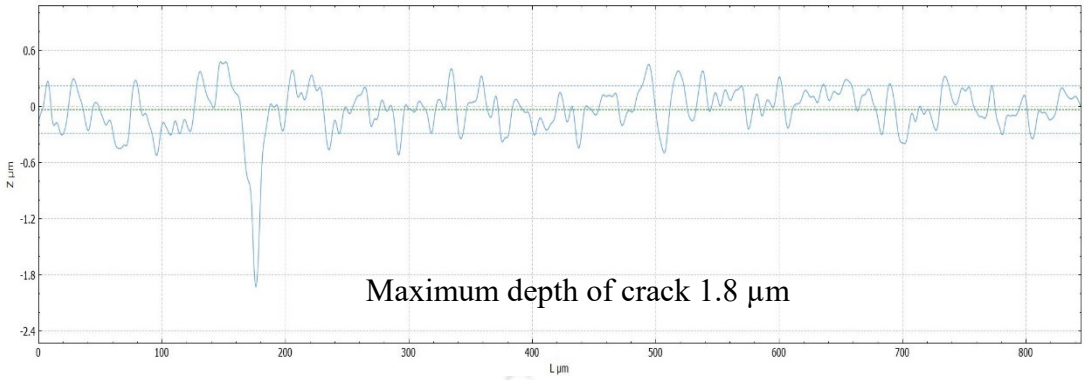

(d)

Fig. 7.6: Surface profiler of (a) before etching, (b) after 10 µm removal by etching, (c) before plasma processing, (d) after 10 µm removal by plasma processing

The Fig. 7.6 shows the comparision surface profile for the etching and plasma processing processes after 10 µm removal with identical MRR. The depth of crack increases with etching process, thus, 150% increase in surface roughness after etching process. Where as there was marginal increase in crack depth after plasma processing, the results confirmed by only 50% increase in surface roughness value.

7.5 Investigation of surface chemical defects

Chemical defects were analyzed using confocal Raman microscopy as per Chapter 5. The relative intensity ratio of 440 cm^{-1} six-membered amplitude compared to 490 cm-1 four-membered ring with a depth of removal was plotted in Fig.7.7. It shows that relative intensity increases with removal depth for both processes. It suggests that both processes are effective for removing damaged layers.

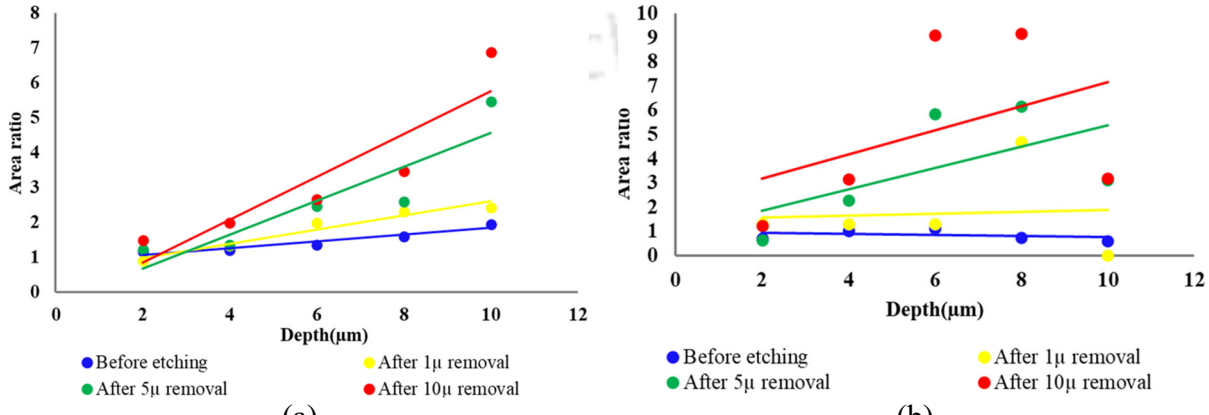

(a) (b)

Fig. 7.7: Relative intensity ratio of 440 cm-1 six-membered amplitude compared to 490 cm^{-1} four-membered ring with a depth of removal (a) plasma (b) chemical etching process

7.6 Evaluation of etch rate

The etch rate of the sample was analyzed using the gravimetric method. Table 7.1 shows the plasma and chemical etching processes etch rate during material removal depths. Etch rate reduces significantly for chemical-etched prism by removing material depth and period of operation. Primarily, it may be due to the redeposition of etched materials on the surface. These redeposition layers obstruct the etchant from reacting with a fresh surface. Secondly, chemical defect concentration also reduces with time, as indicated by confocal Raman microscopy, which reduces the chemical kinetics of the substrate. In the case of plasma processing, there is also a marginal reduction in MRR observed, which is attributed to the reduction in chemical defect concentration of the substrate with the removal of material depth. But in a plasma flow system, the by-product is gaseous, which can be removed from the system with the help of an in-situ pumping mechanism without redeposition onto the surface. To have a comparative study with plasma processing, ten µm depth removal was done with higher HF concentration during the chemical etching process.

Table 7.1: MRR in mm^3/mm during plasma and chemical etching process

	MRR (mm^3/min)		
	After 1µ removal	After 5µ removal	After 10µ removal
Plasma processed	0.02	0.019	0.015
Chemically etched	0.03	0.01	0.005
	0.03	0.01	0.02 (with 10:1)

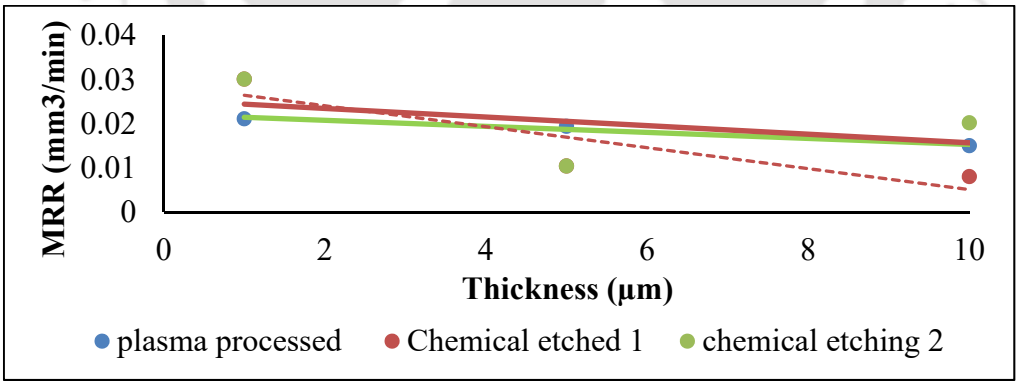

Fig. 7.8: Surface profiler images of plasma processed (a) before processing, (b) after 1 µm removal, (c) after 5 µm removal, (d) after 10 µm removal

The Fig. 7.8 shows the MRR comparision of plasma and etching processing. The material removal rate decreases with time during etching process due to deposition layers, the

formation of deposition confirmed by surface image captured by confocal mode of 3D profiler.

7.7 Surface energy enhancement using plasma processing

The surface energy of the samples before and after both processes were analyzed using by Sessile drop method using a tensiometer. Table 7.2 shows the pieces' surface energy and contact angle before and after processing. The contact angle of the sample before processing is high and has less surface energy. It may be due to the presence of low-energy organic contaminations. A decrease in contact angle and a 26% increase in surface energy were observed for the piece etched with the plasma process. Plasma processing removes the low-energy organic contaminations deposited during fabrication. On the other hand, there is no change in the surface energy of the sample noticed after wet etching processing. It may be due to the redeposition of contaminations during the wet etching process.

Table 7.2: Contact angle and surface energy of the samples before and after processing

Sample used	Contact angle	Surface energy (Nm^{-1})
Unetched sample	86.89	50.87
plasma etched sample after 10 µremoval	50.42	63.78
Chemical-etched sample after 10 µ removal	84.42	51.74

Figure 7.9 shows the contact angle images of unetched, wet chemical etched, and plasma etched pieces during tensiometer analysis. This suggests the plasma-processed sample shows better wettability than the chemically etched substrate. Hence, the plasma process provides better coating adhesion than the chemically etched process.

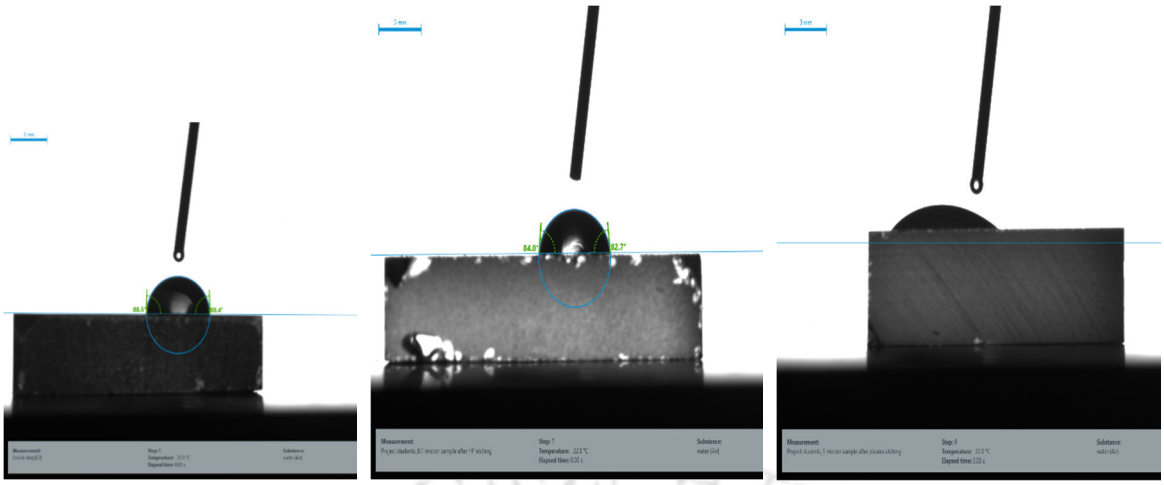

(a) (b) (c)

Fig. 7.9: Contact angle images of (a) unetched, (b) wet chemical etched, and (c) plasma etched

7.8 Summary

This chapter brought out the comparison of plasma etching versus the wet chemical etching process. The material removal rate of both processes was maintained constant for better comparison. This study used buffered HF with NH_4F solution as a wet chemical etching. The MRR of the buffered HF solution with various concentrations was derived experimentally. Concentration of 20:1 buffered HF provides the MRR of 0.02 mm^3/min matched with plasma etching. The three sets of samples, with an initial surface finish of 0.1 µm, were etched using both processes with constant MRR for 1 µm, 5 µm, and 10 µm depth of material removal. There is about a 300% increase in surface roughness and a 50% reduction in MRR observed during chemical etching. This is due to the redeposition of etched layers with time on the surface; these layers reduce the etch rate with time and increase the surface roughness. Only a 50% change in surface roughness was observed after plasma etching, and MRR also remained constant during the process. Etching with the gas phase effectively removes by-products during the process without any redeposition. Chemical defect concentration reduces significantly after 10 µm depth of material. A 26% increase in surface energy is observed for the pieces processed with plasma processing, whereas no change is observed after chemical etching. This may be due to redeposition layers at the surface during wet chemical etching. Hence, the plasma etching process has advantages over the chemical etching process.

Chapter 8

Conclusions and scope for future work

8.1 Conclusions

The machining and fabrication of fused silica optics often pose challenges. The present investigation explored the limitations of machining and fabrication of fused silica-made optical material, quantifying the damage induced by conventional machining and mitigation methodologies to achieve surface integrity of the precision optical components.

The physical action of conventional machining processes induces surface and sub-surface damage to the brittle fused silica optics. The presence of defects on the critical optics can significantly reduce the device's helpful performance. Hence, it is essential to understand the defects and quantify the depth of the damage. In this study, confocal Raman microscopy is effectively used for quantifying the depth of damage of the precision ground optics and their characteristics.

This study also includes designing and developing a medium-pressure plasma flow system. It can polish free-form optics uniformly with higher material removal rate (MRR) compared to earlier studied confined systems. The plasma processing with medium pressure region contains the energy advantages of a low-pressure plasma system and chemical reactivity as atmospheric plasma processing. Hence, the entire free-form substrate can be polished simultaneously and uniformly without any precision mechanisms. The medium pressure plasma processing utilizes a chemical reaction of reactive gases with the substrates, so the surface topography improves after plasma processing, unlike low-pressure plasma processing.

This medium-pressure plasma processing (MPPP) technique effectively mitigates damages due to physical contact machining without inducing any further damage to the

optical substrate. The MPPP technique was a vital replacement for hazardous hydrofluoric acid etching and the final finishing of the ultra-smooth precision optics. This chapter describes the significant conclusions of the study.

8.1.1 Development of medium-pressure plasma flow system

- Medium pressure plasma flow system designed and developed in-house and plasma parameters like flow rate, operating power, time of operation, and gas composition optimized for polishing of fused silica optical components size up to 40 mm.
- The comparative study raveled that the plasma flow system can be used for long machining times (> 60 mins) without any change in MRR. Moreover, the plasma flow system has a 300% higher material removal rate than the earlier studied confined system.
- There is improvement in surface topography and surface chemistry noticed post-plasma processing with a plasma flow system.

8.1.2 Prediction of in-situ material removal rate

- It is essential to understand the MRR during machining otherwise, there will be a deviation in end-product performance. Predicting the MRR during plasma processing without opening the plasma chamber is also a prerequisite. This study developed a non-invasive methodology using an optical emission spectrometer for predicting MRR in situ during the polishing operation.
- Silicon ions generated during plasma processing act as in-situ probe gases for predicting material removal rate. Hence, this methodology is accurate and independent of external parameters like pressure, power and flow rate, etc.

8.1.3 Simulation of plasma process

- The Comsol® simulation study was carried out to optimize plasma chamber configuration. The custom-made chamber with a V-shaped groove has shown uniform reactive radical distribution for polishing free-form optics.
- The simulation was validated by experimental analysis of the entire chamber's plasma temperature and electron density using an optical emission spectrometer.

8.1.4 Quantification of stressed layer depth at fused silica substrate

- The depth of the damage of the ground fused silica was quantified using Confocal Raman microscopy.
- This methodology was adopted for optimizing the rotary ultrasonic machining parameters for shaping fused silica hemispherical resonator shells (HRG).
- The full-width half maximum (FWHM) methodology was developed for quantifying the depth damage due to plastic deformation of the ground HRG shell.
- The FWHM methodology was verified by accessing the Q factor of the resonator shell using laser Doppler vibrometry (LDV).
- There is a quantum jump in the Q factor was observed after removing the damaged depth.

8.1.5 Quantification and mitigation of defect layers of the ultrafine total reflecting prism

- The Plausible mechanism of Ring Laser Gyroscope device failure was analyzed and verified using a photoluminescence spectrometer.
- The SSD depth at the nanometer scale was quantified for the ultra-smooth prism substrate using Secondary Ion Mass Spectrometer (SIMS).
- The plasma processing followed by chemical leaching was established to enhance the surface integrity of the prism substrate.
- The post-processing prism has shown promising results where Ce atoms concentration is reduced completely.
- The structural defects and chemical impurities were removed from the prism substrate by plasma polishing followed by chemical leaching.
- A fluorescence spectrometer was introduced for investigating chemical defects such as absorbing color centers.
- The depth of damage of the precession fused silica sample was quantified using a fluorescence spectrometer.
- Process flow was established for removing 350 nm depth of material for the ultra-fine fused silica substrate without affecting the surface finish.
- The surface finish and Power Spectral Density of the precession substrate before and after processing were analyzed using the 3D profiler.

- There is an improvement in surface finish observed after plasma processing, which confirms the complete removal of structural defects.
- The fluorescence analysis confirms the removal of chemical defects after 350 nm depth of material removal.
- There is a significant reduction in spatial frequency amplitude observed after plasma processing.

8.1.6 Etching Vs. plasma processing

- This chapter brought out the comparison of plasma etching versus the wet chemical etching process.
- The MRR of the buffered HF solution with various concentrations was derived experimentally. 20:1 concentration of buffered HF provides the MRR of 0.02 mm^3/min matched with plasma etching.
- There is about a 300% increase in surface roughness and a 50% reduction in MRR observed during chemical etching. This is due to the redeposition of etched layers with time on the surface; these layers reduce the etch rate with time and increase the surface roughness.
- Only a 50% change in surface roughness was observed after plasma etching, and MRR also remained constant during the process. Etching with the gas phase effectively removes by-products during the process without any redeposition.
- Chemical defect concentration reduces significantly after 10 μm depth of material.
- A 26% increase in surface energy is observed for the pieces processed with plasma processing, whereas no change is observed after chemical etching. This may be due to redeposition layers at the surface during wet chemical etching. Hence, the plasma etching process has advantages over the chemical etching process.

8.2 Scope for further work

- The present study successfully demonstrated the damage-free nano-polishing of ultrasmooth fused silica optics. A Fluorescence spectroscopy study shows the reduction in photo-absorptive color centers after plasma processing. however, the damage threshold value rates the quality of the optics. Thus, the Laser damage

threshold will be evaluated for the optics after plasma polishing to compare with the international standard.

- In this study, Comsol® simulation was used for modeling the plasma simulation. This simulation study cannot simulate the chemical interaction of reactive radicals with the substrate surface. So, comprehensive molecular modeling should be used to simulate plasma interactions effectively.
- The depth of damage was quantitatively analyzed by Confocal Raman spectroscopy. However, this study failed to quantify the plastic deformation of machine-induced stresses. The calibration study will use a diamond anvil cell and nano-indentor to correlate the six-membered peak width with the plastic strain.
- This study has shown the advantages of the plasma process over the chemical wet etching process. Hence, the freeform devices will be plasma processed after mechanical operation to remove damaged layers. It helps in the reduction of the cost-intensive polishing process.

References

1) Avadhesh Kumar Yadav a and PS. A Review of Structure of Oxide Glasses by Raman Spectroscopy. This J Is © NanoGe J Energy Sustain 2012:11002–3. https://doi.org/10.1039/c0xx00000x.

2) Bauch J, Brechbühl J, Ullrich HJ, Meinl G, Lin H, Kebede W. Innovative analysis of X-ray microdiffraction images on selected applications of the Kossel technique. Cryst Res Technol 1999;34:71–88. https://doi.org/10.1002/(SICI)1521-4079(199901)34:1<71::AID-CRAT71>3.0.CO;2-6.

3) Blaineau P, Laheurte R, Darnis P, Darbois N, Cahuc O, Neauport J. Relations between subsurface damage depth and surface roughness of grinded fused silica. Opt Express 2013;21:30433. https://doi.org/10.1364/OE.21.030433.

4) Bo Zheng, Saratoga, CA (US); Mei Chang, Saratoga, CA (US); Arvind Sundarrajan, San Jose C (US). METHODS OF END POINT DETECTION FOR SUBSTRATE FABRICATION PROCESSES. US 8,747,686 B2, 2014.

5) Boudam MK, Moisan M, Saoudi B, Popovici C, Gherardi N, Massines F. Bacterial spore inactivation by atmospheric-pressure plasmas in the presence or absence of UV photons as obtained with the same gas mixture. J Phys D Appl Phys 2006;39:3494–507. https://doi.org/10.1088/0022-3727/39/16/S07.

6) Brugeat S, Coitout H. Determination of electron density in a wall stabilized Ar-CO ${\mathsf{_2}}$ thermal plasma. Eur Phys J D - At Mol Opt Phys 2004;28:101–7. https://doi.org/10.1140/epjd/e2003-00290-6.

7) Carlson JD, Catanzarite DM, St. Clair KA. COMMERCIAL MAGNETO-RHEOLOGICAL FLUID DEVICES. Int J Mod Phys B 1996;10:2857–65. https://doi.org/10.1142/S0217979296001306.

8) Chen Q, Wang H, Dai R, Wang Z, Tao X, Zhao W, et al. Correlation between Photoluminescence Properties of Surface Defects and Laser-Induced Damage Threshold of Fused Silica. Laser Part Beams 2021;2021. https://doi.org/10.1155/2021/5530410.

9) Coburn JW, Winters HF. Ion- and electron-assisted gas-surface chemistry - An

important effect in plasma etching. J Appl Phys 1979;50:3189–96. https://doi.org/10.1063/1.326355.

10) Crintea DL, Czarnetzki U, Iordanova S, Koleva I, Luggenhölscher D. Plasma diagnostics by optical emission spectroscopy on argon and comparison with Thomson scattering. J Phys D Appl Phys 2009;42. https://doi.org/10.1088/0022-3727/42/4/045208.

11) Desai M, Jairath R, Stell M, Tolles R. Chemical mechanical polishing for planarization in manufacturing environment. Mater Res Soc Symp - Proc 1994;337:99–104. https://doi.org/10.1557/proc-337-99.

12) Dev DSD, Krishna E, Das M. Novel Finishing Process Development for Precision Complex-Shaped Hemispherical Shell by Bulk Plasma Processing, 2018. https://doi.org/10.1007/978-981-10-8767-7_12.

13) Dev DSD, Krishna E, Das M. A novel plasma-assisted atomistic surface finishing on freeform surfaces of fused silica. Int J Precis Technol 2016;6. https://doi.org/10.1504/IJPTECH.2016.079998.

14) Duparré A, Ferre-Borrull J, Gliech S, Notni G, Steinert J, Bennett JM. Surface characterization techniques for determining the root-mean-square roughness and power spectral densities of optical components. Appl Opt 2002;41:154. https://doi.org/10.1364/ao.41.000154.

15) Feit MD, Suratwala TI, Wong LL, Steele WA, Miller PE, Bude JD. Modeling Wet Chemical Etching of Surface Flaws on Fused Silica † 2009;7504:1–13. https://doi.org/10.1117/12.836912.

16) Galeener FL, Geissberger AE. Vibrational dynamics in Si-substituted vitreous Sio2. Phys Rev B 1983;27:6199–204.

17) Gerhard C, Weihs T, Luca A, … SW-J of the E, 2013 U. Polishing of optical media by dielectric barrier discharge inert gas plasma at atmospheric pressure. J Eur Opt Soc Publ 2013;8:13081.

18) Gillman BE, Tinker F. <title>Fun facts about pitch and the pitfalls of ignorance</title>. In: Stahl HP, editor. vol. 3782, 1999, p. 72–9.

https://doi.org/10.1117/12.369240.

19) Golini D, Kordonski WI, Dumas P, Hogan SJ. <title>Magnetorheological finishing (MRF) in commercial precision optics manufacturing</title>. Opt Manuf Test III 1999;3782:80–91. https://doi.org/10.1117/12.369174.

20) Griem HR. Principles of Plasma Spectroscopy. Cambridge University Press; 1997. https://doi.org/10.1017/CBO9780511524578.

21) Guinn, Keith V. SCM. Process for device fabrication in which the plasma etch is controlled by monitoring optical emission. 5,877,032, 1999.

22) Hed PP, Edwards DF. Relationship between subsurface damage depth and surface roughness during grinding of optical glass with diamond tools. Appl Opt 1987;26:2491. https://doi.org/10.1364/AO.26.002491.

23) Jiao Y, Liu WJ, Pei ZJ, Xin XJ, Treadwell C. Study on Edge Chipping in Rotary Ultrasonic Machining of Ceramics: An Integration of Designed Experiments and Finite Element Method Analysis. J Manuf Sci Eng 2005;127:752–8. https://doi.org/10.1115/1.2034511.

24) Jin HL, Wang B, Zhang FH. Effect on surface roughness of zerodur material in atmospheric pressure plasma jet processing. 5th Int. Symp. Adv. Opt. Manuf. Test. Technol. Adv. Opt. Manuf. Technol., vol. 7655, SPIE; 2010, p. 76552X. https://doi.org/10.1117/12.866683.

25) Kano K, Suzuki M, Akatsuka H. Spectroscopic measurement of electron temperature and density in argon plasmas based on collisional-radiative model. Plasma Sources Sci Technol 2000;9. https://doi.org/10.1088/0963-0252/9/3/309.

26) Knotter DM. Etching Mechanism of Vitreous Silicon Dioxide in HF-Based Solutions 2000:4345–51.

27) Kordonski W, Jacobs S. Model of magnetorheological finishing. J Intell Mater Syst Struct 1996;7:131–7. https://doi.org/10.1177/1045389X9600700202.

28) Leistner AJ, Thwaite EG, Lesha F, Bennett JM. Polishing study using Teflon and pitch laps to produce flat and supersmooth surfaces. Appl Opt 1992;31:1472. https://doi.org/10.1364/ao.31.001472.

29) Li D, Li N, Su X, Liu K, Ji P, Wang B. Characterization of fused silica surface topography in capacitively coupled atmospheric pressure plasma processing. Appl Surf Sci 2019a;489:648–57. https://doi.org/10.1016/j.apsusc.2019.06.026.

30) Li D, Li N, Su X, Liu K, Ji P, Wang B. Characterization of fused silica surface topography in capacitively coupled atmospheric pressure plasma processing. Appl Surf Sci 2019b;489:648–57. https://doi.org/10.1016/j.apsusc.2019.06.026.

31) Li J, Zhu YW, Zuo DW, Lin K, Li M. Fixed abrasive lapping and polishing of hard brittle materials. Key Eng Mater 2010;426–427:589–92. https://doi.org/10.4028/www.scientific.net/KEM.426-427.589.

32) Li S, Wang Z, Wu Y. Relationship between subsurface damage and surface roughness of optical materials in grinding and lapping processes. J Mater Process Technol 2008;205:34–41. https://doi.org/10.1016/j.jmatprotec.2007.11.118.

33) Li X, Ling L, Hua X, Fukasawa M, Oehrlein GS, Barela M, et al. Effects of Ar and O2 additives on SiO2 etching in C4F8-based plasmas. J Vac Sci Technol A Vacuum, Surfaces, Film 2003;21:284–93. https://doi.org/10.1116/1.1531140.

34) Li Y, Wang J. Surface characteristics of an optical component manufactured with a polyurethane lap. Appl Opt 2009;48:737–42. https://doi.org/10.1364/AO.48.000737.

35) Liao D, Chen X, Tang C, Xie R, Zhang Z. Characteristics of hydrolyzed layer and contamination on fused silica induced during polishing. Ceram Int 2014;40:4479–83. https://doi.org/10.1016/j.ceramint.2013.08.121.

36) Liu F, Qian J, Wang X, Liu L, Ming H. UV irradiation-induced defect study of glasses by Raman spectroscopy. Phys Rev B - Condens Matter Mater Phys 1997;56:3066–71. https://doi.org/10.1103/PhysRevB.56.3066.

37) Liu H, He S, Wei Q, Yang D, Liu Y, Wang H, et al. A study on spectrum property of fused quartz under the influence of space charged particles with low energy. Eur Sp Agency, (Special Publ ESA SP 2003;2003:687–92.

38) Liu H, Ye X, Zhou Xinda, Huang J, Wang F, Zhou Xiaoyan, et al. Subsurface defects characterization and laser damage performance of fused silica optics during

HF-etched process. Opt Mater (Amst) 2014;36:855–60. https://doi.org/10.1016/j.optmat.2013.11.022.

39) Liu W, Wang D, Hu M, Wang Y, Liang H, Hang L. Roughness evolution of fused silica during plasma polishing processes. In: Yang L, Schoen JM, Namba Y, Li S, editors., 2009. https://doi.org/10.1117/12.831002.

40) Lodha GS, Yamashita K, Kunieda H, Tawara Y, Yu J, Namba Y, et al. Effect of surface roughness and subsurface damage on grazing-incidence x-ray scattering and specular reflectance. Appl Opt 1998;37:5239. https://doi.org/10.1364/AO.37.005239.

41) Lv D, Wang H, Zhang W, Yin Z. Subsurface damage depth and distribution in rotary ultrasonic machining and conventional grinding of glass BK7. Int J Adv Manuf Technol 2016;86:2361–71. https://doi.org/10.1007/s00170-016-8376-z.

42) Mauro JC, Zanotto ED. Two Centuries of Glass Research: Historical Trends, Current Status, and Grand Challenges for the Future. Int J Appl Glas Sci 2014;5:313–27. https://doi.org/10.1111/ijag.12087.

43) Michael J. Parent, Oakdale, MN (US); Patricia M. Savu, Maplewood, MN (US); Richard M. Flynn, Mahtomedi M (US). FLUORINATED SURFACTANTS FOR BUFFERED ACID ETCH, SOLUTIONS (75). US 7,169,323 B2, 2007.

44) Mori Y, Yamauchi K, Endo K. Elastic emission machining. Precis Eng 1987;9:123–8. https://doi.org/10.1016/0141-6359(87)90029-8.

45) Morse DL, Evenson JW. Welcome to the Glass Age. Int J Appl Glas Sci 2016;7:409–12. https://doi.org/10.1111/ijag.12242.

46) Namba, Y., Tsuwa, H., Wada R. Structure of Polishing Machine 1987;36:1–4.

47) Neauport J, Ambard C, Cormont P, Darbois N, Destribats J, Luitot C, et al. Subsurface damage measurement of ground fused silica parts by HF etching techniques. Opt Express 2009a;17:20448. https://doi.org/10.1364/OE.17.020448.

48) Neauport J, Cormont P, Legros P, Ambard C, Destribats J. Imaging subsurface damage of grinded fused silica optics by confocal fluorescence microscopy. Opt Express 2009b;17:3543. https://doi.org/10.1364/oe.17.003543.

49) Nucci J, Krämer S, Arzt E, Volkert CA. Local strains measured in Al lines during thermal cycling and electromigration using convergent-beam electron diffraction. J Mater Res 2005;20:1851–9. https://doi.org/10.1557/JMR.2005.0231.

50) Pfiffer M, Cormont P, Fargin E, Bousquet B, Dussauze M, Lambert S, et al. Effects of deep wet etching in HF/HNO_3 and KOH solutions on the laser damage resistance and surface quality of fused silica optics at 351 nm. Opt Express 2017;25:4607. https://doi.org/10.1364/OE.25.004607.

51) Piao F, Oldham WG, Haller EE. Ultraviolet-induced densification of fused silica. J Appl Phys 2000;87:3287–93. https://doi.org/10.1063/1.372338.

52) Pilla O, Fontana A, Caponi S, Rossi F, Viliani G, Gonzalez MA, et al. Vibrational dynamic of "strong" glasses: The case of v-SiO2 and v-GeO2. J Non Cryst Solids 2003;322:53–7. https://doi.org/10.1016/S0022-3093(03)00173-X.

53) Randi JA, Lambropoulos JC, Jacobs SD. Subsurface damage in some single crystalline optical materials. Appl Opt 2005;44:2241–9. https://doi.org/10.1364/AO.44.002241.

54) Salh R. Silicon Nanocluster in Silicon Dioxide: Cathodoluminescence, Energy Dispersive X-Ray Analysis and Infrared Spectroscopy Studies. Cryst Silicon - Prop Uses 2011. https://doi.org/10.5772/35404.

55) Schreiber A, Kühn B, Arnold E, Schilling FJ, Witzke HD. Radiation resistance of quartz glass for VUV discharge lamps. J Phys D Appl Phys 2005;38:3242–50. https://doi.org/10.1088/0022-3727/38/17/S28.

56) Shu Y. Study on etching process of fused silica with concentrated HF. Optik (Stuttg) 2019;178:544–9. https://doi.org/10.1016/j.ijleo.2018.10.011.

57) Steven Lee Szetsen, Hsinchu T. IN-SITU AND NON-INTRUSIVE METHOD FORMONITORNG PLASMA ETCH CHAMBER CONDITION UTILIZING SPECTROSCOPICTECHNIQUE. 6,068,783, 2000.

58) Stevic P. STANDARD OPERATING PROCEDURE 2.pdf 2018.

59) Suratwala T, Steele R, Feit MD, Wong L, Miller P, Menapace J, et al. Effect of rogue particles on the sub-surface damage of fused silica during grinding/polishing.

J Non Cryst Solids 2008;354:2023–37. https://doi.org/10.1016/j.jnoncrysol.2007.11.015.

60) Suratwala T, Steele W, Wong L, Feit MD, Miller PE, Dylla-Spears R, et al. Chemistry and Formation of the Beilby Layer During Polishing of Fused Silica Glass. J Am Ceram Soc 2015;98:2395–402. https://doi.org/10.1111/jace.13659.

61) Suratwala T, Wong L, Miller P, Feit MD, Menapace J, Steele R, et al. Sub-surface mechanical damage distributions during grinding of fused silica. J Non Cryst Solids 2006;352:5601–17. https://doi.org/10.1016/j.jnoncrysol.2006.09.012.

62) Suratwala TI, Miller PE, Bude JD, Steele WA, Shen N, Monticelli M V., et al. HF-based etching processes for improving laser damage resistance of fused silica optical surfaces. J Am Ceram Soc 2011;94:416–28. https://doi.org/10.1111/j.1551-2916.2010.04112.x.

63) Tamura N, MacDowell AA, Spolenak R, Valek BC, Bravman JC, Brown WL, et al. Scanning X-ray microdiffraction with submicrometer white beam for strain/stress and orientation mapping in thin films. J Synchrotron Radiat 2003;10:137–43. https://doi.org/10.1107/S0909049502021362.

64) Trogolo JA, Rajan K. Near surface modification of silica structure induced by chemical/mechanical polishing. J Mater Sci 1994;29:4554–8. https://doi.org/10.1007/BF00376278.

65) Trost M, Herffurth T, Schmitz D, Schröder S, Duparré A, Tünnermann A. Evaluation of subsurface damage by light scattering techniques. Appl Opt 2013;52:6579. https://doi.org/10.1364/AO.52.006579.

66) Uchida T, Hamaguchi S. Magnetic neutral loop discharge (NLD) plasmas for surface processing. J Phys D Appl Phys 2008;41. https://doi.org/10.1088/0022-3727/41/8/083001.

67) Unnikrishnan VK, Alti K, Kartha VB, Santhosh C, Gupta GP, Suri BM. Measurements of plasma temperature and electron density in laser-induced copper plasma by time-resolved spectroscopy of neutral atom and ion emissions. Pramana 2010;74:983–93. https://doi.org/10.1007/s12043-010-0089-5.

68) Wang J, Li Y, Han J, Xu Q, Guo Y. Evaluating subsurface damage in optical glasses. J Eur Opt Soc 2011;6. https://doi.org/10.2971/jeos.2011.11001.

69) Wilson SR, McNeil JR. Neutral Ion Beam Figuring Of Large Optical Surfaces. Curr. Dev. Opt. Eng. II, vol. 0818, SPIE; 1987, p. 320. https://doi.org/10.1117/12.978903.

70) Xie Y, Bhushan B. polishing 1996;200:281–95.

71) Xin Q, Li N, Wang J, Wang B, Li G, Ding F, et al. Surface roughening of ground fused silica processed by atmospheric inductively coupled plasma. Appl Surf Sci 2015;341:142–8. https://doi.org/10.1016/j.apsusc.2015.03.001.

72) Xu S, Yuan X, Zu X, Lv H, Jiang X, Zhang L, et al. Laser-induced defects in fused silica by UV laser irradiation. J Non Cryst Solids 2007;353:4212–7. https://doi.org/10.1016/j.jnoncrysol.2007.08.030.

73) Xu S, Zu X, Jiang X, Yuan X, Huang J, Wang H, et al. The damage mechanisms of fused silica irradiated by 355 nm laser in vacuum. Nucl Instruments Methods Phys Res Sect B Beam Interact with Mater Atoms 2008;266:2936–40. https://doi.org/10.1016/j.nimb.2008.03.192.

74) Yao YX, Wang B, Wang JH, Jin HL, Zhang YF, Dong S. Chemical machining of Zerodur material with atmospheric pressure plasma jet. CIRP Ann - Manuf Technol 2010;59:337–40. https://doi.org/10.1016/j.cirp.2010.03.118.

75) Ye H, Li Y, Yuan Z, Wang J, Yang W, Xu Q. Laser induced damage characteristics of fused silica optics treated by wet chemical processes. Appl Surf Sci 2015;357:498–505. https://doi.org/10.1016/j.apsusc.2015.09.065.

76) Yokota H, Kinosita K, Sakata H. Ellipsometric Study of Polished Glass Surfaces. Japanese J Appl Physics, Part 1 Regul Pap Short Notes Rev Pap 1964;3:805–6. https://doi.org/10.1143/JJAP.3.805.

77) Zhang Jufan, Wang B, Dong S. Application of atmospheric pressure plasma polishing method in machining of silicon ultra-smooth surfaces. Front Electr Electron Eng China 2008;3:480–7. https://doi.org/10.1007/s11460-008-0072-9.

78) Zhang J, Wang B, Dong S. Application of atmospheric pressure plasma polishing

method in machining of silicon ultra-smooth surfaces. Front Electr Electron Eng China 2008;3:480–487.

79) Zhang W, Shi F, Song C, Tian Y, Guo S. Study on Damage Characteristics of Fused Silica under Ion Beam Sputtering and AMP Technique. Laser Part Beams 2022;2022. https://doi.org/10.1155/2022/3740391.

80) Zheng Z, Zu X, Jiang X, Xiang X, Huang J, Zhou X, et al. Effect of HF etching on the surface quality and laser-induced damage of fused silica. Opt Laser Technol 2012;44:1039–42. https://doi.org/10.1016/j.optlastec.2011.10.013.

81) Zhong Y, Dai Y, Shi F, Song C, Tian Y, Lin Z, et al. Effects of ion beam etching on the nanoscale damage precursor evolution of fused silica. Materials (Basel) 2020;13. https://doi.org/10.3390/ma13061294.

82) Zhou M, Wang M, Dong G. Experimental Investigation on Rotary Ultrasonic Face Grinding of SiCp/Al Composites. Mater Manuf Process 2016;31:673–8. https://doi.org/10.1080/10426914.2015.1025962.

83) Zhou Xiaoyan, Zhou Xinda, Huang J, Cheng Q, Wang F, Ye X, et al. Laser-Induced Point Defects in Fused Silica Irradiated by UV Laser in Vacuum. Adv Condens Matter Phys 2014a;2014:1–7. https://doi.org/10.1155/2014/853764.

84) Zhou Xiaoyan, Zhou Xinda, Huang J, Cheng Q, Wang F, Ye X, et al. Laser-induced point defects in fused silica irradiated by UV laser in vacuum. Adv Condens Matter Phys 2014b;2014. https://doi.org/10.1155/2014/853764.

85) Zhu XM, Pu YK. Using OES to determine electron temperature and density in low-pressure nitrogen and argon plasmas. Plasma Sources Sci Technol 2008;17. https://doi.org/10.1088/0963-0252/17/2/024002.

86) Zhu XM, Pu YK, Balcon N, Boswell R. Measurement of the electron density in atmospheric-pressure low-temperature argon discharges by line-ratio method of optical emission spectroscopy. J Phys D Appl Phys 2009;42. https://doi.org/10.1088/0022-3727/42/14/142003.

Publications

Patent filed:

1. Enni Krishna, D Sam Dayala Dev, Sreelakshmi K, and Manas Das In-situ monitoring of plasma polishing process by using optical emission spectrometer, Patent no. **202041007062**, filed on 19th Feb.2020.
2. Enni Krishna, D Sam Dayala Dev, Sreelakshmi K, Jagroop and Manas Das " Surface integrity improvement of ultrasmooth fused silica optics" Application no. **202341045697**, filed on 7th July 23.

Papers published in Journals:

1. Hari Narayan Singh Yadav, Enni Krishna, Sreelakshmy Kombath, D Sam Dayala Dev & Manas Das (2023): Investigation of MRR and surface characterization using plasma process, Materials and Manufacturing Processes, DOI:10.1080/10426914.2023.2176873.
2. D Sam Dayala Dev, Enni Krishna, Manas Das, Development of a non-contact plasma processing technique to mitigate chemical network defects of fused silica with life enhancement of He-Ne laser device, International Journal of Optics and Technology,113 (2019) 289-302.

Communicated to journal

1. Enni Krishna, D Sam Dayala Dev, and Manas Das, A novel plasma processing technique for uniform nanopolishing of freeform hemispherical shell. Journal of Materials Processing Tech (Under review).
2. Enni Krishna, D Sam Dayala Dev, Sreelakshmi K, and Manas Das **Material removal rate comparative study for medium pressure plasma processing of fused silica. Journal of Plasma Science and Plasma Chemistry (communicated).**

Book chapter

1. Enni Krishna, D Sam Dayala Dev, Manas Das, "Induction of Conditioning gas and its Optimization in Non-Conventional Plasma Machining Process of Fused Silica", Advances in Mechanical Engineering, Lecture Notes in Mechanical Engineering, Springer Nature Singapore Pte Ltd., 2020, pp. 549-559, DOI: 10.1007/978-981-15-0124-1_50.

Conference proceedings

1. Enni Krishna, D Sam Dayala Dev, and Manas Das, Induction of conditioning and its optimization in non-conventional plasma machining process of fused silica, International Conference on Recent Innovations and Developments in Mechanical Engineering (IC-RIDME 2018), National Institute of Technology Meghalaya, Shillong, Meghalaya, November 8-10, 2018 (Paper ID 349). **(Received best paper award)**
2. Enni Krishna, D Sam Dayala Dev and Manas Das, Simulation for uniform plasma processing of hemispherical shell, 2nd International Conference on Computational Methods in Manufacturing, ICCMM 2019, Indian Institute of Technology Guwahati, March 8-9, 2019 (Paper ID 71).
3. Enni Krishna, Sreelakshmy K, D Sam Dayala Dev and Manas Das, Material Removal Rate comparative study for medium pressure plasma processing of fused silica, COPEN 11-2019, IIT Indore (Paper id 008). **(Received best paper award).**